Universidade do Minho
Escola de Engenharia
Instituto de Investigação em Biomateriais,
Biodegradáveis e Biomiméticos

João Pedro Fernandes Ribeiro

Bioisnpired organic-inorganic nanocomposite scaffolds for bone tissue engineering

julho de 2021

Bioisnpired organic-inorganic nanocomposite scaffolds for bone tissue engineering

João Pedro Fernandes Ribeiro

UMinho | 2021

Universidade do Minho
Escola de Engenharia
Instituto de Investigação em Biomateriais,
Biodegradáveis e Biomiméticos

João Pedro Fernandes Ribeiro

Bioinspired organic-inorganic nanocomposite scaffolds for bone tissue engineering

Dissertação de Mestrado

Ciclo de Estudos Integrados Conducentes ao Grau de Mestre em Engenharia Biomédica

Ramo Biomateriais, Reabilitação e Biomecânica

Trabalho efetuado sob a orientação de

Professora Doutora Maria Manuela Estima Gomes

e a co-orientação de

Doutor Manuel Gómez-Florit

julho de 2021

Agradecimentos

A concretização desta dissertação contou com grandes e importantes contributos, de forma direta ou indireta, de várias pessoas e entidades às quais gostaria de expressar o meu agradecimento.

Em primeiro lugar, gostaria de agradecer ao Professor Rui Reis pela oportunidade e privilégio de desenvolver a minha dissertação de mestrado no Instituto de Investigação em Biomateriais, Biodegradáveis e Biomiméticos (I3BS), na Universidade do Minho.

Agradeço à minha orientadora, Professora Manuela Gomes, pela oportunidade de integrar a sua equipa de investigação e desenvolver esta tese sob a sua orientação. Agradeço profundamente, pela confiança que depositou em mim e pelo apoio e disponibilidade demonstrados, que foram cruciais na realização desta tese.

Ao meu co-orientador, Manuel Gómez-Florit, um agradecimento especial por me ter acolhido como seu orientando depois de fase menos positiva. Agradeço profundamente toda a ajuda, paciência, partilha de ideias, e todo apoio e conhecimentos transmitidos. Não poderia estar mais grato por ter um investigador como o Manu a acompanhar toda esta aventura e a comprovar a velha máxima de que Deus escreve direito por linhas tortas.

Uma palavra de agradecimento também para o Rui Domingues por um lado, juntamente com o Manu, ter ajudado a dar a volta a uma situação periclitante e difícil e, por outro lado, ter sempre disponibilidade para o superconcorrido confocal.

Um agradecimento ao projeto InjecTE que providenciou o financiamento para a elaboração desta tese.

A todos os colegas de laboratório com quem tive a oportunidade de trabalhar e partilhar conhecimentos e vivências. Um especial agradecimento à Mahwish por ter aceitado despender o seu tempo para me ajudar em diversas situações que me permitiram terminar este projeto com sucesso. Obrigado pelas boas ideias, pelas palavras de conforto em todos os momentos e pelos infinitos after-hours que pedimos. Um especial obrigado também para a Sofia e a Sara Vieira, por todas as conversas e sinceramente por serem as pessoas que são e por apoiarem sempre e darem sempre força para continuar em frente.

Agradeço também ao staff i3Bs, particularmente à Elsa Ribeiro e Belinha pela aquisição das imagens de SEM e por todas as conversas fantásticas e momentos bem passados.

À fantástica Library Crew e a todos que por ela já passaram, já foram muitos. Obrigada por me alegrarem até mesmo naqueles dias em que nada corria bem. Obrigada a todos por serem quem são e por ter tido a sorte de vos conhecer. Em especial uma palavra para a Filipa, Megui, Inês, Ana Olival (o cabeção), Leonor, Didi e também para o Rafa e Rodrigo por todos os momentos vividos naqueles curtos metros quadrados em área, mas muito mais que isso em amizade. Levo-vos a todos para a vida e nunca me esquecerei dos melhores momentos vividos convosco. Um obrigado também a nova geração da Library Crew, à Rosa, Margarida, Ida e Mário, que a vida vos permita continuar a serem felizes e vos trago muito sucesso e saúde. Obrigado, também à Catarina Vale pelos desabafos e conversas científicas, mas sobretudo non-sense sobre qualquer coisa que viesse à baila.

Aos meus amigos de universidade, obrigado por todos os momentos vividos nesta inesquecível aventura que é a universidade. Muito obrigado aos broquitos de biomédica por todos os momentos proporcionados, todos os cabeções, noitadas, idas às termas e ao rio, enfim, obrigado por tudo. Aos meus amigos de sempre, Freitas, Moisés, Mário, Tiago, Tropa, Rui e respetivas namoradas, obrigado por todo o apoio, carinho e compreensão e por continuarem a compartilhar, todos os momentos desta vida comigo. Os que já foram vividos foram sem dúvida inesquecíveis.

À minha Mãe, aos meus padrinhos e aos meus primos um especialíssimo obrigado por terem aguentado e terem tido paciência para os momentos menos bons deste percurso, mas também por me terem proporcionado momentos bastantes felizes. À Mariana e à mãe por serem as pessoas incríveis que são, que apesar de a vida ter pregados inúmeras e difíceis rasteiras, nunca deixaram se estar presentes e por me terem sempre apoiado e dado carinho. Muito obrigado. É com nostalgia que me despeço desta longa aventura que foi a vida académica e com a certeza que tudo o que foi vivido e aprendido durante esta viagem foi fundamental para o meu crescimento pessoal e profissional.

“A vida é curta demais para se acordar com arrependimentos. Ama as pessoas que te tratam bem. Esquece aquelas que não. A vida coloca cada um no seu lugar. Tudo vai e vem por uma razão. Se tens uma segunda oportunidade, agarra-a. Ninguém disse que a vida seria fácil. Só prometeu que iria valer a pena. Vive, deixa viver e sê feliz !” António Feio

DECLARAÇÃO DE INTEGRIDADE

Declaro ter atuado com integridade na elaboração do presente trabalho académico e confirmo que não recorri à prática de plágio nem a qualquer forma de utilização indevida ou falsificação de informações ou resultados em nenhuma das etapas conducente à sua elaboração.
Mais declaro que conheço e que respeitei o Código de Conduta Ética da Universidade do Minho.

STATEMENT OF INTEGRITY

I hereby declare having conducted this academic work with integrity. I confirm that I have not used plagiarism or any form of undue use of information or falsification of results along the process leading to its elaboration.
I further declare that I have fully acknowledged the Code of Ethical Conduct of the University of Minho.

Resumo

O tecido ósseo é um compósito orgânico-inorgânico, cuja matriz extracelular (ECM) é fortemente mineralizada à nanoescala, que constitui o esqueleto do corpo e é crucial para a locomoção. É principalmente composto por cristais de apatite embutidos dentro e entre as fibras de colágeno e proteínas não colágenas (NCPs), que se acredita que desempenham um papel ativo no processo de biomineralização em nanoescala. Diversas estratégias de engenharia de tecidos foram propostas combinando biomateriais inorgânicos e / ou orgânicos, células progenitoras e estímulos bioquímicos. Apesar dos elevados níveis de sucesso destas, não existem estratégias que reproduzam totalmente e com sucesso a verdadeira complexidade do tecido ósseo e do microambiente de biomineralização à nanoescala. Neste trabalho propomos uma estratégia biomimética na qual um criogel bioativo baseado em lisado de plaquetas (PL) reticulado através de nanocristais de celulose funcionalizados com grupos aldeído (a-CNCs) incorpora CNCs mineralizados (m-CNCs) podria replicar o processo e o microambiente da biomineralização à nanoescala, e promover a diferenciação osteogénica de células progenitoras/estaminais. Além disso, pretendemos mimetizar o papel das proteínas nativas não colágenas (NCPs) na regulação da deposição de apatite intra- e extrafibrilar no colágenio com a incorporação dos CNCs mineralizados. Os criogéis desenvolvidos aumentaram a proliferação de células estaminais, a atividade metabólica e a atividade da fosfatase alcalina, bem como regularam positivamente a expressão de marcadores relacionados com osso, sem suplementação osteogénica, demonstrando as suas propriedades osteoindutivas. Em suma, os criógeis mineralizados à nanoescala propostos constituem um biomaterial alternativo com um grande nível de biomimética que podem ser aplicados em amplas abordagens regenerativas ósseas.

Palavras-Chave: Biomineralização à nanoescala, proteínas não colágenas, criógeis, nanocristais de celulose, hidroxiapatite, lisado de plaquetas

Abstract

Bone tissue is an organic-inorganic composite, showing an extracellular matrix (ECM) that is heavily mineralized on the nanoscale, that constitutes the body skeleton and is crucial for locomotion. It is mostly composed of apatite crystals embedded within and between the collagen fibers and non-collagenous proteins (NCPs), which are thought to play an active role on the nanoscale biomineralization process. Several tissue engineering and regenerative medicine (TERM) strategies have been proposed combining inorganic and/or organic biomaterials, progenitor cells, and biochemical stimuli. Despite the increased levels of success towards bone regeneration, there are no strategies that fully and successfully replicate the true complexity of bone tissue and the nanoscale biomineralization microenvironment. Herein, we propose a biomimetic strategy where a bioactive cryogel scaffold based on platelet lysate (PL) crosslinked through aldehyde-functionalized cellulose nanocrystals (a-CNCs) incorporates mineralized CNCs (m-CNCs) in order to replicate the nanoscale biomineralization process and microenvironment and promote the osteogenic differentiation of progenitor/stem cells. Moreover, we intended to mimic the native non-collagenous proteins (NCPs) role on regulating the deposition of both intra- and extrafibrillar apatite in collagen with the m-CNCs. The developed cryogels enhanced stem cell proliferation, metabolic activity, and alkaline phosphatase activity as well as up-regulated the expression of bon-related markers, without osteogenic supplementation, demonstrating their osteoinductive properties. Ultimately, the proposed nanoscale mineralized cryogel scaffolds provide an alternative with a great level of biomimicry that may be applied in broad bone regenerative approaches.

Keywords: Nanoscale biomineralization, non-collagenous proteins, cryogels, cellulose nanocrystals, hydroxyapatite, platelet lysate

Table of contents

List of abbreviations

#

%	Percentage
3D	Three Dimensional
α-MEM	Alpha Minimum Essential Medium
β-TCP	Beta-Tricalcium Phosphate
Ø	Diameter
λ	wavelength
ε	Tensile Strain
σ	Tensile Stress
°	Degree
°C	Degree Celsius
µm	micrometres
µL	microlitres
µS	micro-Siemens

A

A	Cross-sectional area
A/A	Antibiotic/Antimycotic
aCNCs	Aldehyde modified CNCs
ACP	Amorphous Calcium Phosphates
ALP	Alkaline Phosphatase
ASCs	Adipose derived Stem Cells
ATP	Adenosine Triphosphate
ATR	Attenuated Total Reflectance
Au	Gold
A-High	Amorphous-High
A-Low	Amorphous-Low

B

BBM	Bovine derived Bone Matrix
BCP	Biphasic Calcium Phosphate
BMPs	Bone Morphogenic Proteins
BMSCs	Bone marrow derived Stem Cells
BSA	Bovine Serum Albumin
BSP	Bone Sialoprotein

C

Ca	Calcium
CAD	Computer Aided Design
CD31	Cluster of Differentiation 31
cDNA	Complementary DNA
CGCG	Central Giant Cell Granuloma
C-High	Crystalline-High
CHSJ	Centro Hospitalar São João
CHT	Chitosan
Cl^-	Chloride ion
C-Low	Crystalline-Low
cm	Centimetres
cm^3	Cubic centimetres
CNCs	Cellulose Nanocrystals
CO_2	Carbon Dioxide
CO_3^{2-}	Carbonate ion
COL1A1	Alpha-1 type I Collagen
CPC	Calcium Phosphate Cement
Ct	Computed Tomography

D

Da	Dalton
DAPI	4,6-diamidino-2-phenyindole dilactate
DGP	Dentin Glycoprotein
DI Water	Deionized water
DKK-1	Dickkopf-related Protein
DMEM	Dulbecco´s Modified Medium
DMP-1	Dentin Matrix Protein-1
DNA	Deoxyribonucleic Acid
DPCs	Dental Pulp Cells
DPP	Dentin Phosphoprotein
DPSCs	Dental Pulp Stem Cells
DSP	Dentin Sialoprotein
DSPP	Dentin Sialophosphoprotein

E

E	Young´s Modulus
ECGF	Epithelial Cell Growth Factor
ECM	Extracellular Matrix
EDS	Energy Dispersive X-ray Spectroscopy
EGF	Epidermal Growth Factor
ESCs	Embryonic Stem Cells

F

F	Forward Primer
F^-	Fluor ion
FBS	Fetal Bovine Serum
FDA	US Food and Drug Administration
FGF	Fibroblast Growth Factor
FTIR	Fourier Transform Infrared Spectroscopy

G

g	Grams
GAGs	Glycosaminoglycans
GAPDH	Glyceraldehyde-3-phospahte dehydrogenase
GBR	Guided Bone Regeneration
GFs	Growth Factors
Gla-proteins	Matrix Gamma-Carboxy Glutamic Acid-containing Proteins
GO	Graphene Oxide
GPa	Giga Pascal
GTR	Guided Tissue Regeneration

H

h	Hour
HA	Hyaluronic Acid
Hap	Hydroxyapatite
hASCs	Human Adipose derived Stem Cells
HCl	Hydrochloric Acid
hDPCs	Human Dental Pulp Cells
H&E	Hematoxylin and Eosin
HGF	Hepatocyte Growth Factor
HPO_4^{2-}	Hydrogen phosphate ion
HR-SEM	High-Resolution SEM
HUVECs	Human Umbilical Vein Endothelial Cells

I

ICC	Immunocytochemistry
IGF	Insulin-like Growth Factor
IHC	Immunohistochemistry
iPSCs	Induced Pluripotent Stem Cells
IR	Infrared
IRE	Reflection Element

K

k^+	Potassium ion
kDa	Kilodalton
kV	Kilovolts

L

L	Litres

M

M	Molar
m	Metres
MCC	Microcrystalline Cellulose
m-CNCs	Mineralized CNCs
MEPE	Matrix Extracellular Phosphoglycoprotein
Mg^{2+}	Magnesium ion
min	minutes
mL	millilitres
mm	millimetres
mM	milimolar
MoS_2	Molybdenum Sulfate
MSCs	Mesenchymal Stem Cells
MWCO	Molecular Weight Cut-off
MW	Molecular Weight
MΩ	Megaohm

N

N	Newtons
N_2	Nitrogen
Na^+	Sodium ion
NaCl	Sodium Chloride
$NaIO_4$	Sodium Periodate
NaOH	Sodium Hydroxyde
NBM	Natural Bone Mineral
NCPs	Non-collagenous Proteins
nm	nanometres

O

OC	Osteocalcin
OM	Osteogenic Medium
ONN	Osteonectin
OPG	Osteoprotegerin
OPN	Osteopontin
OSX	Osterix

P

P	Phosphate
Pa	Pascal
PBS	Phosphate-Buffered Saline
PC	Platelet Concentrates
PCL	Polycaprolactone
PCR	Polymerase Chain Reaction
Pd	Palladium
PDGF	Platelet-derived Growth Factor
PDL	Periodontal Ligament
PDLCs	Peridontal Ligament Cells
PDPCs	Periosteal derived Stem Cells

PECAM-1	Platelet Endothelial Cell Adhesion Molecule
PGA	Poly(glycolic acid)
PGs	Proteoglycans
PI	Propidium Iodide
PL	Platelet Lysate
PLA	Poly(lactic acid)
PLGA	Poly(glycolide-co-lactide) acid
pnP	p-nitrophenol
pnPP	p-nitrophenyl Phosphate
PRHds	Platelet-rich Hemoderivatives
PRP	Platelet-rich Plasma
PS	Polystyrene
Pt	Platinum
PTTM	Porous Tantalum Trabecular Metal

R

R	Reverse Primer
RANKL	Activator of NF-kβ Ligand
RCS	Root Canal System
RNA	Ribonucleic Acid
rpm	Revolutions per minute
RRA	Recurrence Rate Average
RT	Room Temperature
RT-PCR	Reverse Transcriptase PCR
RUNX2	Runt-related Transcription Factor 2

S

s	seconds
SBF	Simulated Body Fluid
SEM	Scanning Electron Microscopy
Si^{4+}	Silicon ion
SiO_4^{4-}	Silicate ion
SMNs	Skeletal Maxillofacial Neoplasms
SO_3^-	Sulphur trioxide ion
Sr^{2+}	Strontium ion
s-SBF	simplified-SBF

T

TCP	Tricalcium Phosphate
TE	Tissue Engineering
TERM	Tissue Engineering and Regenerative Medicine
TGA	Thermogravimetric Analysis
TGF-β	Transforming Growth Gactor Beta
Ti	Titanium
TRITC	Tetramethylrhodamine B Isothiocyanate

U

UK	United Kingdom
US/USA	United States of America

V

VEGF	Vascular Endothelial Growth Factor
v/v	Volume concentration (volume per volume)

W

Wf	Final Weight
WHO	World Health Organization
Wi	Initial Weight
wt	Weight
w/v	Mass concentration (weight per volume)

X

Xg	Relative Centrifugal Force
XRD	X-ray Diffraction

Z

Zn^{2+}	Zinc ion

List of Figures

Chapter I. Introduction

Chapter II. Materials and Methods

Chapter III. Bioinspired organic-inorganic nanocomposite scaffolds for bone tissue engineering

Chapter III. Supporting Information

List of Tables

Chapter I. Introduction

Chapter II. Materials and Methods

List of Equations

Chapter II. Materials and Methods

Chapter III. Bioinspired organic-inorganic nanocomposite scaffolds for bone tissue engineering

Chapter I.

General Introduction

This chapter is based on the following publication:

J. P. Ribeiro, E. A. Astudillo-Ortiz, P. S. Babo, and M. E. Gomes, "Tissue engineering strategies for the treatment of skeletal maxillofacial defects resulting from neoplasms resections," in *Biomaterials for 3D Tumor Modeling*, Elsevier, 2020, pp. 697–730.

Chapter I. General Introduction

1.1. Tooth morphology and function

Teeth and tissues around them play key roles in everyday functions as mastication, phonation, speech, aesthetics, and even facial expressions [1]. Untreated oral diseases can profoundly impact people's quality of life by inflicting pain and discomfort, restricting normal day-life activities [2]. In advanced states, oral diseases, such as deep caries or periodontal diseases, can compromise tooth vitality or destroy the tooth structure and supporting tissues leading to extreme pain, bleeding, ulcerations, abscesses, and, ultimately, tooth loss [2]–[4]. Poor oral health can also limit food choices and diminish chewing efficiency, which leads to nutritional imbalances such as weight loss or obesity in elderly adults [2], [5]–[8]. Oral diseases have been also associated with systemic co-morbidities, such as increased risk of cardiovascular diseases, respiratory infections, adverse pregnancy outcomes, septicaemia, rheumatoid arthritis, cognitive impairments, diabetes, and cancer [2], [9]–[11]. Moreover, the aesthetical consequences of oral diseases have a strong social burden: detract physical appearance, affect individuals' speech, lower self-esteem, inhibit intimacy, and harm mental health [2], [12], [13]. Therefore, good oral health is crucial for general health and quality of life.

The tooth is a complex biologic composite organ composed of mineralized and non-mineralized tissues that are connected to the surrounding periodontal tissues (figure I.1) [14]–[16]. Enamel, dentin, cementum, and alveolar bone constitute the mineralized tissues whereas dental pulp, gingiva, and periodontal ligament are the major non-mineralized tissues [14]–[16]. Structurally, a tooth consists of a crown covered by enamel and a root covered by bone-like cementum [17]. It contains also the dental pulp, a soft connective tissue, continuous with the periodontal ligament via the apical foramen, which contains vessels and sensory nerves that support dentin [17]. The pulp cavity is surrounded by dentine and expands at the coronal end into a pulp chamber and narrows apically into the root canal system (RCS) [17].

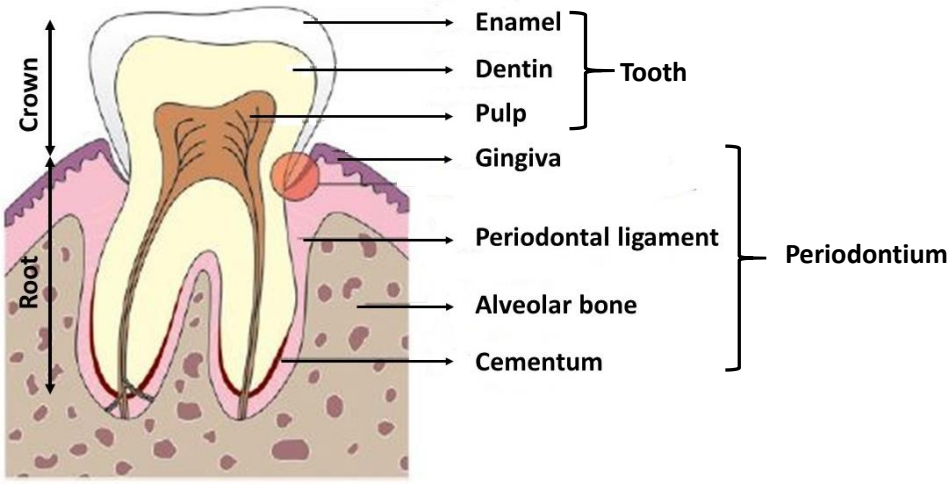

Figure I.1: Schematic representation of tooth´s anatomy. Adapted from [16].

1.2. Periodontium

The periodontal tissues (or periodontium) are defined as the tissues that surround the teeth [18]. It is a complex structure designed to anchor the tooth to the maxillary or mandibular bone, while providing a biological seal between the tooth and the oral epithelium, capable of withstanding the forces generated by the masticatory process and acting as a protective barrier against foreign invaders, as microorganisms [18], [19].

Periodontium is composed of four main components, namely the gingiva and periodontal ligament (PDL), as soft tissues, and the cementum and alveolar bone, as hard tissues [14], [18], [20], as depicted in figure I.1. In a healthy situation, gingiva covers the alveolar bone and tooth root to the cementoenamel junction, providing the aforementioned defensive barrier [20]. The PDL is a soft, dense, fibrous connective tissue (mostly composed of collagen type I), which attaches teeth to the alveolar bone through the PDL or Sharpey´s fibers, and absorbs and dissipates loads applied to the teeth during function [18], [21]. Cementum is a thin avascular bone-like tissue that covers the surface of tooth roots [18], [21]. Besides providing the attachment of the tooth to the alveolar bone by insertion of PDL fibers, it also prevents root resorption during remodelling of the periodontium [18], [21]. Alveolar bone holds the tooth in place and is constantly remodelling in response to the functional demand placed on it [18], [21].

1.2.1. Alveolar Bone

Bone tissue is a mineralized viscoelastic connective tissue which makes up the body skeleton and exerts crucial functions for it, such as providing (1) shape and support to the body; (2) attachment for tendons and muscles, which are essential for locomotion; (3) protection for the vital organs and other tissues; (4) storage for minerals and also blood cells [16]. Alveolar bone is a specialized part of the mandibular and maxillary bones that forms and supports the sockets (alveoli) of the teeth [16], [21], [22]. Although fundamentally comparable to other bone tissues in the body, alveolar bone is distinctive because it is subjected to a continual and very rapid remodelling associated with tooth eruption and movement, subsequently, with the functional demands of mastication, and it is lost in the absence of a tooth [21], [22].

Anatomically, alveolar bone consists of outer cortical plates (buccal, lingual, and palatal) of compact bone, a central spongiosa, and bone lining the alveolus [16], [21]–[23]. The cortical plate and bone lining the alveolus meet at the alveolar crest. The bone lining the socket is specifically referred to as bundle bone because it provides attachment for the PDL fiber bundles [16], [21]–[23]. Moreover, the cortical plates consist of surface layers (lamellae) of fine-fibered bone supported by Haversian systems, and are generally thinner in the maxilla and thickest on the buccal aspect of mandibular premolars and molars [16], [21]–[23]. The trabecular (or spongy) bone, which fills the central part of the alveolar process also consists of bone disposed in lamellae, with the typical Haversian systems present in the larger trabeculae [16], [21]–[23]. In addition, the intertrabecular spaces are usually filled with yellow marrow, rich in adipocytes and pluripotent mesenchymal cells, although sometimes there can also be some red or hematopoietic marrow [16], [21]–[23]. Trabecular bone is absent in the region of the anterior teeth; therefore, the cortical plate and alveolar bone are fused together [16], [21]–[23].

Alveolar bone is a composite material that consists of 65% inorganic material, 25% organic matter (2-5% cells), and 10% water [23], [24]. Regarding the inorganic material, it is composed of plate-shaped crystalline hydroxyapatite (HAp) and some other minor elements, including phosphates, carbonates, and sulphates, that can be found within the interfibrillar space of the collagen fibers [16], [22]. The organic matrix, also known as osteoid, consists of collagen and non-collagenous proteins (NCPs). Collagen (mainly type I) is the major organic component in alveolar bone (80-90%), acting as

scaffold where Hap can be deposited that provides the basic structural integrity for connective tissues and a stable connection with the tooth [16], [22]. In addition, the elasticity of collagen imparts resiliency to the tissue and helps to resist fractures [16]. The remaining organic content (10%) is characterized by the presence of NCPs, including proteoglycans (PGs), glycoproteins, phospholipids, and numerous growth factors (GFs). They are critical participants in bone formation, homeostasis, and remodelling due to their ability to regulate extracellular matrix (ECM) organization, namely collagen fibrillogenesis and degradation, ECM signalling and interactions with cells, mineral and GFs, cellular function and motility, and the mineralization process.

NCPs, including glycosaminoglycans (GAGs) and proteoglycans, possess main roles in the mineralization front. The more characteristic NCPs found in the alveolar bone are alkaline phosphatase (ALP), osteonectin (ONN), osteopontin (OPN), bone sialoprotein (BSP), matrix extracellular phosphoglycoprotein (MEPE), osteocalcin (OC), matrix gamma-carboxyglutamate-containing proteins (Gla proteins), fibronectin, and vitronectin, among others [16], [22], [25]. Dentin matrix protein-1 (DMP-1) and dentin sialophosphoprotein (DSPP), precursors of dentin sialoprotein (DSP), dentin phosphoprotein (DPP) and dentin glycoprotein (DGP), which were thought to be exclusively found in dentin, are also present in bone [25].

Moreover, a cocktail of GFs is also present in alveolar bone ECM, including the transforming growth factors beta (TGF-β), fibroblast growth factor (FGF), insulin-like growth factor I and II (IGF-I and IGF-II), bone morphogenic proteins (BMPs), and platelet-derived growth factor (PDGF) [16], [23]. They are important for the formation, homeostasis, maintenance, and repair of the alveolar bone [16], [23].

Different cells are responsible for the formation, resorption, and maintenance of osteoarchitecture of alveolar bone. Two cell lineages are present in bone, each with specific functions: (1) osteogenic cells (osteoblasts, osteocytes, and bone-lining cells), which form and maintain bone, and (2) osteoclasts, which resorb bone [16], [22], [23]. Osteoblasts are mononucleated cells responsible for the synthesis and secretion of the organic matrix of bone [16], [22], [23]. These cells are derived from osteoprogenitor cells of mesenchymal origin, which are present in the bone marrow and other connective tissues [16], [22], [23]. As the osteoblasts form the bone matrix, they either get entrapped within the matrix they secrete, whether mineralized or unmineralized, and become

osteocytes or remain on the surface as bone-lining cells, having important roles on the homeostasis and remodelling of bone [16], [22], [23]. Osteoclasts are multinucleated giant cells derived from hemopoietic cells of monocyte macrophage lineage that resorb bone tissue by removing the mineralized matrix of bone [16], [22], [23]. Indeed, the coupling between bone formation and resorption processes constitutes one of the fundamental principles for bone remodelled throughout life [16], [22], [23].

1.3. Diseases of periodontium

Oral diseases are a major global public health and socioeconomic burden, having both high prevalence and major negative impacts on individuals, communities, and society, reducing the quality of life for those affected [27]. According to the World Health Organization, chronic and progressive oral diseases affect over 3.5 billion people worldwide, starting in early childhood and progressing throughout individuals´ lifetime [27].

Periodontal diseases, along with dental caries, are the main diseases that affect the dental tissues. They are a group of chronic inflammatory conditions that affect the periodontal tissues as a result of the inflammatory response to accumulation of the dental plaque biofilm at the gingival margin of the teeth [18], [28]. The conditions range from gingivitis, a mild-inflammatory response that is confined to the superficial gingival tissues, to periodontitis, an immune-inflammatory response characterized by a progressive destruction of the supporting tissues of teeth, including alveolar bone [18], [28]. Gingivitis may persist for many years and with good oral hygiene is completely reversible. If untreated, it may lead to periodontitis, the non-reversible destructive stage that affects the supporting tissues, resulting in attachment loss, bone resorption, poor aesthetics, oral discomfort and loss of function, halitosis, and ultimately tooth loss [18], [28]. Furthermore, periodontal diseases can have multifactorial etiology involving microbial, lifestyle-related (inadequate oral hygiene, smoking, and alcohol), systemic (immune or metabolic diseases), and genetic factors [28], [29]. The periodontal diseases are highly prevalent worldwide, affecting up to 90% of the population [29], being the prevalence among adults 50-90% for gingivitis and 5-20% for severe forms of periodontitis [30]. In US periodontitis is considered a public health concern, affecting 46% of US adults representing 64.7 million people, with 8.9% suffering from severe forms of the disease [31].

Another type of periodontium disease or severe outcome of periodontal diseases is the development of oral and maxillofacial neoplasms. In the next sections, these types of neoplasm will be presented as well as the different tissue engineering (TE) strategies to overcome them.

1.3.1. Oral and Maxillofacial Neoplasms

Oral and maxillofacial neoplasms are malignancies affecting the oral mucosa or underlying structures in the area between the vermillion border of the lip and the faucial pillars superolaterally, and the base of the tongue inferiorly. Other structures typically involved include the maxilla, mandible, other facial skeleton and skin, and salivary glands. The World Health Organization (WHO) estimates that annually occur about 657,000 new cases of cancers of the oral cavity and pharynx worldwide (Figure I.2), causing more than 330,000 deaths.

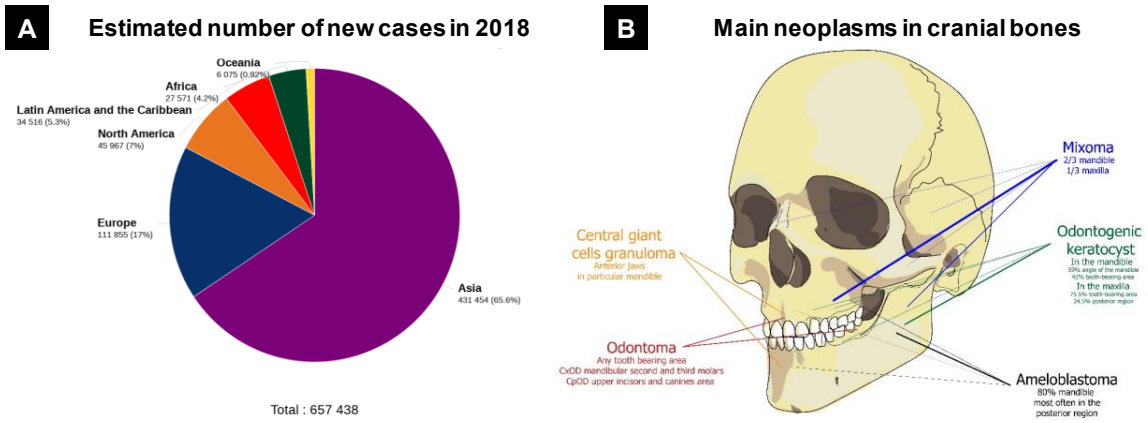

Figure I.2: Oral and maxillofacial cancer prevalence. A) Estimated number of new cases of new oral cavity and pharynx cancer per continent in 2018, for both sexes and all ages (source: Globocan2018; Graph production: Global Cancer Observatory (http://gco.iarc.fr) IARC). B) Distribution of the main neoplasms affecting cranial bones. The thickness of the lines indicates its greater or lesser prevalence according to the literature.

Skeletal maxillofacial neoplasms (SMNs) are particularly pernicious as both their presence and treatment present significant cosmetic and functional limitations, reducing patients quality of life [32]. These are often asymptomatic for long time, and very rarely cause pain, being difficult to detect in early stages even using radiologic tools [33]. The WHO, in their last classification of Head and Neck Tumors in 2017 [34], considered thirteen groups of odontogenic and maxillofacial bone tumors involving around sixty-two diseases. Most of them are considered rare, sporadic, unknown, or only a few cases have been reported worldwide. The most prevalent SMNs, summarized in Table I.1, include myxoma, ameloblastoma, odontoma, odontogenic keratocyst and central giant cells glioblastoma, and can be of

dental origin (odontogenic) or arise from bony tissues. The benign or malignant character of bone maxillofacial neoplasms is based on specific histological criteria, including the presence or absence of necrosis, mitotic figures as well as basic understanding of the entity [35].

Table I.1: Summary of the most prevalent maxillary neoplasms.

Name	Definition	Epidemiology	Localization	Treatment	Prognosis
Myxoma	Spindle-shaped cells dispersed in abundant myxoid ECM	2-5% of all the tumors	2/3 mandible 1/3 maxilla	Curettage/complete excision with free margins	RRA 25%
Ameloblastoma	Benign intraosseous progressively growing epithelial odontogenic neoplasm	1% of all the tumors	80% mandible, most often in the posterior region	Wide surgical excision	RRA 60-80% 50% within 5 years
Odontoma	Tumor-like malformation (hamartoma) composed of dental hard and soft tissues	Most common odontogenic tumors	Any tooth-bearing area	Conservative surgery	Unusual recurrence
Odontogenic keratocyst	Odontogenic cyst with a regular lining of parakeratinized stratified squamous epithelium with palisading hyperchromatic basal cells.	10-20% of the odontogenic cysts. The third most common cyst of the jaws	80% mandible	Enucleation or surgical resection for large lesions	RRA 25%
Central giant cells granuloma	Osteolytic lesion of the jaws characterized by osteoclast-type giant cells in a vascular stroma	10% of benign gnathic tumors	More frequent in the anterior jaws, in particular, the mandible.	Local curettage	Higher recurrence rate

Abbreviations: ECM, extracellular matrix; RRA, Recurrence rate average

1.3.1.1. Myxoma

Myxoma are a group of rare benign tumors of connective-tissue origin that occur in both hard (central) and soft tissues of the body (Figure I.3) [36], [37]. The treatment to myxomas consists in wide surgical excision with a 2.0 cm margin of bone, resulting in most of the excisions of mandibular myxomas in segmental mandibular resection (76.3%) or hemi-mandibulectomy (10.5%) [38].

1.3.1.2. Ameloblastoma

Ameloblastoma is a benign intraosseous progressively growing epithelial odontogenic neoplasm characterized by expansion and tendency or local recurrence if not adequately removed [34]. Ameloblastoma can be associated with un-erupted third molar teeth (Figure I.3) [39]. Treatment can

be conservative or radical. Enucleation, curettage, and surgical excision are considered as part of the conventional treatment. Radical treatment consists of bone resection [40].

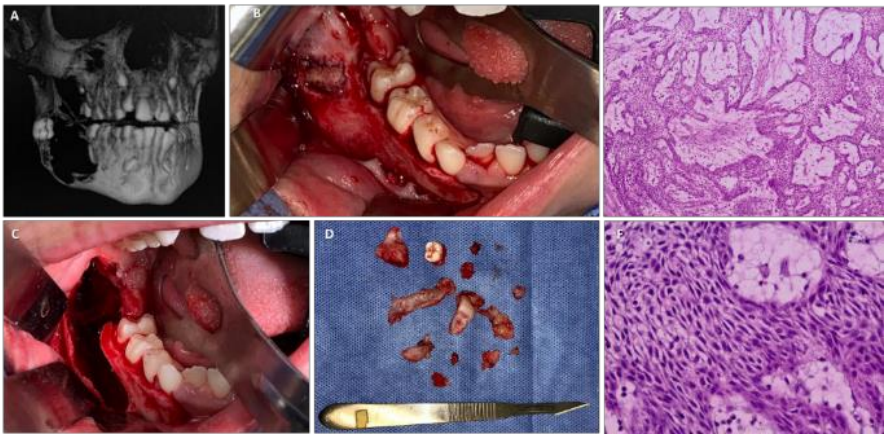

Figure I.3: Example of a type of skeletal maxillofacial neoplasm with significant bone loss. Unicystic ameloblastoma. A. 3D tomography. B. Open flap before osteotomy. C. Conservative surgery. 5-fluorouracil was used topically to avoid recidivism. D. Ameloblastoma and third molar fragments (Courtesy of Dr. Juan Benenaula Bojorque). E and F. Histopathological analysis at 100x and 400x respectively shows epithelial invasion in the ameloblastoma capsule in a plexiform disposition; the peripheral cells are less pronounced than in the follicular type; the connective tissue is loose and often undergoing cystic changes (Courtesy Dr. Fernanda Torres Calle).

1.3.1.3. Odontoma

Odontoma are calcifying benign tumors of odontogenic origin characterized by their slow growth [41], [42]. They consist of enamel, dentine, cementum, and pulpal tissue [34], [41]. Odontoma are frequently associated with an un-erupted teeth and are usually detected on routine radiographs [34]. The traditional treatment consists of surgical elimination, and there is a small likelihood of recurrence [42].

1.3.1.4. Odontogenic keratocyst

The odontogenic keratocyst is a locally aggressive, cystic jaw lesion with a putatively high growth potential and a propensity for recurrence [43]. Treatment is usually the enucleation, or surgical resection of large lesions [34], [44].

1.3.1.5. Central giant cells granuloma

Central giant cell granuloma (CGCG) is a benign but sometimes aggressive lesion of the maxillofacial area, characterized by osteoclast-type giant cells in a vascular stroma [34], [45]. The treatment of this lesion depends on the severity of the lesion. Usually is recommended the surgical enucleation with curettage or resection [46]. Conservative therapies can also be used in combination

with the surgical treatment, or as alternative and include the administration of as corticosteroids, calcitonin, interferon, or bisphosphonates [46].

1.4. Currently used therapies

The traditional clinical options to treat these tumors can be more or less conservative, depending on size, location, and malignancy [47]. Considering Hupp [47], the three primary modalities of surgical excision of maxillary tumors are enucleation, segmental or partial resection, and compound resection. Smaller bony defects (<4 to 6 cm) are commonly treated with enucleation followed by filling of the defect with non-vascularized cortico-cancellous grafts harvested from the anterior or posterior iliac crest [48]. On the other hand, when it has been determined that the lesion is aggressive by histopathological examination, excision can be accompanied by resection of the lesion and adjacent bone margins [47]. Finally, when the malignancy or the recurrence rate is very high, the treatment includes total resection of the tumor by removing all of the affected bone [47], sometimes accompanied with an adjuvant chemo or radiotherapy treatment [34]. The loss of mandibular bone continuity due to neoplasm resections creates "socially mutilated" patients due to the significant loss of function and aesthetics [49]. Likewise, the loss of a part of the jaw creates a communication between the maxillary sinuses or nasal cavity with the oral cavity, which causes great difficulties in speaking or eating. Therefore, after the tumor's ablation, patients must be submitted to subsequent reconstruction surgeries to rehabilitate the function and the aesthetics of the tissues, or, in most extreme cases, to prepare the tissues to receive the prosthetics implants. The "gold standard" for the reconstruction of large bone defects is the autologous bone graft. Usually, it requires the collection of a vascularized bone flap from tibia or fibula [50], iliac crest [51], or ribs [52] which is then adapted to the defect and properly fixed to the preserved bone. Further than the patient discomfort, and risk of donor site morbidity, these procedures have limited aesthetic recovery and represent a heavy burden on national healthcare systems worldwide [51]. Moreover, adverse effects of chemo- and radiotherapies can postpone surgical reconstruction procedures due to complications such as thrombocytopenia, which increases a patient's risk for hemorrhaging, and granulocytopenia, which increases the susceptibility for infection [53].

Some alternatives have been used for small bone defects such as guided bone regeneration (GBR). It consists on the use of barrier membranes to protect the blood clot to promote bone first

intentional repair, while preventing infection and soft tissue collapse into the defect, avoiding the colonization of the defect with epithelial cells or fibroblasts [54], [55]. However, oral and maxillofacial surgeons and dentists still face serious difficulties in reconstructing bone maxillofacial defects after tumor resection and in the osteointegration of implantation devices in patients subjected to radiotherapy.

1.5. Tissue engineering for reconstruction of ablated skeletal maxillofacial tissues

The tissue engineering (TE) is a multidisciplinary discipline which, during the last three decades, has explored the principles of biology and engineering to the development of functional substitutes for damaged tissues [56]. The most traditional TE concept consists of three main pillars (figure I.4): cells, scaffolds, and growth factors [57]. Along the years, it has been shown that there are several other complements to these pillars which can enhance the regeneration of the desired tissue. For example, the use of bioreactors to culture TE constructs under specific stimuli has been explored for better mimic the natural physico-chemical environment of native tissue [58].

The oral and maxillofacial regions are quite complex since they consist of several tissues namely, bone, cartilage, and soft tissues, nerves and blood vessels. The restoration of functional and aesthetics demands of the skeletal maxillofacial tissues after oncologic surgery is one of the major challenges for bone TE [59]. In addition to the surgical treatment, the patients may need to be subject to radiotherapy and/or chemotherapy which compromises patient's tissues self-regenerative potential, jeopardizing the success of oral and maxillofacial rehabilitation [60]. Therefore, clinicians have procured inspiration in the most recent advances in bone TE field to find solutions to the surgical rehabilitation of skeletal maxillofacial tissues.

The TE approaches for oral and maxillofacial regeneration besides biocompatible, should be osteoconductive, osteoinductive and osteogenic [61], [62], that is, should (1) act as a provisional template for new bone growth, while (2) stimulate osteoprogenitor cells to develop into pre-osteoblasts or bone-forming cell lineage [61], [63]; (3) but also provide stable anchorage between the living bone and the implant [63]. This has been endured by the right combination of scaffolds, cells, growth factors,

and culturing conditions, and, in the past few years, the exploration of the emergent microfabrication and 3D printing fields (Table I.2).

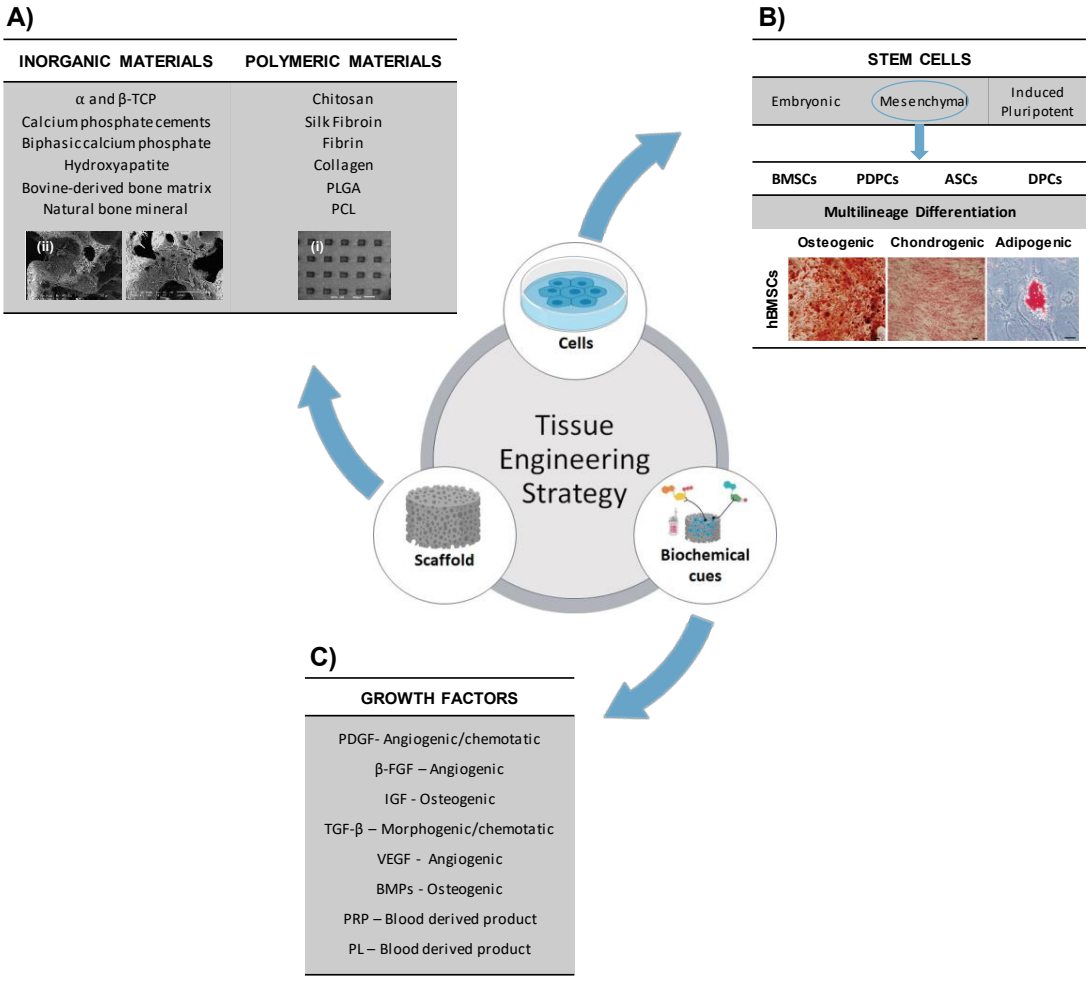

Figure I.4: Schematic of the three pillars for bone tissue engineering. A) Scaffolds from inorganic origin, namely i) ceramic meshes (β-Tricalcium phosphate) [34] or organic origin, such as i) 3D printing polymeric scaffold (polycaprolactone)[48]; B) Stem cells, in particular, multipotent Mesenchymal stem cells isolated from different tissues - bone marrow derived stem cells (BMSCs), periosteal derived progenitor cells (PDPCs), adipose tissue derived stem cells (ASCs) and dental pulp stem cells (DPCs) (tri-lineage differentiation example adapted from [71)]; and C) biochemical cues including growth factors and blood derivatives. Adapted from [79].

Abbreviations: BMP, bone morphogenetic protein; FGF, fibroblast growth factor; IGF, insulin-like growth factor; PDGF, platelet derived growth factor; PL, platelet lysate; PRP, platelet rich plasma; TCP, tri-calcium phosphate; TGF, transforming growth factor; VEGF, vascular endothelial growth factor

Table I.2: Tissue engineering strategies for bone maxillofacial regeneration.

Clinical target	Scaffold	Cell type	Biochemical cues	Type of study	Experimental design	Outcomes	References
Large mandibular defects	β-TCP granules	ASCs	BMP-2	Clinical report	ASCs were combined with β-TCP granules and BMP-2 and cultured in basal medium for 3 weeks. The whole was implanted in a parasymphyseal defect created by ameloblastoma resection.	Bone regeneration 10 months after implantation allowed prosthodontic rehabilitation in the grafted site.	[48]
		BMSCs-hBMP-2	BMP-2	In vitro and in vivo	MSCs were genetically modified with a recombinant human adenovirus type 5 encoding human BMP-2 and later implanted onto ectopic and mandibular defects in (NOD/SCID) mice.	Large mandibular defects.	[64]
	β-TCP granules (Chronos)	ASCs	BMP-2	Clinical report	ASCs were mixed with the BMP-2 laden β-TCP granules and implanted in the rectus abdominis muscle for maturation. Then after 8 months, the microvascular custom-made ectopic bone flap was transplanted to a hemimaxillectomy defect after keratocysts resection.	8 months of after implantation the construct produced a well-ossified and vascularized bone graft ectopically.	[65]
	PCL/ β-TCP (1:1) 3D-printed scaffold	BMSCs		In vivo	BMSCs were seeded into the scaffolds and incubated in a rotational oxygen-permeable bioreactor system for 14 days. Constructs were implanted into mandibular 2 x 2 cm defects in minipigs.	Implanted BMSCs enhanced new bone formation and graft osteointegration 8 weeks after implantation.	[66]

Table I.2: Tissue engineering strategies for bone maxillofacial regeneration. (continued)

Clinical target	Scaffold	Cell type	Biochemical cues	Type of study	Experimental design	Outcomes	References
Maxillofacial bone regeneration	BBM + PRP	ASCs	PRP	In vitro and in vivo	Pre-osteogenic differentiated ASCs carried in BBM mixed with PRP were subcutaneously implanted in subcutaneous model in Balb/c mice.	Increased expression of bone-related genes in a callus-like tissue ectopically, 8 weeks after implantation.	[67]
	3D porous PS scaffolds (Alvetex)	ASCs		In vitro	ACSs spheroids or ASCs seeded PS scaffolds were cultured in OM for 14 days.	Increased osteogenic differentiation, maturation and matrix mineralization by ASCs in PS scaffolds.	[68]
	PLGA/PCL fibrous 3D scaffolds	ASCs	BMP-2	In vitro	Rat ASCs seeded in PLGA/PCL–BMP-2 were cultured in OM over 14 days.	3D scaffold incorporated with BMP-2 significantly increased proliferation and osteogenic differentiation of Rat ASCs.	[69]
	Deciduous red deer antler	Mice-BMSCs	BMP-2 TGF-β	In vitro and in vivo	Mice-BMSCs were seeded in slices of deer antler or OsteoSet and pe-culture in OM or in BMP-2 + TGF-β supplemented OM. Implantation in bone defects surgically induced on the left parietal bone of CD1 mice.	Tissue engineered grafts were proven to be more efficient in bone reconstruction than alloplastic commercial biomaterials (OsteoSet).	[70]
	CPC/CHT	BMSCs		In vitro	BMSCs seeded over CPC/CHT constructs and cultured in OM.	CHT enhanced cell the mechanical properties of CPC, cell adhesion, proliferation and osteogenic differentiation.	[71]

Table I.2: Tissue engineering strategies for bone maxillofacial regeneration. (continued)

Clinical target	Scaffold	Cell type	Biochemical cues	Type of study	Experimental design	Outcomes	References
Maxillofacial bone regeneration (continuation)	BCP/CHT	BMSCs	Gelatin microspheres laden with FGF	In vitro and in vivo	Cells seeded over porous BCP/CHT scaffolds incorporating FGF-laden gelatin microspheres were cultured in vitro in osteoblastic conditions before implantation in transcortical mandibular defects in skeletally mature female Yorkshire pigs.	FGF release enhanced new vascularization in the defect area and new bone formation.	[72]
		HUVECs BMSCs		In vitro and in vivo	Spheroids (2% HUVECs and 98% BMSCs) were cultured under osteogenic and endothelial medium before subcutaneous implantation in the dorsal region of 2 male nude mice.	Enhanced osteogenic differentiation associated to pre-vascularized spheroids of HUVECs/ BMSCs co-cultures.	[73]
	Hap	Periosteal graft		In vivo	Four different implants were inserted in premaxillary bone defects in rats; (1) premaxillar mucoperiosteal graft; (2) Hap/ premaxillar mucoperiosteal graft; (3) Hap/ femoral periosteal graft; (4) and femoral periosteal graft.	The periosteal graft provides satisfactory support to the Hap implant, allowing the growth of new bone.	[74]
		Periosteal graft	PRP	Clinical report	Membranous mandibular periosteum cultured in basal medium were applied in severe human alveolar bone defects.	Periosteal explant transplantation increased bone regeneration.	[75]
	BBM	PDLCs	PDGF-BB hBMP-2	In vitro	PDLCs seeded over BBM were cultured under PDGF-BB or rhBMP-2 supplemented media.	PDGF-BB improved cell proliferation, while rhBMP-2 did not support the cell mitosis.	[76]

Table I.2: Tissue engineering strategies for bone maxillofacial regeneration. (continued)

Clinical target	Scaffold	Cell type	Biochemical cues	Type of study	Experimental design	Outcomes	References
Maxillofacial bone regeneration (continuation)	Silk fibroin/ CHT (SFCS scaffolds)	Periosteal graft		In vivo	Autologous bone or SFCS were implanted over periosteal grafts placed over the latissimus dorsi muscle of adult sheep.	SFCS combined with periosteal graft produced comparable ectopic vascularized bone grafts as the autologous bone control.	[77]
	PLGA fleeces	PDPCs		In vitro and in vivo	Rabbit PDPCs seeded in PLGA fleeces were cultured in vitro in ONM. The tissue constructs were also implanted in critical size calvarial defects in New Zealand White Rabbits.	PDPCs/PLGA constructs expressed osteogenic markers in vitro and induced new bone grew not only from the margins of the defects but even from islands in the centre portion of the defect 4 weeks after implantation, leading to a full regeneration of the injury site.	[78]
	β-TCP	PDPCs BMSCs		In vitro and in vivo	Individual or co-cultures of human PDPCs and BMSCs were cultured in OM. PDPCs + BMSCs / β-TCP implants were inserted in the dorsal surface of CD-1 athymic and immunodeficient nude mice.	Co-culturing MSCs showed synergistic effect on osteogenic differentiation both in vitro and in vivo, enhancing ectopic bone growth and neovascularization.	[79]
	PGLA/β-TCP (cerasorbs) + fibrin	PDPCs	TGF-β1	In vitro	PDPCs were encapsulated into the PLGA/ β-TCP constructs within a fibrin matrix and cultured in OM + TGF-β1 supplementation up to 40 days.	De novo synthesis of human preosseous tissue. The addition of TGF-β1 increased new bone formation with significantly higher concentrations of osteogenic marker proteins.	[80]
	Fibrin/α-TCP	PDPCs	-	In vitro	Cells were embedded in fibrin beads containing 7.5% a-TCP particles. Beads were cultured in Ham's F-12 medium.	DNA content, alkaline phosphatase and osteocalcin content were significantly higher in the constructs containing α-TCP.	[81]

Table I.2: Tissue engineering strategies for bone maxillofacial regeneration. (continued)

Clinical target	Scaffold	Cell type	Biochemical cues	Type of study	Experimental design	Outcomes	References
Sinus floor Augmentation	B-TCP/Hap (Kasios)	BMSCs	-	Clinical report	BMSCs laden B-TCP/Hap scaffolds were implanted into the subantral sinus cavity in patients with loss of bone height in the posterior maxilla, before placement of metallic implants.	4 months after surgery, mean new bone formation was 41,34%. 93% of the implants were considered clinically successful 6 months post-implantation.	[82]
	BBM (Bio-Oss)	BMSCs from iliac crest	-	In vivo	Bilateral augmentations of the sinus floor in 6 adult sheep.	BMSCs combined with BBM consistently support new bone formation, 8 and 16 weeks after implantation.	[83]
	Collagen	PDPCs	-	Clinical	Removal of the bone, elevating the sinus membrane and implantation of the constructs.	Both strategies could create new bone tissue with sufficient stability for successful implant placement.	[84]
	BBM (Bio-Oss)	Autologous osteoblasts					
	PRP	BMSCs	-	Clinical report	BMSCs were combined with PRP and mixed with thronbine + CaCl2 to produce a cell-laden gel. Mucoperiosteal flap was elevated, and the injectable implants were applied in the maxillary sinus in patients' posterior alveolar ridge atrophy.	All 41 dental implants were clinically stable. Mineralized tissue height at 2 years increased 8.8±1.6mm. No adverse effects and remarkable bone absorption were seen in the 2–6-year follow-up time.	[85]
Maxillary Sinus Floor Elevation	BBM (Osteobone)	BMSCs-hBMP-2		In vivo	Cells were seeded in BBM and used in maxillary sinus floor elevation surgeries made bilaterally in Male New Zealand rabbits.	The BMSCs-hBMP-2 combined with BBM promoted new bone formation in rabbit maxillary sinus.	[86]

Table I.2: Tissue engineering strategies for bone maxillofacial regeneration. (continued)

Clinical target	Scaffold	Cell type	Biochemical cues	Type of study	Experimental design	Outcomes	References
Prosthodontic rehabilitation	PTTM-enhanced Ti implants	-	-	Pilot clinical cases	PTTM-enhanced titanium implants were placed in both maxilla and mandibles of postablative cancer patients.	PTTM-enhanced dental implants were clinically effective in the prosthetic rehabilitation of postoncological patients.	[60]
Temporal-mandibular joint replacement	BBM	BMSCs		In vitro	Culture for 5 weeks in a custom-made perfusion bioreactor.	Formation of confluent layers of lamellar bone and osteoids, homogeneously distributed throughout the scaffold.	[87]

α-MEM, alpha minimum essential medium; ASCs, adipose tissue derived stem cells; BCP, biphasic calcium phosphate; BBM, Bovine derived bone matrix; BMP-2, bone morphogenetic protein-2; BMSCs, bone marrow derived stem cells; BMSCs-hBMP-2, genetically modified BMSCs overexpressing recombinant human BMP-2; β-TCP, beta-tricalcium phosphate; CHT, chitosan; CPC, calcium phosphate cement; DMEM, Dulbecco´s modified medium; FGF-2, fibroblast growth factor-2, Hap, hydroxyapatite; HUVECs, human umbilical vein endothelial cells; MSCs, mesenchymal stem cells; NBM, natural bone mineral; OM, osteogenic medium; PCL, polycaprolactone; PDGF-BB, platelet derived growth factor; PDLCs, periodontal ligament cells; PDPCs, periosteal derived progenitor cells; PLGA, poly(glycolide-co-lactide) acid; PRP, platelet rich plasma; PS, polystyrene; PTTM, porous tantalum trabecular metal; TGF-β, transforming growth factor-beta; Ti, titanium.

1.5.1. Scaffolds

The use of "scaffolds" or engineered biomaterials, stems from the need for an adequate matrix to drive the regeneration of target tissues [61], [62]. Its function lies on providing structural support with adequate mechanical properties, architecture and volume mimicking tissue 3D environment, and biophysical/ biochemical cues for progenitor cells to attach, migrate, proliferate, generate their natural extracellular matrix (ECM), and differentiate until the mature tissue is fully regenerated. Scaffold´s bioactivity could be intrinsic to the material or achieved by functionalizing it structurally or with the incorporation of biochemical cues, as endogenous biomolecules, GFs, or ECM proteins [24], [88], [89]. An ideal scaffold should accomplish several requirements, such as biocompatibility, appropriate mechanical strength and degradation, adequate porosity, and pore interconnectivity [61], [62], [90]–[92].

Dental biomaterials have evolved from inert materials, aimed only at replacing and restoring dental structures, to bioactive biomaterials, which are designed to regenerate tissues and restore the natural functions of the tooth and its surrounding tissues [88]. The biomaterials that have been used for the regeneration of skeletal maxillofacial tissues can be inorganic, such as ceramics, metals, or metallic alloys, or organic, including both synthetic or natural origin molecules as polymers [62], [90].

1.5.1.1. Inorganic materials

Ceramic materials, such as β-tricalcium phosphate (β-TCP), hydroxyapatite (Hap), biphasic calcium phosphate (BCP) and calcium phosphate cements (CPC), or xenogenic bone mineral matrices, are the most used TE bone graft substitutes for the reconstruction of oral and maxillofacial region [58], [61], [67], [70], [76], [83], [84], [86], [90], [93]. The ceramics are highly biocompatible and closely resemble the natural bone apatite in terms of composition and compressive strength [58]. Their intrinsic osteogenic and osteoconductive properties have been widely explored alone [48], [65], [82]–[84], [86], [87] or in combination with other biomaterials [71], [72], [94]. Moreover, they can be produced in a large range of shapes, sizes, and porosity using industrialized manufacturing techniques, as 3D printing technologies [58], [61]. Although, their very low degradation rate [94], brittleness, and limited tensile strength [95], might compromise the quality of the regenerated tissues [96].

Metal alloys have also been used for their biocompatibility and osteointegrative potential. Brauner et al. demonstrated that porous tantalum trabecular metal (PTTM)-enhanced titanium

dental implants improved the osteointregation of the implants and, subsequently, boosted the efficacy of the clinical treatment used for the prosthodontic rehabilitation of post-ablative cancer patients submitted to post-surgery radiotherapy (Figure I.5 A) [60].

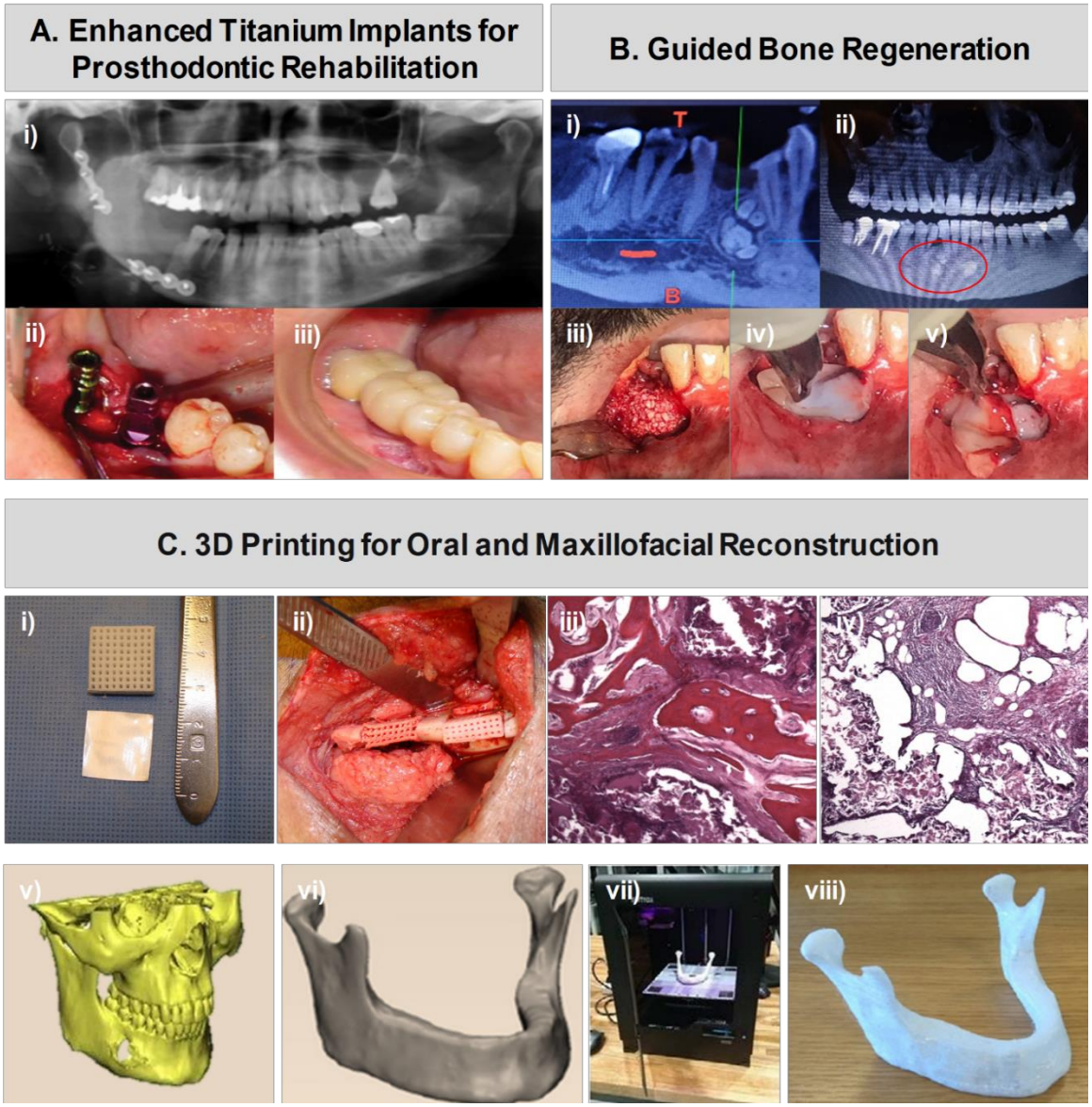

Figure I.5: Tissue engineering-based therapies for skeletal maxillofacial rehabilitation. (A) Porous tantalum trabecular metal (PTTM)-enhanced titanium dental implants for prosthodontic rehabilitation in postablative oral and maxillofacial cancer patients: (i) X-ray of the oral cavity after cancer treatments; (ii) implantation of the dental implants; (iii) post-implantation image of the oral cavity; adapted from [60]. B. Guided bone regeneration in a patient with an odontoma in 43 zone: odontome identification (i and ii); filling of the mandible defect with (iii) Bioss from Geistlich mixed with autologous liquid fibrin; (iv) covering with EPTFE membrane and (iii) PRF; courtesy from Dr. Antonio Dólera Ortiz. C. 3D printed TE scaffolds for bone resection reconstruction: (i) general appearance of PCL/β-TCP (1:1) 3D-printed scaffolds; (ii) scaffolds seeded with BMSCs (left) or unseeded (right), implanted in mandibular body osteotomies in Yucatan minipigs; (iii) new bone formation in the core of scaffolds seeded with BMSCs and (iv) absence of new bone in plain scaffolds, 8 weeks after implantation; adapted from [66]. Patient designed whole mandibule reconstruction: (v) original model of the cancerous mandible from patient's CT scan data; (vi) final 3D template of the reconstructed mandible; (vii) 3D printing, by fused deposition modelling in ABS polymer; (viii) reconstructed mandible implant; adapted from [66].

1.5.1.2. Synthetic polymeric materials

Several synthetic polymers are already approved by the FDA for biomedical applications [97], [98]. Among the most used synthetic polymers are poly(glycolic acid) (PGA), poly(lactic acid) (PLA), poly(glycolic-co-lactic acid) (PGLA), and polycaprolactone (PCL) [97], [98].

In general, these polymers are biodegradable and biocompatible and can be produced in highly controlled conditions, enabling to tailor their average molecular weight, porosity, mechanical properties, etc. TE has explored these materials to produce scaffolds with reproducible and predictable features, such as degradation kinetics or mechanical properties [58], [91]. However, synthetic polymeric biomaterials usually do not have adequate biofunctional cues to promote cellular attachment and differentiation [58]. So, synthetic polymeric biomaterials often require either some surface modification, or the blending with natural polymers (e.g. starch, chitosan (CHT)) or ceramics to enhance their biocompatibility and bioactivity [66], [78], [80]. In a pre-clinical study, Konopnicki and coworkers showed that 3D-printed scaffolds of poly(caprolactone) (PCL)/β-TCP (1:1) blends seeded with pig bone marrow cells were able to regenerate mandibular critical defects in minipigs (Figure I.5 C) [66].

1.5.1.3. Natural polymers

Several molecules derived from biologic/natural sources such as collagen [77], [84], [93], hyaluronic acid (HA) [94], [96], [99], fibrin [81], CHT [71], [72], [77], gelatin [72], or silk fibroin [77] are commonly used in TE. Most of them have already FDA approval for clinical use in temporary applications [58], [91]. Unlike synthetic polymers, the nature-derived polymers are more challenging to tailor and engineer using industrial processing technologies and present higher batch-to-batch variability. Nevertheless, their similarity with extracellular matrix, biocompatibility and intrinsic biofunctionality, make them ideal to functionalize other biomaterials or even be use as raw materials to produce matrices.

Collagen is the main structural protein present in the ECM of all the animals. Scaffolds based on collagen have been used in oral and maxillofacial applications as membranes [82], [83], [100], matrices [84], [93] or sponges [101]. For GBR, collagen membranes are able to avoid soft tissues collapse into bone defects while maintaining the ability space stability for new bone growth [82], [100]. Collagen matrices have been used for cells [84] or growth factors delivery [101] showing promising results in the regeneration of the skeletal maxillofacial defects by improving the cellular attachment and 3D spreading, and promoting faster new bone formation in clinical studies.

CHT is the de-acetylated derivative of chitin, commonly found in shells of marine crustaceans and cell walls of fungi. This linear β-(1-4) linked polysaccharide of glucosamine and N-acetyl glucosamine, is a polyvalent material used in TE applications as scaffolds, injectable hydrogels, microspheres, composites with ceramics [102] or as carrier agent both for cells and growth factors [77], [103]. For bone TE, CHT/calcium phosphate composites processed as porous scaffolds were shown to be valuable matrices to support bone and cartilage regeneration [71]. Along with CHT, the incorporation of calcium phosphates promotes osteogenic differentiation, new bone growth, and enhance the ability for osteoblasts to migrate through the pores of the scaffold [71], [72], [104].

HA is the backbone of vertebrates' ECM. Further than its structural role, HA is implied in several relevant biological processes such as angiogenesis and endothelial cell migration [105]. HA biocompatibility, degradability by means of hyaluronidases, and capacity to be modified through its carboxyl [106] and hydroxyl [107] groups to produce stable hydrogels makes it particularly interesting for TE. HA has been processed into microparticles capable of sustained drug delivery [106] or hydrogels [99], [107], [108] capable of supporting cell encapsulation. In particular, the HA microspheres, have been explored to be used as porogenic and drug delivery materials to enhance the degradability and osteoconductive/osteointegrative properties of injectable calcium phosphate cements [94], [96], [109]

Autologous fibrin- or platelet-rich blood derivatives have also been explored (figure I.7 B) as matrices for bone regeneration. The similarity of fibrin matrices with blood clot, namely the presence of cell- and GFs-binding motifs [110], [111], support their use in regenerative approaches. Despite fibrin's weak mechanical properties, fibrins matrices are excellent cells or GFs carriers, and can be incorporated with inorganic compounds, like ceramics (Figure I.5 B), in order to enhance their osteogenic properties [81], [112].

1.5.2. Cells

The inclusion of cells capable of participating in the regeneration of the tissue that is being replaced and integrate in host tissues is a keystone in TE strategies [90]. Stem cells are unspecialized cells with the ability for indefinitely self-renewal and differentiate into multiple cell lineages, capable of generating new tissues/organs or regenerate the existing ones [89], [113]–[117]. Moreover, they possess immunomodulatory properties down-modulating the immune reactions, therefore reducing the probability of graft failure, and attenuating the inflammatory

process [118], [119]. Also, they establish paracrine interactions with host cells, regulating their migration and differentiation into endowed cells of the target tissue [89], [119].

Commonly, stem cells are classified into three main types: embryonic stem cells (ESCs), usually isolated from the inner wall of the preimplantation blastocysts [90], [120], [121]; adult stem cells, found in adult tissues [115]; and induced pluripotent stem cells (iPSCs), which are produced artificially by genetic manipulation of somatic cells [121], [122].

While ESCs and iPSCs are pluripotent stem cells potentially capable to differentiate into all types of cells from the three germinal layers [90], [120], [122], their use in TE strategies is impaired by technical, ethical, and safety concerns [90], [122]. In contrast, adult stem cells can only differentiate into a restricted number of cell types from certain tissues [90], [113]. These cells, also named as postnatal stem cells, or somatic stem cells have been widely explored for TE applications.

1.5.2.1. Mesenchymal stem cells

Since the first isolation of clonogenic cells capable of multi-lineage differentiation in vitro from bone marrow, termed mesenchymal stem cells (MSCs) [123], different studies have shown that MSCs can be found in several tissues [113], [123]. Populations of MSCs-like cells have been found in periosteum, muscle, liver, brain, epithelium, skin, peripheral blood, umbilical cord blood, amniotic membrane, dental, and adipose tissues [61], [90], [113]. After harvesting, MSCs can expanded ex vivo, and then be induced to differentiate into the desired cell type.

MSCs from these sources exhibit the ability to undergo osteogenic, chondrogenic, and adipogenic differentiation in vitro [58], [124]–[131], however they have distinct differentiation potential, possibly due to niche effect [132]. Remarkably, these cells have immunomodulatory and chemotactic effects, preventing TE graft rejection and enhancing host regenerative potential [132], [133]. For bone TE, MSCs are most commonly obtained from bone marrow aspirates, adipose tissue, and periosteum.

1.5.2.1.1. Bone marrow derived stem cells

Bone marrow derived stem cells (BMSCs) are the most used MSCs in bone TE, and can be isolated from iliac crest aspirates, core biopsies, or surplus bone removed surgically [61]. The pre-culture in vitro in osteogenic conditions, incorporation into osteogenic biomaterials, and/or supplementation with growth factors have been explored by TE to engineer implantable grafts for critical bone defects regeneration. Urkmez et al., assessed the combinatory effect of porcine

BMSCs, and scaffolds composed of CHT flakes and BCP granules incorporating fibroblast growth factor (FGF) laden gelatin microspheres [72]. The cells pre-cultured under osteoblastic conditions and seeded onto the engineered scaffolds were able to induce new vascularization and new bone formation 8 weeks after implantation in transcortical mandibular defects in skeletally mature female Yorkshire pigs [72]. In another study, aiming to develop a successful sinus floor augmentation strategy for patients that had suffered a loss of height in the posterior maxilla, Shayesteh et al. implanted iliac crest´s BMSCs combined with porous Hap/TCP ceramic matrices [82]. Numerous areas of osteoid and orthotopic bone formation were seen 4 months after implantation, as confirmed by evaluation of biopsy specimens [82].

1.5.2.1.2. Periosteal-derived Progenitor Cells

Another interesting source of MSCs-like cells are the Periosteal-Derived Progenitor Cells (PDPCs). MSCs isolated from periosteum could be a useful resource for bone regeneration [113]. PDPCs have been shown to differentiate into several cell lineages such as osteogenic, adipogenic, chondrogenic and myogenic [58], [124]–[126].For bone TE, the PDPCs have been combined with osteogenic biomaterials, and/or GFs for oral and maxillofacial defects rehabilitation, presenting very good results in terms of new bone growth in critical defects, neovascularization, and higher osteogenic ability than BMSCs [74], [78]–[81], [84]. Redlich, et al., with the purpose of repairing critical size calvarial defects in New Zealand White Rabbits, seeded rabbits´ tibial periosteum PDPCs, cultured in osteogenic conditions, in PGLA fleeces (Ethisorb) [78]. The expression of osteogenic markers was observed in vitro and, 4 weeks after implantation, histological analysis revealed that the group treated with the biocomplex showed orthotopic new bone growth, not only from the margins of the defects but also from islands in the core of the defect, leading to a full regeneration of the injury site [78]. Arnold et al., using the same polymeric fleeces (Ethisorb) combined with β-TCP and transforming growth factor beta1 (TGF-β1), seeded the developed construct with PDPCs from human anteomedial portion of tibia and cultivated in vitro under osteogenic conditions [80]. After 40 days, histological images demonstrated that the samples that included TGF-β1 presented enhanced new bone formation and displayed significantly higher osteogenic markers expression than the constructs without GFs, whereas the inclusion of the inorganic part enhanced the osteoconductivity of the construct [80]. Remarkably, some studies have suggested that, the osteogenic potential of PDPCs is consistent, regardless the bone from which PDPCs were isolated [74].

1.5.2.1.3. Adipose tissue-derived stem cells

Adipose tissue-derived stem cells (ASCs) are MSCs obtained from the adipose tissues [134]. ASCs high abundance in adipose tissue, lower collection morbidity [128], [130], [131], higher proliferation rate in vitro comparing to BMSCs [90], [127], and osteogenic potential [127]–[131] has supporting ASCs as a good alternative to BMSCs for bone TE. Despite displaying lower osteogenic potential compared to BMSCs, it is maintained with aging, unlike the rest of the MSCs [135]–[137]. Clinical studies conducted by Mesimäki et al. or Sandor et al. showed that ASCs hold great potential in oral and maxillofacial rehabilitation [48], [65], [138]. They both combined autologous ASCs with a tricalcium phosphate scaffold and bone morphogenetic protein-2 (BMP-2) in order to repair critical maxillofacial defects, in patients subject to hemimaxillectomy due to a recurrent keratocyst or patients with anterior mandibular ameloblastoma resection defects, respectively [48], [65], [138]. The cytokines and chemokines produced by the transplanted ASCs acted as homing signals for endogenous stem cells and progenitor cells migration towards the site of injury [48], [65], [138]. This ability together with the osteoconductivity of the β-TCP acted synergistically in order to regenerate native-like bone 10 months after implantation in a parasymphyseal defect created by ameloblastoma resection, which allowed prosthodontic rehabilitation in the grafted site [48].

1.5.2.1.4. Dental pulp stem cells

The dental pulp is the soft tissue inside a tooth that contains neural fibers, blood vessels, lymphatics, and MSCs derived from the neural crest [139], [140]. Consequently, DPSCs have a strong differentiation potential towards the osteogenic lineage [141]. DPSCs have many advantages for bone TE, including high proliferation rate, excellent osteogenic differentiation potential, low donor site morbidity, and favorable paracrine and immunomodulatory properties [140], [142].

There are many different bone TE strategies using DPSCs in combination of scaffolds made of bone ECM [141], alginates [143], bioactive glass [144]–[146], CHT [144], [147], gelatin sponges [148], PCL [149], [150], and collagen [151], [152]. Other less conventional additives have been explored, to enhance the osteogenic differentiation of the DPSCs for bone regeneration, for example aloe vera [151], platelet-rich plasma (PRP) [153], parathyroid hormone [154], adenosine triphosphate (ATP) [155], tooth powder [156]; drug like aspirin [157], or berberine [158]; or even metal nanoparticles, such as iron [159] or gold [160].

D'Aquino et al. in order to fill the injury site left by the extraction of the mandibular third molar in patients that needed all wisdom teeth extraction seeded DPCs harvested from the extracted teeth onto a collagen sponge scaffold and implanted into the alveolar bone [161]. After 3 months, X-rays showed an optimal vertical repair of the alveolar bone tissue, whereas histological observations from biopsies clearly proved the complete regeneration of bone at the injury site and the enhancement of the expression of osteogenic markers [161]. Also, the combination in vitro of DPCs with HA hydrogels enriched with platelet lysate (PL) improved the osteogenic potential of the cells, increasing the cellular metabolism and stimulating the mineralized matrix deposition by DPSCs [162], and promotes implant vascularization [163].

1.5.2.1.5. Co-cultures

Other studies have procured to emulate the organogenesis, combining relevant cell types in co-cultures. Spheroid of human HUVECs and BMSCs (2:98), prevascularized after 10 days in culture, were implanted subcutaneous in the dorsal region of male mice resulting in a significantly increase of the osteogenic marker alkaline phosphatase (ALP) [73]. This study showed that combination with endothelial cells is likely to have a positive effect on the osteogenic differentiation of BMSCs [73].

In another study, Chen et al. co-culture BMSCs and PDPCs, both harvested from metaphyseal distal part of tibia, and loaded them into porous β-TCP scaffolds to evaluate their osteogenic potential and their capacity for ectopic bone growth [79]. Compared to single cultures, co-culturing MSCs in vitro showed abundant mineralization and a steadily increasing ALP activity and expression of osteogenic specific genes (COL1A1, BMP-2, osteopontin and osteocalcin) [79]. Eight weeks after implantation in the dorsal surface of CD-1 nude mice´s, similar synergistic effects were confirmed by histological observation of enhanced ectopic new bone formation and neovascularization [79].

1.5.3. Biochemical cues

GFs are secreted proteins which bind specific cellular receptors located on target cells to implement a desired function [90], [91]. These peptides activate the cellular signalling network, initiating several intracellular cascades that alter and influence many different cellular processes, such as the promotion or prevention of cell adhesion, proliferation, migration, and differentiation, the matrix deposition and the maturation of tissues [61], [90], [91]. The cellular response depends upon the GF, dose, the cell type, and the bound receptor. Hence, these molecules are

therapeutically applied in the regeneration of tissues aiming the enhancement of level of regeneration beyond the limit of spontaneous and natural tissue healing [90], [164].

Particularly for oral and maxillofacial reconstruction, the most used GFs are platelet-derived growth factor (PDGF) [76], [165], basic FGF (b-FGF) [72], insulin-like growth factor (IGF) [63], [70], [93], [162], [166], [167], TGF-β [70], [80], vascular endothelial growth factor (VEGF) [73], [163], [166] and bone morphogenetic proteins (BMPs) [48], [64], [65], [69], [70], [76]. These bioactive molecules can be used as a supplement for cell cultures, impregnated, or coated on the scaffolds [48], [64], [65], [69], [70], [72], [76], [80], [165], [167].

The morphogenic GFs, such as BMPs and TGF-β, have been widely used in skeletal maxillofacial regeneration for their ability to induce osteogenic differentiation, accelerating the production of bone ECM and, consequently, promote the tissue integration [168]. Specifically, BMPs are chemotactic, mitogenic, and osteogenic, recruiting MSCs from the surrounding tissues towards the bioengineered graft and inducing the differentiation of the recruited cells into the osteogenic lineage [61], [90], [168], [169].

Platelet-rich hemoderivatives (PRHds) are used for maxillofacial bone reconstruction since the 90's. Whitman et al. showed that PRP improve the aggregation and cohesiveness of particulate bone, enhancing the osteogenesis in palatal bone defects [170]. The PRHds are simple and cost-effective compositions containing supra physiologic concentrations of platelets, usually $1x10^6/\mu L$ [171] which, upon activation, release a cocktail of GFs and cytokines, that are essential in wound healing orchestration and regenerative processes, such as chemotaxis, cell proliferation and differentiation [28], [172]. Moreover, structural proteins and scaffold-forming elements, as fibrinogen (or its polymerized product fibrin) and fibronectin, which may act as temporary matrix for cell adhesion and migration, are also present in PRHds [28], [172]. Additionally, some PRHds have been reported to exhibit antimicrobial properties, which promotes the prophylaxis of the wound site [28], [107], [172].

Among the most clinically explored PRHds are the PRP and the platelet-rich fibrin (PRF), which have been shown to have therapeutic potential for osteointegration of implants [173] or as GTR occlusive barriers [174] (Figure I.12 B). Recent research on TE field has procured to use PRHds with more consistent batch-to-batch composition (e.g, platelet lysate) using standard preparation and activation protocols or pools of different donors, in order to overcome the therapeutic outcomes variability reported for these hemoderivatives [28], [172]. Likewise, PRHds

have been incorporated into smart materials in order to modulate the spatial-temporal release of the factors, enhancing host tissues healing potential [28], [172].

1.5.4. Bioreactors

Bioreactors have been explored in TE to mimic the human body biophysical, biochemical, and/or hydrodynamic conditions in a sterile, confined, and controlled environment. Four main bioreactor types have been used for bone tissue engineering [175]: spinner flasks [176], [177], rocker platforms [178], [179], rotating wall vessels [180], [181], compression [182], and perfusion systems [183], [184]. In general, these systems allow a more effective mass transport for feeding in the essential nutrients, cells, and oxygen and remove wastes and carbon dioxide, which yield more homogeneous colonization with cells and matrix deposition within large TE scaffolds [87], [175], [185]. Bioreactors can also provide complex biophysical stimuli, such as static and dynamic mechanical stresses, and magnetic or electrical signals [175].

The use of bioreactors has been proposed for recellularization of decellularized bone with autologous cells to treat large bone defects. It has been proposed as an alternative for those patients that are not candidates for additional surgery to bone graft harvest either due to radio- or chemotherapies, or to systemic conditions as malnutrition, a common consequence of maxillary neoplasm resection [175]. Some studies [87], [186]–[189] had reached good results regarding the clinical size, shape, and functionality of customized bone grafts using autologous stem cells and a bioreactor system to provide patient-specific bone grafts for maxillary reconstruction. In a study, scaffolds from fully decellularized bovine trabecular bone, anatomically shaped to resemble a human temporal-mandibular junction based on CT scans, were seeded with BMSCs and cultured with interstitial flow of culture medium in a perfusion bioreactor [87]. After 5 weeks of culture in dynamic conditions, tissue growth was evidenced by the formation of confluent layers of lamellar bone and osteoids, homogeneously distributed throughout the scaffold [87]. Conversely, statically cultured constructs exhibited empty pore spaces and loosely packed cells [87]. However, appropriate means to provide construct vascularization are still yet to be achieved [186].

1.5.5. Prophylactic tissue engineering constructs

Postoperative proliferation of residual tumor cells may result in the tumor recurrence, which has been strike with the irradiation or chemotherapy after tissue ablation. Given the impaired regenerative potential of irradiated tissues, successful bone regeneration combined with the control of residual cancer cells presents a challenge for bone tissue engineering.

Recently, has been explored the delivery of tumor suppressive drugs locally incorporated into the scaffolds to avoid the systemic administration of chemotherapy. Chai and coworkers, demonstrated that poly-cyclodextrin functionalized porous bioceramics laden with an antibiotic (gentamicin) and an anticancer agent (cisplatin) were cytocompatible and enabled the controlled release of the drugs [190]. Photothermal and magnetic hyperthermia therapies have also been developed, in which specific agents combined with TE scaffolds generate heat locally under near-infrared irradiation or magnetic stimulation respectively, to ablate tumor cells. Such agents include organic particles [191], gold nanoparticles [192], molybdenum sulfide (MoS_2) nanosheets [193], or graphene oxide (GO) [194], and magnetic nanoparticles [195].

1.6. Future perspectives and unmet challenges

The field of TE has substantially contributed for the development of therapies aiming the recovery of oral and maxillofacial tissues inflicted by neoplasms. In the particular case of skeletal maxillofacial tissues, two main lines have been approached: (i) the replacement of the "gold standard" bone flap autografts by engineered constructs; and (ii) the improvement of impaired regeneration of tissues following surgical resection of tumors and chemo or radiotherapy. Strategies combining biomaterials-based micro-engineered scaffolds, progenitor cells, and biophysical/ biochemical stimuli deeply contributed for the successful outcomes towards the development of successful bioengineered solutions. However, there are still controversial aspects to be clarified, such as the clinical use of GFs. For instance, the unpredictable effects and complications of BMP-supplemented treatments of oncogenic patients, led FDA to restrict the application of this GF to sinus alveolar process augmentation in the United States [196]. Likewise, the proper vascularization of bioengineered bone grafts, and the conjugation of adequate mechanical, processing, and biofunctional properties in a single construct are unmet challenges in bone TE. The bias responses in humans, highlights the complexity behind tissue regeneration after tumor development and defies for new therapeutic solutions with improved efficacy and systematic biological responses.

Overall, the future of TE in the rehabilitation of tissues affected by SMNs is unquestionable. Further than the sole fabrication of tissue substitutes, TE research is evolving to become a holistic research field addressing all the aspects of disease progression and post-implantation issues. The exploitation of imaging technologies and computer modeling to engineer patient-customized therapies [197]; the development of smart drug delivery strategies for spatio-temporal delivery of

GF [172]; the incorporation of molecules to prevent opportunistic microbial infections [107], [198], or tumor residence [191]–[195]; or even the development of in vitro models resourcing to artificial tissues to recreate the 3D tumor microenvironment and key physiological interactions [199]–[201], are driving the development of more efficient and personalized TE-based therapies for patients suffering from SMNs.

Recently, the emerging of microfabrication and 3D printing technologies have empowered the conventional TE approaches, enabling the preparation of hierarchically organized scaffolds emulating the complexity of tissue organization. Mimicking the 3D structural characteristics and functionality of the recessed tissues is one of the most challenging difficulties to overcome [58], [61]. The integration of imaging, CAD, and 3D printing technologies can be used to print anatomically identical models of complex bones, such as mandibles [202]. Moreover, the use of 3D printing technology has been explored to produce TE constructs closely mimicking bone microarchitecture [193]. However, in the particular case of bioprinting, which is the 3D printing of cells into constructs, available bioinks are still at an infancy stage and do not have the adequate mechanical properties or biofunctionality to reliably regenerate large bone defects [203].

TE research lines have also been exploring the cumulative experience in the preparation of artificial tissues to produce in vitro tumor models [199]–[201]. The ideal in vitro cancer models procure to mimic 3D microenvironment and key physiological interactions that are crucial to modulate tumor response to soluble paracrine factors, tumor drug resistance, and invasiveness. These models, further than providing a realistic platform which could potentially minimize the animal-based preclinical cancer models, might be equally essential to pave the way for personalized cancer medicine.

However, the costs for such therapies are still very high and will predictably be affordable just for wealthy populations in the near future, which raises funded ethical concerns. Hence, the future research trends of TE in oral and maxillofacial rehabilitation should focus on three main goals: (1) encourage the clinical translation of the most promising TE approaches for bone regeneration; (2) the development of new printable bioinks and technologies more stable, biofunctional, and cost effective, and its homologation for biomedical application; and, most importantly, (3) to disseminate/communicate this exciting field of knowledge to clinicians and healthcare providers so new solutions for the rehabilitation of SMNs can be successfully implemented, contributing for improved quality of life of patients.

1.7. References

[1] K. M. Galler and R. N. D'Souza, "Tissue engineering approaches for regenerative dentistry," *Regen. Med.*, vol. 6, no. 1, pp. 111–124, 2011, doi: 10.2217/rme.10.86.

[2] S. O. Griffin, J. A. Jones, D. Brunson, P. M. Griffin, and W. D. Bailey, "Burden of oral disease among older adults and implications for public health priorities," *Am. J. Public Health*, vol. 102, no. 3, pp. 411–418, 2012, doi: 10.2105/AJPH.2011.300362.

[3] B. Monse, R. Heinrich-Weltzien, H. Benzian, C. Holmgren, and W. Van Palenstein Helderman, "PUFA - An index of clinical consequences of untreated dental caries," *Community Dent. Oral Epidemiol.*, vol. 38, no. 1, pp. 77–82, Feb. 2010, doi: 10.1111/j.1600-0528.2009.00514.x.

[4] D. Herrera, S. Roldán, I. González, and M. Sanz, "The periodontal abscess (I). Clinical and microbiological findings," *J. Clin. Periodontol.*, vol. 27, no. 6, pp. 387–394, 2000, doi: 10.1034/j.1600-051x.2000.027006387.x.

[5] L. M. ROSENOER and A. SHEIHAM, "Dental impacts on daily life and stisfaction with teeth in relation to dental status in adults," *J. Oral Rehabil.*, vol. 22, no. 7, pp. 469–480, 1995, doi: 10.1111/j.1365-2842.1995.tb01191.x.

[6] P. T. N. Sarita, D. J. Witter, C. M. Kreulen, M. A. Van't Hof, and N. H. J. Creugers, "Chewing ability of subjects with shortened dental arches," *Community Dent. Oral Epidemiol.*, vol. 31, no. 5, pp. 328–334, Oct. 2003, doi: 10.1034/j.1600-0528.2003.t01-1-00011.x.

[7] C. Ritchie, K. Joshipura, R. A. Silliman, B. Miller, and C. W. Douglas, "Oral health problems and significant weight loss among community- dwelling older adults," *Journals Gerontol. - Ser. A Biol. Sci. Med. Sci.*, vol. 55, no. 7, 2000, doi: 10.1093/gerona/55.7.M366.

[8] A. Sheiham, J. G. Steele, W. Marcenes, S. Finch, and A. W. G. Walls, "The relationship between oral health status and Body Mass Index among older people: A national survey of older people in Great Britain," *British Dental Journal*, vol. 192, no. 12. Nature Publishing Group, pp. 703–706, Jun. 29, 2002, doi: 10.1038/sj.bdj.4801461.

[9] C. De Oliveira, R. Watt, and M. Hamer, "Toothbrushing, inflammation, and risk of cardiovascular disease: Results from Scottish Health Survey," *BMJ*, vol. 340, no. 7761, p. 1400, Jun. 2010, doi: 10.1136/bmj.c2451.

[10] P. Sjögren, E. Nilsson, M. Forsell, O. Johansson, and J. Hoogstraate, "A systematic review of the preventive effect of oral hygiene on pneumonia and respiratory tract infection in elderly people in hospitals and nursing homes: Effect estimates and methodological quality of randomized controlled trials," *J. Am. Geriatr. Soc.*, vol. 56, no. 11, pp. 2124–2130, Nov. 2008, doi: 10.1111/j.1532-5415.2008.01926.x.

[11] L. Winning and G. J. Linden, "Periodontitis and systemic disease," *BDJ Team*, vol. 2, no. 10, p. 15163, 2015, doi: 10.1038/bdjteam.2015.163.

[12] I. Eli, Y. Bar-Tal, and I. Kostovetzki, "At first glance: Social meanings of dental appearance," *J. Public Health Dent.*, vol. 61, no. 3, pp. 150–154, 2001, doi: 10.1111/j.1752-7325.2001.tb03382.x.

[13] J. M. Starr and R. Hall, "Predictors and correlates of edentulism in healthy older people," *Current Opinion in Clinical Nutrition and Metabolic Care*, vol. 13, no. 1. Curr Opin Clin Nutr

Metab Care, pp. 19–23, Jan. 2010, doi: 10.1097/MCO.0b013e328333aa37.

[14] T. M. Hassell, "Tissues and cells of the periodontium," *Periodontol. 2000*, vol. 3, no. 1, pp. 9–38, Oct. 1993, doi: 10.1111/j.1600-0757.1993.tb00230.x.

[15] J. M. Retrouvey, M. Goldberg, and S. A. Schwartz, "Dental Development and Maturation, From the Dental Crypt to the Final Occlusion," in *Pediatric Bone*, Elsevier Inc., 2012, pp. 83–108.

[16] G. S. Kumar, *Orban's oral histology and embryology*, 14th ed. Elsevier, 2015.

[17] S. Standring and H. Gray, *Gray's anatomy : the anatomical basis of clinical practice*. Churchill Livingstone/Elsevier, 2008.

[18] F. J. Hughes, "Periodontium and Periodontal Disease," in *Stem Cell Biology and Tissue Engineering in Dental Sciences*, Elsevier Inc., 2015, pp. 433–444.

[19] H. E. Schroeder and M. A. Listgarten, "The gingival tissues: the architecture of periodontal protection," *Periodontol. 2000*, vol. 13, no. 1, pp. 91–120, Feb. 1997, doi: 10.1111/j.1600-0757.1997.tb00097.x.

[20] P. M. Bartold, L. J. Walsh, and A. S. Narayanan, "Molecular and cell biology of the gingiva," *Periodontol. 2000*, vol. 24, no. 1, pp. 28–55, Oct. 2000, doi: 10.1034/j.1600-0757.2000.2240103.x.

[21] A. Nanci and D. D. Bosshardt, "Structure of periodontal tissues in health and disease," *Periodontology 2000*, vol. 40, no. 1. John Wiley & Sons, Ltd, pp. 11–28, Feb. 01, 2006, doi: 10.1111/j.1600-0757.2005.00141.x.

[22] J. Sodek and M. D. McKee, "Molecular and cellular biology of alveolar bone," *Periodontol. 2000*, vol. 24, no. 1, pp. 99–126, Oct. 2000, doi: 10.1034/j.1600-0757.2000.2240106.x.

[23] A. Nanci and A. R. TenCate, *Ten Cate's oral histology : development, structure, and function*, 9th ed. Elsevier, 2018.

[24] C. R. Silva, M. Gomez-Florit, P. S. Babo, R. L. Reis, and M. E. Gomes, "3D Functional scaffolds for dental tissue engineering," in *Functional 3D Tissue Engineering Scaffolds: Materials, Technologies, and Applications*, Elsevier, 2017, pp. 424–450.

[25] A. L. Boskey and P. G. Robey, "The Composition of Bone," in *Primer on the Metabolic Bone Diseases and Disorders of Mineral Metabolism: Eighth Edition*, Wiley Blackwell, 2013, pp. 49–58.

[26] S. Pérez and I. Tvaroška, "Chapter 1 - Carbohydrate–Protein Interactions: Molecular Modeling Insights," vol. 71, D. Horton, Ed. Academic Press, 2014, pp. 9–136.

[27] M. A. Peres *et al.*, "Oral diseases: a global public health challenge," *Lancet*, vol. 394, no. 10194, pp. 249–260, Jul. 2019, doi: 10.1016/S0140-6736(19)31146-8.

[28] P. S. Babo, R. L. Reis, and M. E. Gomes, "Periodontal tissue engineering: Current strategies and the role of platelet rich hemoderivatives," *J. Mater. Chem. B*, vol. 5, no. 20, pp. 3617–3628, 2017, doi: 10.1039/c7tb00010c.

[29] B. L. Pihlstrom, B. S. Michalowicz, and N. W. Johnson, "Periodontal diseases," in *Lancet*,

Nov. 2005, vol. 366, no. 9499, pp. 1809–1820, doi: 10.1016/S0140-6736(05)67728-8.

[30] B. A. Dye, "Global periodontal disease epidemiology," *Periodontol. 2000*, vol. 58, no. 1, pp. 10–25, Feb. 2012, doi: 10.1111/j.1600-0757.2011.00413.x.

[31] P. I. Eke *et al.*, "Update on Prevalence of Periodontitis in Adults in the United States: NHANES 2009 to 2012," *J. Periodontol.*, vol. 86, no. 5, pp. 611–622, May 2015, doi: 10.1902/JOP.2015.140520.

[32] D. A. Chaukar *et al.*, "Quality of life in head and neck cancer survivors: a cross-sectional survey," *Am. J. Otolaryngol.*, vol. 30, no. 3, pp. 176–180, May 2009, doi: 10.1016/j.amjoto.2008.05.001.

[33] J. Prein, "Review of Benign Tumors of the Maxillofacial Region and Considerations for Bone Invasion," in *Craniomaxillofacial Reconstructive and Corrective Bone Surgery*, New York, NY: Springer New York, pp. 59–64.

[34] A. El-Naggar, J. Chan, T. Takata, and P. Slooweg, Eds., *World Health Organization Classification of Tumours*. Lyon: International Agency for Research on Cancer, 2017.

[35] B. Mintz and R. A. Fleischman, *Tumors are often attributed to "uncontrolled growth' of cells. Yet it has become increasingly recognized that the problem*, vol. 34. 1981.

[36] M. Saalim, K. Sansare, F. R. Karjodkar, A. G. Farman, S. N. Goyal, and S. R. Sharma, "Recurrence rate of odontogenic myxoma after different treatments: a systematic review," *Br. J. Oral Maxillofac. Surg.*, pp. 7–13, 2019, doi: 10.1016/j.bjoms.2019.09.005.

[37] R. Agbara, B. Fomete, O. Athanasius-Chukwudi, O. Uchenna-Kevin, and S. Modupeola-Omotara, "Central Myxoma / Myxofibroma of the Jaws : A Clinico-Epidemiologic Review," vol. 29, no. 90, pp. 35–41, 2017.

[38] C. E. Anyanechi and B. D. Saheeb, "The Clinical Presentation of Odontogenic Myxoma of the Jaws: A 22-Year Retrospective Analysis," *J. Clin. Exp. Oncol.*, vol. 06, no. 05, 2017, doi: 10.4172/2324-9110.1000193.

[39] A. C. McClary *et al.*, "Ameloblastoma: a clinical review and trends in management," *Eur. Arch. Oto-Rhino-Laryngology*, vol. 273, no. 7, pp. 1649–1661, 2016, doi: 10.1007/s00405-015-3631-8.

[40] R. D. A. C. Almeida, E. S. D. S. Andrade, J. C. Barbalho, A. Vajgel, and B. C. D. E. Vasconcelos, "Recurrence rate following treatment for primary multicystic ameloblastoma: Systematic review and meta-analysis," *Int. J. Oral Maxillofac. Surg.*, vol. 45, no. 3, pp. 359–367, 2016, doi: 10.1016/j.ijom.2015.12.016.

[41] S. Amado Cuesta, J. Gargallo Albiol, L. Berini Aytés, and C. Gay Escoda, "Review of 61 cases of odontoma. Presentation of an erupted complex odontoma," *Med. Oral*, vol. 8, no. 5, p. 366—373, 2003.

[42] G. Isola, M. Cicciù, L. Fiorillo, and G. Matarese, "Association between odontoma and impacted teeth," *J. Craniofac. Surg.*, vol. 28, no. 3, pp. 755–758, 2017, doi: 10.1097/SCS.0000000000003433.

[43] T. Li, "The Odontogenic Keratocyst: A Cyst, or a Cystic Neoplasm?," *J. Dent. Res.*, vol. 90, no. 2, pp. 133–142, 2011, doi: 10.1177/0022034510379016.

[44] E. V. a Ahlfors, “The Odontogenic,” pp. 10–19, 1984.

[45] D. Dolanmaz, A. Esen, A. Mihmanlı, and K. Işık, “Management of central giant cell granuloma of the jaws with intralesional steroid injection and review of the literature,” *Oral Maxillofac. Surg.*, vol. 20, no. 2, pp. 203–209, 2016, doi: 10.1007/s10006-015-0530-5.

[46] N. B. Daroit, R. G. de Marco, M. Sant’Anna Filho, and G. G. Fritscher, “The challenge in the treatment of central giant cell granuloma – What is the best approach?,” *J. Oral Maxillofac. Surgery, Med. Pathol.*, vol. 29, no. 2, pp. 122–128, 2017, doi: 10.1016/j.ajoms.2016.05.009.

[47] J. Hupp, M. Tucker, and E. Ellis, *Contemporary Oral and Maxillofacial Surgery*, Sixth edit. St. Louis: Elsevier, Mosby, 2014.

[48] G. K. Sándor *et al.*, “Adipose Stem Cell Tissue–Engineered Construct Used to Treat Large Anterior Mandibular Defect: A Case Report and Review of the Clinical Application of Good Manufacturing Practice–Level Adipose Stem Cells for Bone Regeneration,” *J. Oral Maxillofac. Surg.*, vol. 71, no. 5, pp. 938–950, May 2013, doi: 10.1016/j.joms.2012.11.014.

[49] L. B. Moura *et al.*, “Autogenous non-vascularized bone graft in segmental mandibular reconstruction: a systematic review,” *Int. J. Oral Maxillofac. Surg.*, vol. 45, no. 11, pp. 1388–1394, 2016, doi: 10.1016/j.ijom.2016.05.004.

[50] T. Burk, J. Del Valle, R. A. Finn, and C. Phillips, “Maximum Quantity of Bone Available for Harvest From the Anterior Iliac Crest, Posterior Iliac Crest, and Proximal Tibia Using a Standardized Surgical Approach: A Cadaveric Study,” *J. Oral Maxillofac. Surg.*, vol. 74, no. 12, pp. 2532–2548, 2016, doi: 10.1016/j.joms.2016.06.191.

[51] T. M. Osborn, D. Helal, and P. Mehra, “Iliac crest bone grafting for mandibular reconstruction: 10-year experience outcomes,” *J. Oral Biol. Craniofacial Res.*, vol. 8, no. 1, pp. 25–29, 2018, doi: 10.1016/j.jobcr.2017.12.001.

[52] H. M. Hahn, Y. J. Lee, and D. H. Park, “Huge Radicular Cyst of the Maxilla Treated with Complete Resection and Immediate Reconstruction by Rib Bone Graft,” *J. Maxillofac. Oral Surg.*, vol. 18, no. 3, pp. 378–381, 2019, doi: 10.1007/s12663-018-1125-0.

[53] E. C. Sung, S. M. Chan, K. Sakurai, and E. Chung, “Osteonecrosis of the maxilla as a complication to chemotherapy: A case report,” *Spec. Care Dentist.*, vol. 22, no. 4, pp. 142–146, 2002, doi: 10.1111/j.1754-4505.2002.tb01178.x.

[54] R. A. Hitti, “Guided Bone Regeneration in the Oral Cavity: A Review,” *Open Pathol. J.*, vol. 5, no. 1, pp. 33–45, 2011, doi: 10.2174/1874375701105010033.

[55] T. Ettl, M. Gosau, R. Sader, and T. E. Reichert, “Jaw cysts - Filling or no filling after enucleation? A review,” *J. Cranio-Maxillofacial Surg.*, vol. 40, no. 6, pp. 485–493, 2012, doi: 10.1016/j.jcms.2011.07.023.

[56] R. Langer and J. Vacanti, “Tissue engineering,” *Science (80-.).*, vol. 260, no. 5110, pp. 920–926, May 1993, doi: 10.1126/science.8493529.

[57] S. O. Keyhan, H. Fallahi, A. Jahangirnia, S. M. R. Masoumi, M. H. Khosravi, and M. H. Amirzade-Iranaq, “Tissue Engineering Applications in Maxillofacial Surgery,” in *Stem Cells in Clinical Practice and Tissue Engineering*, InTech, 2018.

[58] J. L. Shaul, B. K. Davis, and K. J. L. Burg, "Regenerative Engineering in Maxillofacial Reconstruction," *Regen. Eng. Transl. Med.*, vol. 2, no. 2, pp. 55–68, 2016, doi: 10.1007/s40883-016-0009-4.

[59] M. Cuesta-Gil, S. Ochandiano Caicoya, F. Riba-García, B. D. Ruiz, C. Navarro Cuéllar, and C. Navarro Vila, "Oral Rehabilitation With Osseointegrated Implants in Oncologic Patients," *J. Oral Maxillofac. Surg.*, vol. 67, no. 11, pp. 2485–2496, 2009, doi: 10.1016/j.joms.2008.03.001.

[60] E. Brauner *et al.*, "Evaluation of highly porous dental implants in postablative oral and maxillofacial cancer patients: A prospective pilot clinical case series report," *Implant Dent.*, vol. 24, no. 5, pp. 631–637, 2015, doi: 10.1097/ID.0000000000000295.

[61] S. Mobini and A. Ayoub, "Bone Tissue Engineering in the Maxillofacial Region: The State-of-the-Art Practice and Future Prospects," vol. 1, no. 1, p. 8, 2016, doi: 10.22037/rrr.v1i1.10518.

[62] R. Rai, R. Raval, R. V. S. Khandeparker, S. K. Chidrawar, A. A. Khan, and M. S. Ganpat, "Tissue Engineering: Step Ahead in Maxillofacial Reconstruction.," *J. Int. oral Heal. JIOH*, vol. 7, no. 9, pp. 138–42, 2015, [Online]. Available: http://www.ncbi.nlm.nih.gov/pubmed/26435634%0Ahttp://www.pubmedcentral.nih.gov/articlerender.fcgi?artid=PMC4589709.

[63] T. Albrektsson and C. Johansson, "Osteoinduction, osteoconduction and osseointegration," *Eur. Spine J.*, vol. 10, pp. S96–S101, 2001, doi: 10.1007/s005860100282.

[64] Y. Steinhardt *et al.*, "Maxillofacial-derived stem cells regenerate critical mandibular bone defect," *Tissue Eng. - Part A.*, vol. 14, no. 11, pp. 1763–1773, 2008, doi: 10.1089/ten.tea.2008.0007.

[65] K. Mesimäki *et al.*, "Novel maxillary reconstruction with ectopic bone formation by GMP adipose stem cells," *Int. J. Oral Maxillofac. Surg.*, vol. 38, no. 3, pp. 201–209, 2009, doi: 10.1016/j.ijom.2009.01.001.

[66] S. Konopnicki *et al.*, "Tissue-Engineered Bone With 3-Dimensionally Printed β-Tricalcium Phosphate and Polycaprolactone Scaffolds and Early Implantation: An In Vivo Pilot Study in a Porcine Mandible Model," *J. Oral Maxillofac. Surg.*, vol. 73, no. 5, pp. 1016.e1-1016.e11, May 2015, doi: 10.1016/j.joms.2015.01.021.

[67] V. J. Cvetković, J. G. Najdanović, M. Vukelić-Nikolić, S. Stojanović, and S. J. Najman, "Osteogenic potential of in vitro osteo-induced adipose-derived mesenchymal stem cells combined with platelet-rich plasma in an ectopic model," *Int. Orthop.*, vol. 39, no. 11, pp. 2173–2180, 2015, doi: 10.1007/s00264-015-2929-x.

[68] S. Rumiński, I. Kalaszczyńska, A. Długosz, and M. Lewandowska-Szumieł, "Osteogenic differentiation of human adipose-derived stem cells in 3D conditions - comparison of spheroids and polystyrene scaffolds," *Eur. Cell. Mater.*, vol. 37, pp. 382–401, 2019, doi: 10.22203/eCM.v037a23.

[69] S. Hu *et al.*, "Thermally induced self-agglomeration 3D scaffolds with BMP-2-loaded core–shell fibers for enhanced osteogenic differentiation of rat adipose-derived stem cells," *Int. J. Nanomedicine*, vol. 13, pp. 4145–4155, 2018, doi: 10.2147/IJN.S167035.

[70] O. Lucaciu *et al.*, "Tissue engineered bone versus alloplastic commercial biomaterials in craniofacial reconstruction," *Rom. J. Morphol. Embryol.*, vol. 51, no. 1, pp. 129–136, 2010.

[71] M. D. Weir and H. H. K. Xu, "Culture human mesenchymal stem cells with calcium phosphate cement scaffolds for bone repair," *J. Biomed. Mater. Res. - Part B Appl. Biomater.*, vol. 93, no. 1, pp. 93–105, Apr. 2010, doi: 10.1002/jbm.b.31563.

[72] A. S. Urkmez, S. G. Clark, M. B. Wheeler, M. S. Goldwasser, and R. D. Jamison, "Evaluation of chitosan/biphasic calcium phosphate scaffolds for maxillofacial bone tissue engineering," *Macromol. Symp.*, vol. 269, no. 1, pp. 100–105, 2008, doi: 10.1002/masy.200850912.

[73] J. Rouwkema, J. De Boer, and C. A. Van Blitterswijk, "Endothelial cells assemble into a 3-dimensional prevascular network in a bone tissue engineering construct," *Tissue Eng.*, vol. 12, no. 9, pp. 2685–2693, 2006, doi: 10.1089/ten.2006.12.2685.

[74] P. H. F. Caria, E. Y. Kawachi, C. A. Bertran, and J. A. Camilli, "Biological Assessment of Porous-Implant Hydroxyapatite Combined With Periosteal Grafting in Maxillary Defects," *J. Oral Maxillofac. Surg.*, vol. 65, no. 5, pp. 847–854, 2007, doi: 10.1016/j.joms.2006.05.059.

[75] H. Mizuno, H. Kagami, J. Mase, D. Mizuno, and M. Ueda, "Efficacy of membranous cultured periosteum for the treatment of patients with severe periodontitis: a proof-of-concept study.," *Nagoya J. Med. Sci.*, vol. 72, no. 1–2, pp. 59–70, 2010, doi: 10.18999/nagjms.72.1-2.59.

[76] H. N. Vavouraki, X. E. Dereka, I. A. Vrotsos, and C. E. Markopoulou, "Ability of a bovine bone graft, alone or enriched with PDGF-BB or rhBMP-2, to promote human periodontal ligament (PDL) cells proliferation. A preliminary study," *Cell Tissue Bank.*, vol. 4, no. 1, pp. 17–23, 2003, doi: 10.1023/A:1026383604279.

[77] C. N. Ríos, R. J. Skoracki, M. J. Miller, W. C. Satterfield, and A. B. Mathur, "In vivo bone formation in silk fibroin and chitosan blend scaffolds via ectopically grafted periosteum as a cell source: a pilot study.," *Tissue Eng. Part A*, vol. 15, no. 9, pp. 2717–2725, 2009, doi: 10.1089/ten.tea.2008.0360.

[78] A. Redlich *et al.*, "Bone engineering on the basis of periosteal cells cultured in polymer fleeces," *J. Mater. Sci. Mater. Med.*, vol. 10, no. 12, pp. 767–772, 1999, doi: 10.1023/A:1008994715605.

[79] D. Chen *et al.*, "Co-culturing mesenchymal stem cells from bone marrow and periosteum enhances osteogenesis and neovascularization of tissue-engineered bone," *J. Tissue Eng. Regen. Med.*, vol. 6, no. 10, pp. 822–832, Nov. 2012, doi: 10.1002/term.489.

[80] U. Arnold, K. Lindenhayn, and C. Perka, "In vitro-cultivation of human periosteum derived cells in bioresorbable polymer-TCP-composites," *Biomaterials*, vol. 23, no. 11, pp. 2303–2310, 2002, doi: 10.1016/S0142-9612(01)00364-7.

[81] R. S. Spitzer, C. Perka, K. Lindenhayn, and H. Zippel, "Matrix engineering for osteogenic differentiation of rabbit periosteal cells using α-tricalcium phosphate particles in a three-dimensional fibrin culture," *J. Biomed. Mater. Res.*, vol. 59, no. 4, pp. 690–696, 2002, doi: 10.1002/jbm.1277.

[82] Y. S. Shayesteh, A. Khojasteh, M. Soleimani, M. Alikhasi, A. Khoshzaban, and N. Ahmadbeigi, "Sinus augmentation using human mesenchymal stem cells loaded into a β-tricalcium phosphate/hydroxyapatite scaffold," *Oral Surgery, Oral Med. Oral Pathol. Oral Radiol. Endodontology*, vol. 106, no. 2, pp. 203–209, 2008, doi: 10.1016/j.tripleo.2007.12.001.

[83] R. Gutwald *et al.*, "Mesenchymal stem cells and inorganic bovine bone mineral in sinus augmentation: comparison with augmentation by autologous bone in adult sheep," *Br. J. Oral Maxillofac. Surg.*, vol. 48, no. 4, pp. 285–290, 2010, doi: 10.1016/j.bjoms.2009.06.226.

[84] I. N. Springer *et al.*, "Two techniques for the preparation of cell-scaffold constructs suitable for sinus augmentation: Steps into clinical application," *Tissue Eng.*, vol. 12, no. 9, pp. 2649–2656, 2006, doi: 10.1089/ten.2006.12.2649.

[85] Y. Yamada *et al.*, "Injectable tissue-engineered bone using autogenous bone marrow-derived stromal cells for maxillary sinus augmentation: Clinical application report from a 2-6-year follow-up," *Tissue Eng. - Part A.*, vol. 14, no. 10, pp. 1699–1707, 2008, doi: 10.1089/ten.tea.2007.0189.

[86] X. J. Sun *et al.*, "Maxillary sinus floor elevation using a tissue engineered bone complex with BMP-2 gene modified bMSCs and a novel porous ceramic scaffold in rabbits," *Arch. Oral Biol.*, vol. 55, no. 3, pp. 195–202, 2010, doi: 10.1016/j.archoralbio.2010.01.006.

[87] W. L. Grayson *et al.*, "Engineering anatomically shaped human bone grafts," *Proc. Natl. Acad. Sci. U. S. A.*, vol. 107, no. 8, pp. 3299–3304, 2010, doi: 10.1073/pnas.0905439106.

[88] I. Medina-Fernandez and A. D. Celiz, "Acellular biomaterial strategies for endodontic regeneration," *Biomater. Sci.*, vol. 7, no. 2, pp. 506–509, 2019, doi: 10.1039/c8bm01296b.

[89] T. M. Botero and J. E. Nör, "Tissue Engineering Strategies for Endodontic Regeneration," *Stem Cell Biol. Tissue Eng. Dent. Sci.*, pp. 419–430, 2015, doi: 10.1016/B978-0-12-397157-9.00037-0.

[90] L. N. Melek, "Tissue engineering in oral and maxillofacial reconstruction," *Tanta Dent. J.*, vol. 12, no. 3, pp. 211–223, 2015, doi: 10.1016/j.tdj.2015.05.003.

[91] B. T. Smith, J. Shum, M. Wong, A. G. Mikos, and S. Young, "Bone tissue engineering challenges in oral & Maxillofacial surgery," in *Advances in Experimental Medicine and Biology*, vol. 881, Springer New York LLC, 2015, pp. 57–78.

[92] M. Mastrogiacomo *et al.*, "Tissue engineering of bone: Search for a better scaffold," *Orthod. Craniofacial Res.*, vol. 8, no. 4, pp. 277–284, 2005, doi: 10.1111/j.1601-6343.2005.00350.x.

[93] J. Eyckmans, "Periosteum Derived Progenitor Cells in Bone Tissue Engineering," *Unpubl. Thesis*, pp. 1–175, 2007.

[94] P. S. P. S. Babo, V. E. V. E. Santo, M. E. M. E. Gomes, and R. L. R. L. Reis, "Development of an Injectable Calcium Phosphate/Hyaluronic Acid Microparticles System for Platelet Lysate Sustained Delivery Aiming Bone Regeneration," *Macromol. Biosci.*, vol. 16, no. 11,

pp. 1662–1677, Nov. 2016, doi: 10.1002/mabi.201600141.

[95] M. Nilsson, L. Wielanek, J. S. Wang, K. E. Tanner, and L. Lidgren, "Factors influencing the compressive strength of an injectable calcium sulfate-hydroxyapatite cement," *J. Mater. Sci. Mater. Med.*, vol. 14, no. 5, pp. 399–404, 2003, doi: 10.1023/A:1023254632704.

[96] P. S. Babo, P. P. Carvalho, V. E. Santo, S. Faria, M. E. Gomes, and R. L. Reis, "Assessment of bone healing ability of calcium phosphate cements loaded with platelet lysate in rat calvarial defects," *J. Biomater. Appl.*, vol. 31, no. 5, 2016, doi: 10.1177/0885328216669474.

[97] P. A. Gunatillake, R. Adhikari, and N. Gadegaard, "Biodegradable synthetic polymers for tissue engineering," *Eur. Cells Mater.*, vol. 5, pp. 1–16, 2003, doi: 10.22203/eCM.v005a01.

[98] E. Marin, M. I. Briceño, and C. Caballero-George, "Critical evaluation of biodegradable polymers used in nanodrugs," *Int. J. Nanomedicine*, vol. 8, pp. 3071–3091, 2013, doi: 10.2147/IJN.S47186.

[99] R. M. A. Domingues *et al.*, "Development of Injectable Hyaluronic Acid/Cellulose Nanocrystals Bionanocomposite Hydrogels for Tissue Engineering Applications," *Bioconjug. Chem.*, vol. 26, no. 8, pp. 1571–1581, 2015, doi: 10.1021/acs.bioconjchem.5b00209.

[100] N. Ardjomandi, F. Duttenhoefer, S. Xavier, T. Oshima, A. Kuenz, and S. Sauerbier, "In vivo comparison of hard tissue regeneration with ovine mesenchymal stem cells processed with either the FICOLL method or the BMAC method," *J. Cranio-Maxillofacial Surg.*, vol. 43, no. 7, pp. 1177–1183, 2015, doi: 10.1016/j.jcms.2015.05.020.

[101] A. S. Herford and P. J. Boyne, "Reconstruction of Mandibular Continuity Defects With Bone Morphogenetic Protein-2 (rhBMP-2)," *J. Oral Maxillofac. Surg.*, vol. 66, no. 4, pp. 616–624, Apr. 2008, doi: 10.1016/j.joms.2007.11.021.

[102] J. M. Oliveira *et al.*, "Novel hydroxyapatite/chitosan bilayered scaffold for osteochondral tissue-engineering applications: Scaffold design and its performance when seeded with goat bone marrow stromal cells," *Biomaterials*, vol. 27, no. 36, pp. 6123–6137, Dec. 2006, doi: 10.1016/j.biomaterials.2006.07.034.

[103] A. Di Martino, M. Sittinger, and M. V. Risbud, "Chitosan: A versatile biopolymer for orthopaedic tissue-engineering," *Biomaterials*, vol. 26, no. 30, pp. 5983–5990, 2005, doi: 10.1016/j.biomaterials.2005.03.016.

[104] H. H. K. Xu, M. D. Weir, and C. G. Simon, "Injectable and strong nano-apatite scaffolds for cell/growth factor delivery and bone regeneration," *Dent. Mater.*, vol. 24, no. 9, pp. 1212–1222, Sep. 2008, doi: 10.1016/j.dental.2008.02.001.

[105] M. Slevin *et al.*, "Hyaluronan-mediated angiogenesis in vascular disease: Uncovering RHAMM and CD44 receptor signaling pathways," 2006, doi: 10.1016/j.matbio.2006.08.261.

[106] P. S. Babo, R. L. Reis, and M. E. Gomes, "Production and characterization of hyaluronic acid microparticles for the controlled delivery of growth factors using a spray/dehydration method," *J. Biomater. Appl.*, vol. 31, no. 5, pp. 693–707, 2016, doi: 10.1177/0885328216669475.

[107] P. S. Babo *et al.*, "Platelet Lysate-Loaded Photocrosslinkable Hyaluronic Acid Hydrogels for Periodontal Endogenous Regenerative Technology," *ACS Biomater. Sci. Eng.*, vol. 3, no. 7, pp. 1359–1369, 2017, doi: 10.1021/acsbiomaterials.6b00508.

[108] L. S. Neves *et al.*, "Injectable Hyaluronic Acid Hydrogels Enriched with Platelet Lysate as a Cryostable Off-the-Shelf System for Cell-Based Therapies," *Regen. Eng. Transl. Med.*, vol. 3, no. 2, pp. 53–69, Jun. 2017, doi: 10.1007/s40883-017-0029-8.

[109] P. S. Babo *et al.*, "The Role of a Platelet Lysate-Based Compartmentalized System as a Carrier of Cells and Platelet-Origin Cytokines for Periodontal Tissue Regeneration," *Tissue Eng. - Part A*, vol. 22, no. 19–20, pp. 1164–1175, Oct. 2016, doi: 10.1089/ten.tea.2016.0226.

[110] K. Adamson, E. Spain, U. Prendergast, N. Moran, R. J. Forster, and T. E. Keyes, "Fibrinogen Motif Discriminates Platelet and Cell Capture in Peptide-Modified Gold Micropore Arrays," *Langmuir*, vol. 34, no. 2, pp. 715–725, Jan. 2018, doi: 10.1021/acs.langmuir.7b03279.

[111] M. M. Martino, P. S. Briquez, A. Ranga, M. P. Lutolf, and J. A. Hubbell, "Heparin-binding domain of fibrin(ogen) binds growth factors and promotes tissue repair when incorporated within a synthetic matrix," *Proc. Natl. Acad. Sci.*, vol. 110, no. 12, pp. 4563–4568, Mar. 2013, doi: 10.1073/pnas.1221602110.

[112] Y. Yamada *et al.*, "Bone regeneration following injection of mesenchymal stem cells and fibrin glue with a biodegradable scaffold," *J. Cranio-Maxillofacial Surg.*, vol. 31, no. 1, pp. 27–33, 2003, doi: 10.1016/S1010-5182(02)00143-9.

[113] M. Tatullo, M. Marrelli, and F. Paduano, "The regenerative medicine in oral and maxillofacial surgery: The most important innovations in the clinical application of mesenchymal stem cells," *Int. J. Med. Sci.*, vol. 12, no. 1, pp. 72–77, 2015, doi: 10.7150/ijms.10706.

[114] D. Cyranoski, "The cells that sparked a revolution," *Nature*, vol. 555, no. 7697, pp. 429–430, Mar. 2018, doi: 10.1038/d41586-018-03268-4.

[115] N. Gurusamy, A. Alsayari, S. Rajasingh, and J. Rajasingh, *Adult Stem Cells for Regenerative Therapy*, 1st ed., vol. 160. Elsevier Inc., 2018.

[116] T. Gong, B. C. Heng, E. C. M. Lo, and C. Zhang, "Current Advance and Future Prospects of Tissue Engineering Approach to Dentin/Pulp Regenerative Therapy," *Stem Cells Int.*, vol. 2016, no. 1, 2016, doi: 10.1155/2016/9204574.

[117] L. A. Sharma and R. M. Love, *Scaffolds for regeneration of the pulp–dentine complex*, no. 2. Elsevier Ltd, 2019.

[118] G. T. J. Huang, S. Gronthos, and S. Shi, "Critical reviews in oral biology & medicine: Mesenchymal stem cells derived from dental tissues vs. those from other sources: Their biology and role in Regenerative Medicine," *J. Dent. Res.*, vol. 88, no. 9, pp. 792–806, 2009, doi: 10.1177/0022034509340867.

[119] H. Hong *et al.*, "Dental follicle stem cells rescue the regenerative capacity of inflamed rat dental pulp through a paracrine pathway," *Stem Cell Res. Ther.*, vol. 11, no. 1, pp. 1–16, 2020, doi: 10.1186/s13287-020-01841-1.

[120] D. Cyranoski, "How human embryonic stem cells sparked a revolution," *Nature*, vol. 555, no. 7697, pp. 428–430, Mar. 2018, doi: 10.1038/d41586-018-03268-4.

[121] M. Csete, *Regenerative Medicine*, Second Edi., no. in 2011. Elsevier Inc., 2013.

[122] J. Yu and J. A. Thomson, *Induced Pluripotent Stem Cells*, Fourth Edi. Elsevier, 2013.

[123] A. I. Caplan, "Mesenchymal stem cells," *J. Orthop. Res.*, vol. 9, no. 5, pp. 641–650, Sep. 1991, doi: 10.1002/jor.1100090504.

[124] C. De Bari *et al.*, "Mesenchymal multipotency of adult human periosteal cells demonstrated by single-cell lineage analysis," *Arthritis Rheum.*, vol. 54, no. 4, pp. 1209–1221, 2006, doi: 10.1002/art.21753.

[125] Y. S. Choi *et al.*, "Multipotency and growth characteristic of periosteum-derived progenitor cells for chondrogenic, osteogenic, and adipogenic differentiation," *Biotechnol. Lett.*, vol. 30, no. 4, pp. 593–601, 2008, doi: 10.1007/s10529-007-9584-2.

[126] D. W. Hutmacher and M. Sittinger, "Periosteal cells in bone tissue engineering," *Tissue Eng.*, vol. 9, no. SUPPL. 1, 2003, doi: 10.1089/10763270360696978.

[127] C. M. Cowan *et al.*, "Adipose-derived adult stromal cells heal critical-size mouse calvarial defects," *Nat. Biotechnol.*, vol. 22, no. 5, pp. 560–567, May 2004, doi: 10.1038/nbt958.

[128] J. R. Dudas *et al.*, "The osteogenic potential of adipose-derived stem cells for the repair of rabbit calvarial defects," *Ann. Plast. Surg.*, vol. 56, no. 5, pp. 543–548, May 2006, doi: 10.1097/01.sap.0000210629.17727.bd.

[129] S. Kern, H. Eichler, J. Stoeve, H. Klüter, and K. Bieback, "Comparative Analysis of Mesenchymal Stem Cells from Bone Marrow, Umbilical Cord Blood, or Adipose Tissue," *Stem Cells*, vol. 24, no. 5, pp. 1294–1301, May 2006, doi: 10.1634/stemcells.2005-0342.

[130] C. Pendleton, Q. Li, D. A. Chesler, K. Yuan, H. Guerrero-Cazares, and A. Quinones-Hinojosa, "Mesenchymal Stem Cells Derived from Adipose Tissue vs Bone Marrow: In Vitro Comparison of Their Tropism towards Gliomas," *PLoS One*, vol. 8, no. 3, p. e58198, Mar. 2013, doi: 10.1371/journal.pone.0058198.

[131] P. A. Zuk *et al.*, "Human adipose tissue is a source of multipotent stem cells," *Mol. Biol. Cell*, vol. 13, no. 12, pp. 4279–4295, Dec. 2002, doi: 10.1091/mbc.E02-02-0105.

[132] R. A. Musina, E. S. Bekchanova, A. V. Belyavskii, and G. T. Sukhikh, "Differentiation potential of mesenchymal stem cells of different origin," *Bull. Exp. Biol. Med.*, vol. 141, no. 1, pp. 147–151, 2006, doi: 10.1007/s10517-006-0115-2.

[133] L. Zhang *et al.*, "The Effects of Mesenchymal Stem Cells in Craniofacial Tissue Engineering," *Curr. Stem Cell Res. Ther.*, vol. 9, no. 3, pp. 280–289, 2014, doi: 10.2174/1574888x09666140213204202.

[134] A. O. Luby, K. Ranganathan, J. V. Lynn, N. S. Nelson, A. Donneys, and S. R. Buchman, "Stem cells for bone regeneration: Current state and future directions," *J. Craniofac. Surg.*, vol. 30, no. 3, pp. 730–735, 2019, doi: 10.1097/SCS.0000000000005250.

[135] A. Schäffler and C. Büchler, "Concise Review: Adipose Tissue-Derived Stromal Cells-Basic and Clinical Implications for Novel Cell-Based Therapies," *Stem Cells*, vol. 25, no. 4, pp. 818–827, 2007, doi: 10.1634/stemcells.2006-0589.

[136] O. G. Davies, P. R. Cooper, R. M. Shelton, A. J. Smith, and B. A. Scheven, "A comparison

of the in vitro mineralisation and dentinogenic potential of mesenchymal stem cells derived from adipose tissue, bone marrow and dental pulp," *J. Bone Miner. Metab.*, vol. 33, no. 4, pp. 371–382, 2015, doi: 10.1007/s00774-014-0601-y.

[137] N. Kishimoto and S. Tran, "Dedifferentiated Fat (DFAT) Cells: a cell source for oral and maxillofacial tissue engineering," *Oral Dis.*, vol. 24, no. 7, pp. 42–49, 2018, doi: 10.1111/ijlh.12426.

[138] G. B. Sándor, "Tissue engineering of bone: Clinical observations with adipose-derived stem cells, resorbable scaffolds, and growth factors," *Ann. Maxillofac. Surg.*, vol. 2, no. 1, p. 8, 2012, doi: 10.4103/2231-0746.95308.

[139] L. F. Pettersson, P. J. Kingham, M. Wiberg, and P. Kelk, "In Vitro Osteogenic Differentiation of Human Mesenchymal Stem Cells from Jawbone Compared with Dental Tissue," *Tissue Eng. Regen. Med.*, vol. 14, no. 6, pp. 763–774, 2017, doi: 10.1007/s13770-017-0071-0.

[140] T. Yasui *et al.*, "Isolation of dental pulp stem cells with high osteogenic potential," *Inflamm. Regen.*, vol. 37, no. 1, pp. 1–10, 2017, doi: 10.1186/s41232-017-0039-4.

[141] F. Paduano *et al.*, "Decellularized bone extracellular matrix and human dental pulp stem cells as a construct for bone regeneration," *J. Biomater. Sci. Polym. Ed.*, vol. 28, no. 8, pp. 730–748, 2017, doi: 10.1080/09205063.2017.1301770.

[142] Y. C. Lee, Y. H. Chan, S. C. Hsieh, W. Z. Lew, and S. W. Feng, "Comparing the Osteogenic Potentials and Bone Regeneration Capacities of Bone Marrow and Dental Pulp Mesenchymal Stem Cells in a Rabbit Calvarial Bone Defect Model," *Int. J. Mol. Sci.*, vol. 20, no. 20, 2019, doi: 10.3390/ijms20205015.

[143] S. Sancilio *et al.*, "Alginate/hydroxyapatite-based nanocomposite scaffolds for bone tissue engineering improve dental pulp biomineralization and differentiation," *Stem Cells Int.*, vol. 2018, 2018, doi: 10.1155/2018/9643721.

[144] C. Covarrubias, M. Cádiz, M. Maureira, I. Celhay, F. Cuadra, and A. von Marttens, "Bionanocomposite scaffolds based on chitosan–gelatin and nanodimensional bioactive glass particles: In vitro properties and in vivo bone regeneration," *J. Biomater. Appl.*, vol. 32, no. 9, pp. 1155–1163, 2018, doi: 10.1177/0885328218759042.

[145] S. P. Sevari, S. Shahnazi, C. Chen, J. C. Mitchell, S. Ansari, and A. Moshaverinia, "Bioactive glass-containing hydrogel delivery system for osteogenic differentiation of human dental pulp stem cells," *J. Biomed. Mater. Res. Part A*, 2019, doi: 10.1002/jbm.a.36836.

[146] J. Tsukamoto *et al.*, "Efficacy of a self-Assembling peptide hydrogel, spg-178-gel, for bone regeneration and three-dimensional osteogenic induction of dental pulp stem cells," *Tissue Eng. - Part A*, vol. 23, no. 23–24, pp. 1394–1402, 2017, doi: 10.1089/ten.tea.2017.0025.

[147] A. Bakopoulou *et al.*, "Dental pulp stem cells in chitosan/gelatin scaffolds for enhanced orofacial bone regeneration," *Dent. Mater.*, vol. 35, no. 2, pp. 310–327, 2019, doi: 10.1016/j.dental.2018.11.025.

[148] Q. Fu *et al.*, "Improved osteogenic differentiation of human dental pulp stem cells in a layer-by-layer-modified gelatin scaffold," *J. Biomater. Appl.*, vol. 33, no. 4, pp. 477–487, 2018, doi: 10.1177/0885328218799162.

[149] N. K. Oliveira *et al.*, "Osteogenic potential of human dental pulp stem cells cultured onto poly-ε-caprolactone/poly (rotaxane) scaffolds," *Dent. Mater.*, pp. 1–10, 2019, doi: 10.1016/j.dental.2019.08.109.

[150] N. Wongsupa, T. Nuntanaranont, S. Kamolmattayakul, and N. Thuaksuban, "Assessment of bone regeneration of a tissue-engineered bone complex using human dental pulp stem cells/poly(ε-caprolactone)-biphasic calcium phosphate scaffold constructs in rabbit calvarial defects," *J. Mater. Sci. Mater. Med.*, vol. 28, no. 5, pp. 1–13, 2017, doi: 10.1007/s10856-017-5883-x.

[151] I. M. V. Soares *et al.*, "The influence of Aloe vera with mesenchymal stem cells from dental pulp on bone regeneration: Characterization and treatment of non-critical defects of the tibia in rats," *J. Appl. Oral Sci.*, vol. 27, pp. 1–11, 2019, doi: 10.1590/1678-7757-2018-0103.

[152] F. Chamieh *et al.*, "Accelerated craniofacial bone regeneration through dense collagen gel scaffolds seeded with dental pulp stem cells," *Sci. Rep.*, vol. 6, no. November, pp. 1–11, 2016, doi: 10.1038/srep38814.

[153] L. Otero, N. Carrillo, J. L. Calvo-Guirado, J. Villamil, and R. A. Delgado-Ruíz, "Osteogenic potential of platelet-rich plasma in dental stem-cell cultures," *Br. J. Oral Maxillofac. Surg.*, vol. 55, no. 7, pp. 697–702, 2017, doi: 10.1016/j.bjoms.2017.05.005.

[154] X. Ge *et al.*, "Parathyroid hormone enhances the osteo/odontogenic differentiation of dental pulp stem cells via ERK and P38 MAPK pathways," *J. Cell. Physiol.*, no. June, pp. 1–13, 2019, doi: 10.1002/jcp.29034.

[155] K. E. Stovall *et al.*, " Adenosine triphosphate enhances osteoblast differentiation of rat dental pulp stem cells via the PLC–IP 3 pathway and intracellular Ca 2+ signaling ," *J. Cell. Physiol.*, no. June, pp. 1–10, 2019, doi: 10.1002/jcp.29091.

[156] J. Wu *et al.*, "The Conditioned Medium of Calcined Tooth Powder Promotes the Osteogenic and Odontogenic Differentiation of Human Dental Pulp Stem Cells via MAPK Signaling Pathways," *Stem Cells Int.*, vol. 2019, pp. 1–13, 2019, doi: 10.1155/2019/4793518.

[157] M. Yuan *et al.*, "Aspirin promotes osteogenic differentiation of human dental pulp stem cells," *Int. J. Mol. Med.*, vol. 42, no. 4, pp. 1967–1976, 2018, doi: 10.3892/ijmm.2018.3801.

[158] B. C. Xin, Q. S. Wu, S. Jin, A. H. Luo, D. G. Sun, and F. Wang, "Berberine Promotes Osteogenic Differentiation of Human Dental Pulp Stem Cells Through Activating EGFR-MAPK-Runx2 Pathways," *Pathol. Oncol. Res.*, 2019, doi: 10.1007/s12253-019-00746-6.

[159] Y. Xia *et al.*, "Injectable calcium phosphate scaffold with iron oxide nanoparticles to enhance osteogenesis via dental pulp stem cells," *Artif. Cells, Nanomedicine Biotechnol.*, vol. 46, no. sup1, pp. 423–433, 2018, doi: 10.1080/21691401.2018.1428813.

[160] Y. Xia *et al.*, "Gold nanoparticles in injectable calcium phosphate cement enhance osteogenic differentiation of human dental pulp stem cells," *Nanomedicine Nanotechnology, Biol. Med.*, vol. 14, no. 1, pp. 35–45, Jan. 2018, [Online]. Available: https://linkinghub.elsevier.com/retrieve/pii/S1549963417301612.

[161] R. D'Aquino *et al.*, "Human mandible bone defect repair by the grafting of dental pulp

stem/progenitor cells and collagen sponge biocomplexes," *Eur. Cells Mater.*, vol. 18, pp. 75–83, 2009, doi: 10.22203/eCM.v018a07.

[162] L. D. F. F. Almeida *et al.*, "Hyaluronic acid hydrogels incorporating platelet lysate enhance human pulp cell proliferation and differentiation," *J. Mater. Sci. Mater. Med.*, vol. 29, no. 6, p. 88, 2018, doi: 10.1007/s10856-018-6088-7.

[163] C. R. Silva *et al.*, "Injectable and tunable hyaluronic acid hydrogels releasing chemotactic and angiogenic growth factors for endodontic regeneration," *Acta Biomater.*, vol. 77, pp. 155–171, 2018, doi: 10.1016/j.actbio.2018.07.035.

[164] P. V. Giannoudis and I. Pountos, "Tissue regeneration: The past, the present and the future," *Injury*, vol. 36, no. SUPPL. 4, pp. 2–5, 2005, doi: 10.1016/j.injury.2005.10.006.

[165] Y.-M. Lee *et al.*, "The Bone Regenerative Effect of Platelet-Derived Growth Factor-BB Delivered With a Chitosan/Tricalcium Phosphate Sponge Carrier," *J. Periodontol.*, vol. 71, no. 3, pp. 418–424, 2000, doi: 10.1902/jop.2000.71.3.418.

[166] G. D. G. Barabaschi and V. Manoharan, "Engineering Mineralized and Load Bearing Tissues," *Adv. Exp. Med. Biol.*, vol. 881, pp. 79–94, 2015, doi: 10.1007/978-3-319-22345-2.

[167] L. Yin *et al.*, "Physicochemical and biological characteristics of BMP-2/IGF-1-loaded three-dimensional coaxial electrospun fibrous membranes for bone defect repair," *J. Mater. Sci. Mater. Med.*, vol. 28, no. 6, pp. 1–14, 2017, doi: 10.1007/s10856-017-5898-3.

[168] G. Chen, C. Deng, and Y.-P. Li, "TGF-β and BMP Signaling in Osteoblast Differentiation and Bone Formation," *Int. J. Biol. Sci*, vol. 8, no. 2, pp. 272–288, 2012, doi: 10.7150/ijbs.2929.

[169] P. J. Harwood and P. V. Giannoudis, "Application of bone morphogenetic proteins in orthopaedic practice: Their efficacy and side effects," *Expert Opinion on Drug Safety*, vol. 4, no. 1. pp. 75–89, Jan. 2005, doi: 10.1517/14740338.4.1.75.

[170] D. H. Whitman, R. L. Berry, and D. M. Green, "Platelet gel: An autologous alternative to fibrin glue with applications in oral and maxillofacial surgery," *J. Oral Maxillofac. Surg.*, vol. 55, no. 11, pp. 1294–1299, 1997, doi: 10.1016/S0278-2391(97)90187-7.

[171] R. E. Marx, "Platelet-Rich Plasma: Evidence to Support Its Use," *J. Oral Maxillofac. Surg.*, vol. 62, no. 4, pp. 489–496, 2004, doi: 10.1016/j.joms.2003.12.003.

[172] B. B. Mendes, M. Gómez-Florit, P. S. Babo, R. M. Domingues, R. L. Reis, and M. E. Gomes, "Blood derivatives awaken in regenerative medicine strategies to modulate wound healing," *Adv. Drug Deliv. Rev.*, vol. 129, pp. 376–393, Apr. 2018, doi: 10.1016/j.addr.2017.12.018.

[173] G. Weibrich, W. K. G. Kleis, W. E. Hitzler, and G. Hafner, "Comparison of the platelet concentrate collection system with the plasma-rich-in-growth-factors kit to produce platelet-rich plasma: a technical report.," *Int. J. Oral Maxillofac. Implants*, vol. 20, no. 1, pp. 118–23, Accessed: Jan. 26, 2020. [Online]. Available: http://www.ncbi.nlm.nih.gov/pubmed/15747683.

[174] J. H. Fu and H. L. Wang, "Platelet-rich plasma has no additional benefit during guided tissue regeneration procedure to significantly improve clinical attachment gains in the treatment

of periodontal intrabony defects," *Journal of Evidence-Based Dental Practice*, vol. 12, no. 1. pp. 5–7, Mar. 2012, doi: 10.1016/j.jebdp.2011.12.003.

[175] P. Amrollahi, F. Moghadam, and L. Tayebi, "Bioreactor design for oral and dental tissue engineering," in *Biomaterials for Oral and Dental Tissue Engineering*, vol. 361, no. 2, 2017, pp. 193–204.

[176] V. I. Sikavitsas, G. N. Bancroft, and A. G. Mikos, "Formation of three-dimensional cell/polymer constructs for bone tissue engineering in a spinner flask and a rotating wall vessel bioreactor," *J. Biomed. Mater. Res.*, vol. 62, no. 1, pp. 136–148, 2002, doi: 10.1002/jbm.10150.

[177] L. Meinel *et al.*, "Bone tissue engineering using human mesenchymal stem cells: Effects of scaffold material and medium flow," *Ann. Biomed. Eng.*, vol. 32, no. 1, pp. 112–122, 2004, doi: 10.1023/B:ABME.0000007796.48329.b4.

[178] L. A. Edwards and F. Hills, "(12) Patent Application Publication (10) Pub. No.: US 2012/0257061 A1," vol. 1, no. 19, 2012.

[179] P. S. P. Poh, D. W. Hutmacher, M. M. Stevens, and M. A. Woodruff, "Erratum: Fabrication and in vitro characterization of bioactive glass composite scaffolds for bone regeneration (Biofabrication (2013) 5 (045005))," *Biofabrication*, vol. 6, no. 2, 2014, doi: 10.1088/1758-5082/6/2/029501.

[180] Q. Qing-Qing, P. Ducheyne, and P. S. Ayyaswamy, "Fabrication, characterization and evaluation of bioceramic hollow microspheres used as microcarriers for 3-D bone tissue formation in rotating bioreactors," *Biomaterials*, vol. 20, no. 11, pp. 989–1001, 1999, doi: 10.1016/S0142-9612(98)00183-5.

[181] E. A. Botchwey, S. R. Pollack, E. M. Levine, and C. T. Laurencin, "Bone tissue engineering in a rotating bioreactor using a microcarrier matrix system," *J. Biomed. Mater. Res.*, vol. 55, no. 2, pp. 242–253, 2001, doi: 10.1002/1097-4636(200105)55:2<242::aid-jbm1011>3.3.co;2-4.

[182] W. Hoffmann, "Novel perfused compression bioreactor system as an in vitro model to investigate fracture healing," *Front. Bioeng. Biotechnol.*, vol. 3, no. February, pp. 1–6, 2015, doi: 10.3389/fbioe.2015.00010.

[183] F. W. Janssen, J. Oostra, A. Van Oorschot, and C. A. Van Blitterswijk, "A perfusion bioreactor system capable of producing clinically relevant volumes of tissue-engineered bone: In vivo bone formation showing proof of concept," *Biomaterials*, vol. 27, no. 3, pp. 315–323, 2006, doi: 10.1016/j.biomaterials.2005.07.044.

[184] T. Applications and B. E. T. Al, "Overview of Bioreactor Types," vol. 9, no. 3, 2003.

[185] M. Fröhlich, W. L. Grayson, D. Marolt, J. M. Gimble, N. Kregar-Velikonja, and G. Vunjak-Novakovic, "Bone Grafts Engineered from Human Adipose-Derived Stem Cells in Perfusion Bioreactor Culture," *Tissue Eng. Part A*, vol. 16, no. 1, pp. 179–189, Aug. 2009, doi: 10.1089/ten.tea.2009.0164.

[186] M. Frohlich, "Bone Grafts Engineered from Human Adipose-Derived," *Tissue Eng. Part A*, vol. 16, no. 1, pp. 179–189, 2010.

[187] P. F. Costa *et al.*, "Biofabrication of customized bone grafts by combination of additive

manufacturing and bioreactor knowhow," *Biofabrication*, vol. 6, no. 3, p. 035006, 2014, doi: 10.1088/1758-5082/6/3/035006.

[188] L. C. G. Chase, M. S. G. Rao, and M. S. Vemuri, "Mesenchymal Stem Cell Assays and Applications Methods in Molecular Biology," *Methods*, vol. 698, no. 5, p. 534, 2011, doi: 10.1007/978-1-60761-999-4.

[189] M. M. Stevens, R. P. Marini, D. Schaefer, J. Aronson, R. Langer, and V. P. Shastri, "In vivo engineering of organs: The bone bioreactor," *Proc. Natl. Acad. Sci. U. S. A.*, vol. 102, no. 32, pp. 11450–11455, 2005, doi: 10.1073/pnas.0504705102.

[190] F. Chai *et al.*, "Poly-cyclodextrin functionalized porous bioceramics for local chemotherapy and anticancer bone reconstruction," *J. Biomed. Mater. Res. Part B Appl. Biomater.*, vol. 102, no. 6, pp. 1130–1139, Aug. 2014, doi: 10.1002/jbm.b.33094.

[191] L. Cheng *et al.*, "PEGylated Micelle Nanoparticles Encapsulating a Non-Fluorescent Near-Infrared Organic Dye as a Safe and Highly-Effective Photothermal Agent for In Vivo Cancer Therapy," *Adv. Funct. Mater.*, vol. 23, no. 47, pp. 5893–5902, Dec. 2013, doi: 10.1002/adfm.201301045.

[192] J. L. Li, D. Day, and M. Gu, "Ultra-Low Energy Threshold for Cancer Photothermal Therapy Using Transferrin-Conjugated Gold Nanorods," *Adv. Mater.*, vol. 20, no. 20, pp. 3866–3871, Oct. 2008, doi: 10.1002/adma.200800941.

[193] X. Wang *et al.*, "A 3D-printed scaffold with MoS2 nanosheets for tumor therapy and tissue regeneration," *NPG Asia Mater.*, vol. 9, no. 4, pp. e376–e376, Apr. 2017, doi: 10.1038/am.2017.47.

[194] H. Ma *et al.*, "A Bifunctional Biomaterial with Photothermal Effect for Tumor Therapy and Bone Regeneration," *Adv. Funct. Mater.*, vol. 26, no. 8, pp. 1197–1208, Feb. 2016, doi: 10.1002/adfm.201504142.

[195] J. Zhang *et al.*, "3D-printed magnetic Fe 3 O 4 /MBG/PCL composite scaffolds with multifunctionality of bone regeneration, local anticancer drug delivery and hyperthermia," *J. Mater. Chem. B*, vol. 2, no. 43, pp. 7583–7595, 2014, doi: 10.1039/C4TB01063A.

[196] J. W. Hustedt and D. J. Blizzard, "The controversy surrounding bone morphogenetic proteins in the spine: a review of current research," *Yale J. Biol. Med.*, vol. 87, no. 4, pp. 549–561, Dec. 2014.

[197] O. Tao *et al.*, "The applications of 3D printing for craniofacial tissue engineering," *Micromachines*, vol. 10, no. 7, 2019, doi: 10.3390/mi10070480.

[198] R. Costa-Almeida *et al.*, "The effects of platelet lysate patches on the activity of tendon-derived cells," *Acta Biomater.*, Jan. 2018, doi: 10.1016/j.actbio.2018.01.006.

[199] M. Cortini, N. Baldini, and S. Avnet, "New Advances in the Study of Bone Tumors: A Lesson From the 3D Environment," *Front. Physiol.*, vol. 10, Jun. 2019, doi: 10.3389/fphys.2019.00814.

[200] M. Cavo, M. Caria, I. Pulsoni, F. Beltrame, M. Fato, and S. Scaglione, "A new cell-laden 3D Alginate-Matrigel hydrogel resembles human breast cancer cell malignant morphology, spread and invasion capability observed 'in vivo,'" *Sci. Rep.*, vol. 8, no. 1, p. 5333, Dec. 2018, doi: 10.1038/s41598-018-23250-4.

[201] C. Liu, D. Lewin Mejia, B. Chiang, K. E. Luker, and G. D. Luker, "Hybrid collagen alginate hydrogel as a platform for 3D tumor spheroid invasion," *Acta Biomater.*, vol. 75, pp. 213–225, Jul. 2018, doi: 10.1016/j.actbio.2018.06.003.

[202] M. I. Mohammed, A. P. Fitzpatrick, and I. Gibson, "Customised design of a patient specific 3D printed whole mandible implant," *KnE Eng.*, vol. 2, no. 2, p. 104, 2017, doi: 10.18502/keg.v2i2.602.

[203] A. Aldaadaa, N. Owji, and J. Knowles, "Three-dimensional Printing in Maxillofacial Surgery: Hype versus Reality," *J. Tissue Eng.*, vol. 9, pp. 1–5, Apr. 2018, doi: 10.1177/2041731418770909.

Chapter II.

Materials and Methods

Chapter II. Materials and Methods

Under the scope of this thesis, we ambitioned to optimized and test PL-m-CNCs cryogels that comply with the requirements of alveolar bone tissue. In this sense, we pretended to recapitulate the genesis of bone by developing a strategy that promotes the recruitment of STEM/progenitor cells from the surrounding tissues which differentiate into functional osteoblastic-like cells and lead to the deposition of mineralized matrix that resembles the alveolar bone in oral and maxillofacial defects. In the following chapter, all experimental procedures developed throughout this thesis are described in detail to allow their understanding and reproducibility as well as the rationale behind the materials and procedures selection for achieving the main objectives proposed by this thesis.

2.1 Materials

Adequate selection of biomaterials in TE is crucial for the success of the system under development since the material itself is a source of important biochemical and physical signals that allow the proliferation and differentiation of stem cells, aiming for the regeneration of injured tissues.

Different biomaterials were used for the optimization of the scaffolds. For this purpose, platelet lysate (PL) was elected as the matrix due to its enriched content in structural proteins and growth factors. Moreover, this low strength matrix was blended with cellulose nanocrystals modified with aldehyde groups (aCNCs) and/or modified with hydroxyapatite (m-CNCs) as cross-linkers and reinforcement nanofillers, aiming at the regeneration of bone tissue. A detailed description of the main characteristics of these materials as well as the motivation behind their selection is thoroughly described in the subsequent sections.

2.1.1 Cellulose Nanocrystals

Cellulose is the most ubiquitous, abundant, and renewable polymeric raw material available in nature from different vegetal, bacterial, and animal sources [1]–[6]. Regardless of its source, cellulose is described as a high-molecular-weight long-chain linear homo-polysaccharide consisting of D-anhydrous-glucopyranose linked by β(1→4) glycosidic bonds, in which every monomer unit is corkscrewed at 180° concerning its neighbours, and the repeating unit is frequently considered a dimer of glucose, known as cellobiose, as depicted in figure II.1 [1]–[6]. Several cellulose chains form elementary fibrils (protofibrils), which assemble into microfibrils

supported by van der Waals forces, as well as intra- and intermolecular hydrogen bonds [1]–[6]. Microfibrils´ diameter ranges from 5 to 50 nm and they can have up to several micrometers in length while presenting alternate crystalline (highly organized) and amorphous (disordered) regions [1]–[6]. These microfibrils assemble into larger units called macrofibrils, which in turn further form the familiar cellulose fibers [3].

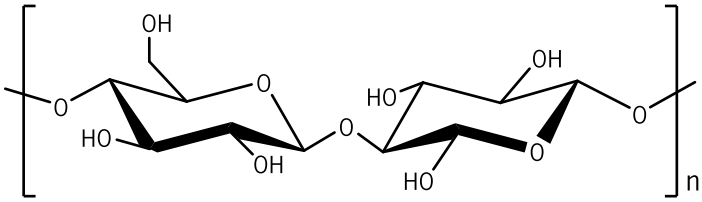

Figure II.1: Molecular structure of cellulose di-saccharide unit, known as cellobiose. This polysaccharide is composed of a dimer of D-anhydrous-glucopyranose units.

Controlled acid hydrolysis of cellulose fibers is the most common and well-known process used to synthesize cellulose nanocrystals (CNCs) [1]–[8]. By exploiting the hierarchical structure of native cellulose, this method promotes the selective degradation of the more accessible, disordered parts (amorphous regions), leading to the isolation of the typical crystalline rod-shaped CNCs, as demonstrated in figure II.2 [1]–[8]. The selection of the acid determines the properties of the resulting nanocrystals [8]. The most common acid used for the hydrolysis of cellulose is sulfuric acid, followed closely by hydrochloric acid [5]. Moreover, sulfuric hydrolysis allows to obtain not only isolated cellulose whiskers but also will make CNCs surface negatively charged due to the esterification of hydroxyl groups with sulphate groups [2], [5]–[8]. The incorporation of negatively charged sulphate groups on CNCs´ surface results in their high colloidal stability in aqueous suspension via electrostatic repulsion forces [2], [5], [8], [9]. This feature may also confer additional interesting functional properties to hydrogels, as this functionality is also characteristic of the ECM sulphated GAGs which are known to induce and control specific cell functions on the cellular microenvironment [10].

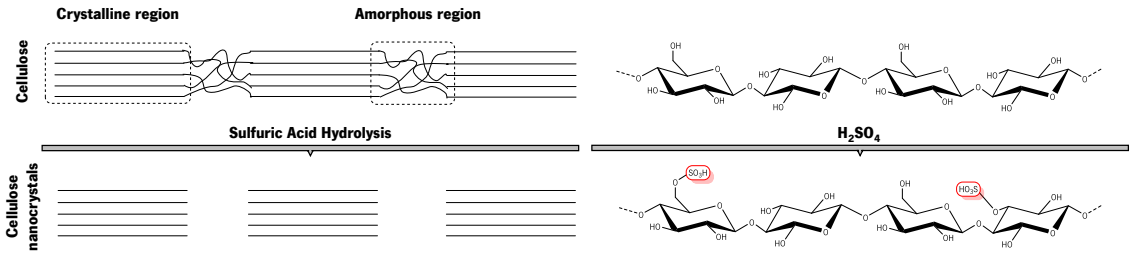

Figure II.2: Schematic representation of the chemical structure of cellulose depicting crystalline and amorphous regions and cellulose nanocrystals. After the process of sulfuric acid hydrolysis, the disordered amorphous regions are degraded and only the crystalline regions remain. The resultant cellulose nanocrystals exhibit a surface covered with hydroxyl and sulphate half-ester groups.

Depending on their source as well as the hydrolysis conditions, these elongated rod-like nanoparticles generally possess a width of about 3 – 50 nm and a length that ranges from 25 nm to several μm [3]–[6], [11], [12]. Additionally, along with general biocompatibility, CNCs present a high aspect ratio, low density (1.6 g/cm^3), high crystallinity, excellent mechanical properties (axial elastic modulus ranging from 110 to 220 GPa and tensile strength is in the range of 7.5 – 7.7 GPa), high surface area, and reactive surface chemistry (hydroxyl and sulfate side groups) [1], [3], [5], [6]. This last feature enables different surface modifications of CNCs, such as noncovalent modifications and covalent modifications, as oxidation, esterification, etherification, amidation, carbamation, nucleophilic substitution, silylation, or polymer grafting, leading to different functionalization of CNCs [4]–[6], [8]. These surface functionalizations (1) facilitate their self-assembly; (2) improve their colloidal stability to obtain better dispersion within a wide range of polymer matrices; (3) improve their compatibility by controlling the particle-particle and particle-matrix bond strength while trying to maintain CNCs original morphology and integrity [3]–[6]. All these properties render to CNCs the status of a potentially suitable candidate for various applications, as enzyme immobilization, synthesis of antimicrobial and medical materials, green catalysis, biosensing, bioimaging, drug delivery, and reinforcing nanofiller material for tissue engineering and regenerative medicine (TERM) approaches [3]–[6].

As nanofillers (incorporation without covalent attachment), CNCs have been widely studied in several bio-nanocomposites. Their incorporation has been shown to enhance the stability as well as the thermal and mechanical properties of polymer hydrogels based on gelatin [13], poly(vinyl alcohol) [14], [15], cyclodextrin [16], polycaprolactone [17], [18], polyethylene [19], polyethylene glycol [20], poly(N-isopropylacrylamide) [21], and carboxymethyl or hydroxyethyl cellulose [22], among others. For instance, our group has investigated the incorporation of CNCs on polycaprolactone/chitosan (PCL/CHT) nanofibrous scaffolds, which increased their mechanical performance by raising the biomaterial-toughing effect mechanical properties, as Young´s modulus and tensile strength, to tendon/ligament relevant range [23]. This reinforcing effect is attributed to the formation of a rigid CNCs network governed by the percolation threshold and the strong hydrogen bonding between them and with the matrix [24].

Further than nanofillers, CNCs can be covalently incorporated within polymeric matrices through specific aforementioned surface modifications to crosslink, for example, hydrogel systems. This usually results in improved stability, biochemical, and mechanical properties when compared

to the mere physical entrapment of CNCs within the gel matrix [13], [25], [26]. For instance, our group has previously used aldehyde-modified CNCs (a-CNCs) to reinforce and chemically crosslink platelet lysate-based hydrogel networks, which avoided the typical clot retraction and showed favoured retention of platelet-derived bioactive molecules [27], [28]. Moreover, these nanocomposite hydrogels allowed cell spreading and the formation of well-developed cellular networks.

2.1.2 Hydroxyapatite

Hap is the main mineral component of bone embedded between the ordered collagen fibers with c-axis orientation (along the length of the fibers), parallel to the longitudinal orientation of collagen. The term "apatite" describes a family of compounds that have similar chemical structures but not the same composition ($Ca_{10}(PO_4)_6X_2$), mainly composed of calcium phosphates [29]–[31]. Pure or stoichiometric calcium hydroxyapatite, commonly referred to as hydroxyapatite (Hap), $Ca_{10}(PO_4)_6(OH)_2$, with a Ca/P molar ratio of 1.67, is considered the most thermodynamically stable calcium phosphate salt at physiologic temperature and pH [29], [32], [33]. Moreover, Hap can exhibit either hexagonal or monoclinic crystal structures. The major differences between the monoclinic and hexagonal HAp is the hydroxyl groups orientation and the synthesis process, where hexagonal HAp is usually formed by precipitation from supersaturated solutions, while the monoclinic HAp is primarily formed by heating the hexagonal form at 850 °C in air and then cooling to room temperature (RT) [29], [32], [34]. However, from a chemical perspective, biologic and synthetic Hap, unlike the pure one, are non-stoichiometric due to the presence of ionic substituents in their crystalline structure, as Na^+, Mg^{2+}, Zn^{2+}, Sr^{2+}, K^+, F^-, Cl^-, Si^{4+}, HPO_4^{2-}, SiO_4^{4-}, and CO_3^{2-} [29], [31]–[36]. Therefore, impure biological apatites, frequently referred to as calcium deficient or carbonated hydroxyapatites, are the main mineral components of human bones and teeth enamel and dentin, being embedded between the oriented collagen fibers with c-axis orientation [30], [31], [36], [37].

During the past decades, different Hap production processes with precise control over its microstructure have been reported [38]. These methods can be classified into six distinct groups: 1) dry methods, which include the solid-state and mechanochemical procedures; 2) wet methods, which involve processes as chemical precipitation, emulsion, and hydrolysis, sol-gel, hydrothermal and sonochemical methods; 3) high-temperature processes that comprise the combustion and pyrolysis methods; 4) synthesis procedures based on biogenic sources; and 5) combination or

hybrid methods [38], [39]. Depending on the chosen synthesis method, Hap can possess different microstructures regarding its morphology, stoichiometry, crystallographic structure, and phase purity, which will, subsequently, affect its intrinsic properties [29], [38]. Hap has attracted great interest for TERM approaches owing to its excellent biological properties, namely its biocompatibility, producing non-toxic, non-inflammatory, and non-immunogenic responses [38], [40]–[42], affinity to biopolymers [37], [43]–[46], and bioactivity, through its osteoconductive [47]–[50], osteointegration [50], [51], and osteoinductive (in certain conditions) [52]–[56] features. On the other hand, Hap´s low mechanical properties represent its main disadvantage, limiting its usage in TERM strategies [30], [32]. Nevertheless, Hap is widely used for biomedical applications, mainly in the fields of orthopaedics, maxillofacial surgery, and dentistry, in different forms, as porous, dense, granules, blocks, or scaffolds, alone or as a composite with specific polymers or other ceramics, or as coatings for implants [30], [31]. Throughout the past years, Hap materials have been used as fillers, TERM scaffolds, drug delivery agents, and bioactive coatings on metallic implants for several bony, maxillofacial, and dental defects [32], [38], [57].

2.1.3 Platelet Lysate

Platelet lysate (PL) is obtained by freeze/thaw cycles or by ultrasounds that disrupt platelets´ membranes contained in platelet concentrates (PC) batches, produced either by centrifugation cycles or by apheresis [58]–[63]. This hemoderivative is a rich natural source of growth factors (GFs), cytokines, and structural proteins, essential for wound healing and regenerative stages [59], [60], [63], [64]. Among the GFs present in PL are platelet-derived growth factor (PDGF), transforming growth factors (TGF) -β1 and -β2, bone morphogenetic proteins (BMPs) -2, -4, and -6, vascular endothelial growth factor (VEGF), fibroblast growth factor (FGF), insulin-like growth factor (IGF), epidermal growth factor (EGF), epithelial cell growth factor (ECGF), and hepatocyte growth factor (HGF) [58], [59], [61], [64], [65]. They allow PL to be involved in several cellular processes, such as chemotaxis [66], cell proliferation [67] and differentiation, including angiogenesis [68], [69], chondrogenesis [70], and osteogenesis [71]–[73]. Additionally, PL contains fibrinogen (fibrin´s precursor), fibronectin, and vitronectin which may provide a temporary matrix for cell migration and adhesion [58], [60], [64].

PL presents numerous advantages over other platelet-rich hemoderivatives regarding therapeutic applications: 1) clot and platelet debris are removed during PL processing, therefore, PL is a solution that hardly forms spontaneously a gel or retracts; 2) PL is usually obtained from

outdated platelet concentrate units pools from different donors, thus, it is not necessary a blood collection from the patient; 3) freeze/thaw cycles are easy to standardize and do not require the addition of any clot activator to release the platelet factors; 4) the concentration of the (GFs) and cytokines are highly reproducible between batches, which can contribute for more predictable outcomes; 5) it can be frozen and stored to be readily available for further use; 6) PL exhibits antimicrobial properties which might reduce the recurrence of diseases and infections [58], [61], [74], [75]. Actually, PL has also been proposed as a prevailing alternative to fetal bovine serum supplement for culture of several human cell types [58].

For TERM applications, PL has been applied externally, loaded into carriers for the sustained release of PL bioactive molecules, injected directly into injured tissues, or as a scaffold for cell and/or biomolecules delivery [58], [64]. These constructs incorporating PL have shown potential to induce neovascularization [27], osteogenesis [63], [71], [76], to enhance periodontal re-attachment [77] and potential to enhance wound healing [78]. For example, the incorporation of PL into hyaluronic acid (HA) microparticles enhanced the biological performance and osteogenic potential of calcium phosphate cements through the sustained release of PL chemotactic and osteogenic GFs [63]. Moreover, the inclusion of PL in HA-based hydrogels improved their ability to recruit host cells and promote their sprouting, and also their pro-angiogenic properties [27]. Within this thesis, we reasoned that combining aldehyde-modified CNCs and hydroxyapatite coated CNCs into an PL-based cryogel would lead to a strategy that gathers improved mechanical properties with enhanced cellular signalling cues for applications in bone regeneration, as studied in chapter III.

2.2 Methods

2.2.1 Synthesis and functionalization of cellulose nanocrystals (CNCs)

2.2.1.1 Synthesis of cellulose nanocrystals (CNCs)

In this project, CNCs were isolated from microcrystalline cellulose (MCC, Sigma-Aldrich, USA), following a well-established sulfuric acid hydrolysis described by Bondeson *et al.* and adapted by Domingues *et al.* (Figure II.5). Briefly, 42 g of MCC were mixed with 189 mL of DI water with vigorous mechanical agitation for 20 min and at 500 rpm while cooled in an ice bath, and concentrated sulfuric acid (188.3 mL, 95-97% (v/v), Honeywell, USA) was added dropwise up to a final concentration of 64 wt%. The suspension was heated to 44°C in a pre-warmed water bath, under continuous stirring at 500 rpm for 2 h. Afterwards, the reaction was stopped by diluting the suspension with a 5-fold excess of cold deionized (DI) water and left to decant at 4°C for 2 h.

Thereafter, the supernatant was discarded, and the remaining suspension was successively centrifuged (Eppendorf 5810R, Germany) for 10 min at 3220 xg and 5°C, until the supernatant became turbid, with continuous replacement of the supernatant with DI water and subsequent resuspension of the solution in each cycle.

The resulting suspension was collected into dialysis membranes (MWCO: 14 kDa, Sigma-Aldrich, USA) and extensively dialyzed against DI water for a week until neutral pH was reached, with regular water replacement. Dialysis membranes were previously treated by washing and submerging them for 2 h in warm DI water several times. After dialysis, the content was sonicated with an ultrasonic processor (VCX750, Sonics & Materials Inc, USA) and using an ultrasound probe (½" Threaded End Part No. 630-0220) for 3 cycles of 5 min at 60% of amplitude output, under ice-cooling, to prevent overheating, which can lead to the desulfation of CNCs. The sonication process helps to disperse the CNCs avoiding the formation of possible aggregates and provides reasonable stability to the suspension. Then, the cloudy suspension was centrifuged one more time (10 min, 5°C, 3220 xg) to remove big particles aggregates and the final supernatant containing the CNCs was collected. The suspension of CNCs was further filtered using a vacuum pump chemically resistant (PTFE) (N820.3FT18, KNF Neuberger), and a fritted funnel D2. The concentration of CNCs in the final solution (stock solution) was determined gravimetrically to be 2.5 wt.% and was stored at 4°C until further use.

2.2.1.2 CNCs surface functionalization

2.2.1.2.1 Aldehyde functionalization of CNCs (a-CNCs)

As explained, CNCs can be modified to act as crosslinker agents through chemical functionalization of their surfaces. Periodate oxidation is a well-known method that induces the selective oxidative cleavage of the C2-C3 glycol bond of the glucose residues, resulting in the formation of dialdehyde groups at the respective carbon atoms along the cellulose chains (figure II.3) [10], [13], [79]. Therefore, under the scope of this thesis, the aldehyde functionalization of CNCs (a-CNCs) was obtained by sodium periodate oxidation route, according to the procedures described elsewhere with minor modifications [10], [13], [79].

In this sense, 3.95 g of sodium (meta) periodate ($NaIO_4$, Sigma Aldrich, Portugal) were added to 200 mL CNCs aqueous suspension (1.5 wt.%) in a 1:1 molar ratio ($NaIO_4$/CNCs). The suspension was stirred for 6 h protected from light exposure and at RT. Non-reacted periodate was quenched by the addition of 8 mL ethylene glycol (Sigma-Aldrich, Portugal). Thereafter, the solution

was loaded into dialysis membranes (MWCO: 14kDa, Sigma-Aldrich, USA), previously treated by washing and submerging them for 2 h in warm DI water several times, and then dialyzed against ultrapure water (Milli-Q, 18.2 MΩ.cm) for a week with regular water replacement. The final aldehyde-modified CNCs (a-CNCs) suspension was then collected and stored at 4°C until further use. To concentrate a-CNCs a reverse osmosis procedure was used. Briefly, a suspension of a-CNCs was concentrated against poly(ethylene glycol) (average MW 20,000 kDa, Sigma-Aldrich, USA) using benzoylated cellulose dialysis membranes (2000 Da NMWCO, Sigma-Aldrich, USA). The final a-CNC concentration was determined gravimetrically.

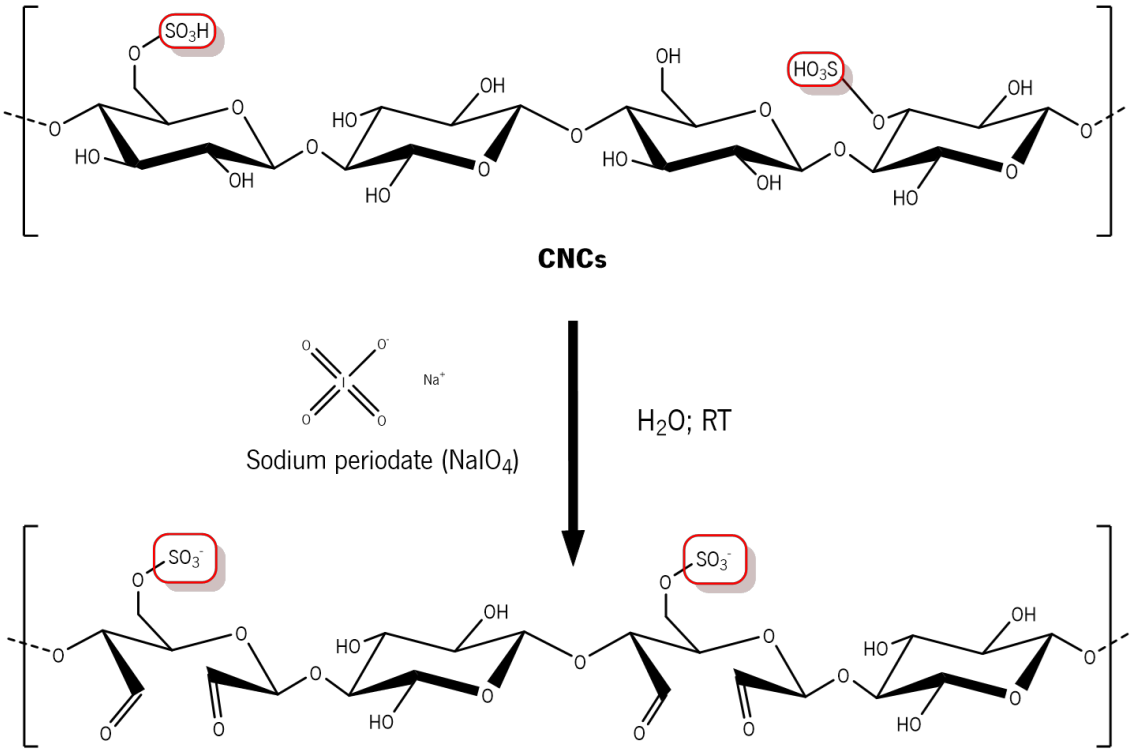

Figure II.3: CNCs surface oxidation. During the oxidation, the reaction of sodium periodate with the hydroxyl groups on CNCs surface leads to the formation of dialdehyde groups.

2.2.1.2.2 CNCs coating with hydroxyapatite (m-CNCs)

As explained, Hap possesses osteoconductive, osteointegrative, and osteoinductive properties, promotes the growth of new mineral material without causing any inflammatory response, and is an attractive material for biomedical applications, namely mineral tissue regeneration. Particularly, nanosized Hap, which has a high surface to volume ratio and ultrafine structure, can significantly improve cell adhesion and cell-biomaterial interactions [38]. Simulated body fluid (SBF) is a solution that mimics the natural composition and concentration of human blood plasma presented by Kokubo *et al.* in 1991 [48]. Besides being widely used to evaluate the

bioactivity of different materials [48], SBF can be used for decorating materials' surfaces with different kinds of apatite, including Hap [37], [43], [44]. Moreover, Hap crystals formed in SBF are nanosized and tend to grow and elongate in the c-axis (vertical orientation) resembling their natural orientation in real bone [80].

Moreover, during bone biomineralization, the deposition of apatite crystals within (intrafibrillar) and between (extrafibrillar) collagen fibrils has been suggested to be orchestrated by matrix non-collagenous proteins (NCPs), the arrangement of the tropocollagen molecules, fibril geometry, and water [81]. Although initially viewed as rather redundant and static acidic calcium binding proteins, NCPs are multifunctional proteins that actively participate in the organization of the ECM, coordination of cell-matrix and mineral-matrix interactions, and regulation of the mineralization process [82], [83]. NCPs, such as osteocalcin (OC) and osteopontin (OPN), are anionic matrix proteins able to regulate the sequestration of mineral ions to form metastable nanodroplets of amorphous calcium phosphate (ACP), which penetrate the interstices of collagen fibrils, later transforming into thermodynamically stable carbonated, calcium-deficient Hap [81], [84]. NCPs might not only stabilize the amorphous phase by inhibiting apatite nucleation, but also play an active role in aiding the formation of negatively charged complexes of mineral precursors that allow them to enter into collagen through electrostatic attraction and thus allowing the intrafibrillar collagen mineralization [84]. Moreover, the existence of positively charged domains in collagen fibrils provides binding sites for templating NCPs, which further contributes to the regulation of mineral deposition in an ordered manner [84].

Thus, NCPs ultimately control where and how much mineral crystal is deposited, as well as determining the quality and biomechanical properties of the mineralized matrix produced [83], [85]. Efforts to controllably mimic the process of nanoscale bone biomineralization date back to decades ago. These include the use of poly(amino acids) and synthetic organic polyelectrolytes early on, and have recently explored the use of self-assembling peptide-amphiphiles and anionic polymer acids to mimic the function of NCPs in templating Hap growth within collagen fibrils [81], [86]–[91].

In this sense, to mimic the nanoscale biomineralization process, particularly, the role of the acidic and negatively charged NCPs in bone formation, CNCs were used to promote Hap nucleation on their surface (figure II.4), inspired by the procedures described by the Salazar-Alvarez group [43], [92], adapted and optimized, as necessary. In this work, a simplified SBF (s-SBF)

without Mg^{2+}, HCO_3^-, and SO_4^{2-} was used to precipitate nano-Hap on the surface of CNCs, since these ions had a negative effect on the Hap coating formation due to their competition with Ca and P binding sites on CNCs surface.

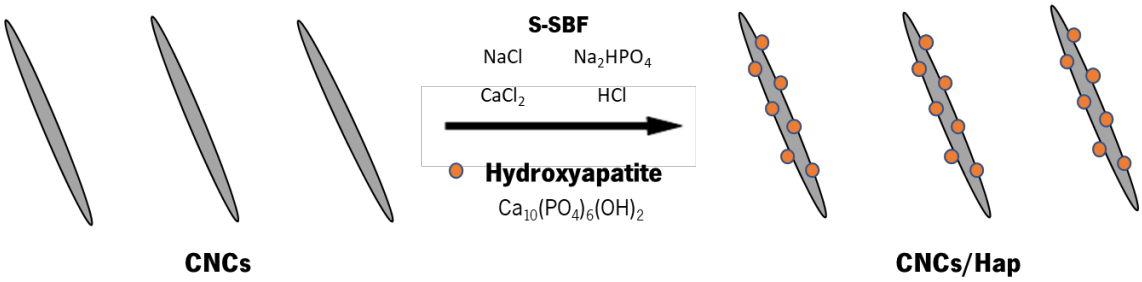

Figure II.4: Schematic representation of CNCs coating with hydroxyapatite using a s-SBF solution without Mg^{2+}, HCO_3^-, and SO_4^{2-}.

In brief, s-SBF solution composed of 140.0 mM sodium chloride (NaCl, Honeywell, USA), 2.5 mM calcium chloride hexahydrate ($CaCl_2.6H_2O$, Sigma-Aldrich, USA), 1.0 mM disodium hydrogen phosphate (Na_2HPO_4, 98%, abcr GmbH, Germany), and 20 mM hydrochloric acid (HCl, VWR, France) was prepared 24 h in advance and stored at RT preventing air and light exposure to avoid undesired precipitation. Thereafter, CNCs aqueous solution of 0.8% (w/v), prepared from the original CNCs stock solution (2.5 wt.%), was added to s-SBF in a closed flask in different amounts to obtain the calcium ion (in s-SBF) and sulfonic groups (in CNCs) molar ratio (Ca^{2+}/SO_3^-) of 10:1, 20:1, and 40:1. The suspension was then vigorously stirred using a magnetic stirrer until no bulk particles were apparent and then moved to an ultrasonic water bath (DT 100 H Sonorex Digitec, Bandelin, Germany) for 30 min to disperse evenly. Afterwards, the mixture pH was adjusted to two different values, 6.9 and 7.9, with the addition of tris(hydroxymethyl)aminomethane (Trisbase, Alfa Aesar, Germany), to avoid that Ca^{2+}/SO_3^- molar ratio was disturbed. After this, the solutions were placed in an orbital/linear thermostatic shaking water bath (OLS 200, Grant, UK) at 37°C and 150 rpm for 1 h. The ultrasound and shaking steps were repeated three times. Subsequently, the precipitated products were collected by centrifugation (Eppendorf 5810R, Germany) at 3220 xg and 15°C for 10 min and washed several times with anhydrous ethanol and ultrapure water (Milli-Q, 18.2 MΩ.cm) to remove the residual salts. Finally, m-CNCs nanocomposites were stored at 4 °C until further use.

2.2.2 Preparation of platelet lysate (PL)

PL used in this project was produced from outdated (> 5 days old) platelet concentrates (PC) obtained by plasma apheresis, provided by "Serviço de Imunohemoterapia do Centro

Hospitalar de São João" (CHSJ, Porto, Portugal), under a previously established cooperation protocol, approved by the Hospital Ethical Committee (approval number 363/18). The platelet count was performed at the CHSJ and the sample volume was adjusted to one million platelets per mL. All the lots were biologically qualified according to the Portuguese legislation (Decreto-Lei n.º 100/2011), and stored at -80°C five days after collection. PL was produced by three repeated freezing/thaw cycles to disrupt platelets and release their protein content [60], [61].

To obtain a more consistent content and a higher reproducibility of PL batches, PC lots from ten different donors, previously stored at -80°C, as above described (Figure II.5A), were thawed in a 37°C water bath and pooled (Figure II.5B) [61], [76], [93]. Thereafter, the suspension was subjected to another freezing/thaw cycle (frozen with liquid nitrogen at -196°C and thawed in a 37°C water bath) and aliquoted in several sterile tubes (Figure II.5C). The third cycle started by freezing all the aliquots in liquid nitrogen at -196°C before their storage at -80°C until further use (Figure II.5D). The last cycle was concluded just before use by thawing the PL in a 37°C water bath. Then, the cellular debris were removed by centrifugation at 3220 xg for 5 min (Figure II.5E), and the supernatant was filtered through 0.45 µm sterile filters (TPP, Switzerland) (Figure II.5F). All the experimental processing was performed in aseptic conditions.

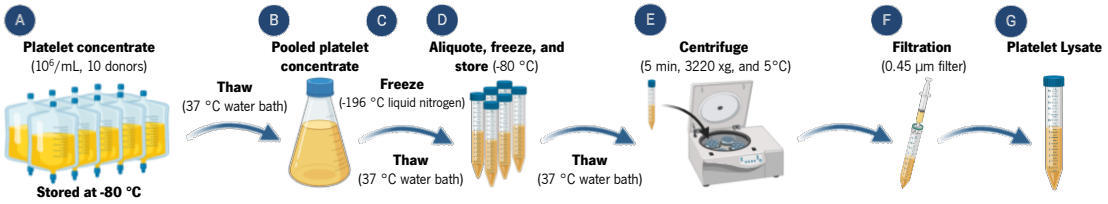

Figure II.5: Schematic representation of platelet lysate preparation from platelet concentrates.

2.2.3 Characterization of cryogel precursors

2.2.3.1 Physicochemical characterization

Zeta potential is a measure of the magnitude of the electrostatic or charge/repulsion between nanoparticles or molecules in a liquid medium [94]. Theoretical principles postulate that when a charged particle is suspended in a liquid, ions with opposite charge are attracted to the surface of the suspended particle [94]. Ions close to the particle surface are strongly bounded while ions that are further away are slightly bounded, forming a diffuse layer. Within this layer there is a notional boundary called slipping plane, and only the ions within this boundary will move with the particle when it moves in the liquid [94]. A difference of charge exists between the particle surface and the dispersing liquid, varying with the distance from the particle surface, being the charge at the slipping plane called the Zeta potential [94]. Zeta potential is measured using a combination of

two measurement techniques: electrophoresis and Laser Doppler Velocimetry, sometimes called Laser Doppler Electrophoresis, a method that measures how fast a particle moves in a liquid (particle velocity) when an electrical field is applied [94].

In the scope of this thesis, the Zeta potential was calculated for 0.1 w/v% suspensions of CNCs and m-CNCs in DI water. Briefly, 1 mL of each suspension was transferred into a Folded Capillary cell (DTS1060, Malvern) and zeta potential was measured by Zetasizer (Nano ZS, Malvern). Each analysis was performed in triplicate.

2.2.3.1.1 Conductometric titration of CNCs and a-CNCs

Conductometric titration is a quantitative technique that measures the conductivity of a solution as a titration proceeds, which has been widely used to study polyelectrolytic compounds in terms of complex composition, association phenomena, colloidal stability, and charged groups nature, content, and behaviour [95], [96]. The stoichiometric endpoints of titrated acids with bases and vice-versa are revealed by a minimum in the conductivity, showed by the interception between two straight-line segments tangential to the diminishing and increasing of the conductivity [96].

Regarding this, the amount of protonated sulfate half-ester groups introduced onto the surface of the CNCs during the hydrolysis reaction was determined by conductometric titration with sodium hydroxide (NaOH), following the procedure described elsewhere with minor adjustments [96], [97]. Succinctly, a CNCs suspension containing 150 mg CNCs was diluted with ultrapure water to give a total volume of 200 mL, followed by the addition of 2 mL NaCl solution (0.1 M, Honeywell, USA) for a final concentration of 1 mM NaCl. Thereafter, the solution was titrated with a solution of 10 mM NaOH (Panreac Quimica, Spain), added in 0.25 mL increments over 30-40 min with constant stirring to equilibrate the mixture after each NaOH addition. Titration conductivity values (μS/cm) were recorded using a conductivity meter (DDS-11AW, SCANSCI, UK) and corrected for dilution effects, and plotted against the added volume of NaOH. The typical titration curves show two distinct linear regions: (1) an initial decrease in conductivity with the added NaOH as the protons associated with the sulfate ester groups are consumed and (2) an increase in conductivity with the addition of NaOH which happens once all the charged groups have been neutralized [96]. Furthermore, the inflection point, determined by the intersection of the two linear regions, provides the volume of NaOH (V_{NaOH}) with a defined concentration (C_{NaOH}) required for the neutralization. Since this is related to the surface charge density of the crystallites, it can be

reported as percent sulphur content (%S) by weight, through the following calculation described in equation II.1 [98]:

$$\%\mathbf{S} = \frac{\mathbf{V_{NaOH} C_{NaOH} M_W(S)}}{\mathbf{m_{susp} C_{susp}}} \times \mathbf{100}\% \qquad \textbf{(Equation II.1)}$$

Where m_{susp} and c_{susp} are the mass and concentration (mass %) of the CNCs suspension and M_w (S) is the atomic mass of sulphur. The CNCs conductometric titration was performed in triplicate.

Moreover, the number of aldehyde groups on a-CNCs and the corresponding degree of oxidation were also quantified by acid-base conductometric titration after selectively oxidizing the aldehyde groups to carboxylic acid groups using silver(I) oxide, according to Yang *et al.* with minor modifications [25]. In a typical run, 3.6 mL of a-CNCs aqueous suspension (0.8 wt.%, 0.0288 g) and 0.025 g (0.62 mmol) of NaOH were dispersed in a final volume of 10 mL of ultra-pure water. Afterwards, 0.193 g of silver(I) oxide (Sigma-Aldrich, USA) were added to the solution, which was allowed to stir overnight, whilst selectively oxidizing the aldehyde groups to carboxylic acids. Next, to remove the unreacted silver particles, which may alter the reliability of the conductivity results, the suspension was centrifuged for 10 min at 3220 xg and 15 °C. Then, 5 mL of the supernatant from the centrifuged mixture were diluted with 80 mL of ultrapure water and the pH was adjusted to 3.5 with 1M HCl (VWR, France) added dropwise. Later, the solution was titrated using a 0.01M NaOH solution, added in 0.25 mL increments for 30-40 min with constant stirring to equilibrate the mixture after each NaOH addition. Lastly, the conductivity values, registered using a conductivity meter (DDS-11AW, SCANSCI, UK) were plotted against the volume of NaOH (in mL) and used to determine the content of carbonyl groups. The total amount of carboxyl groups corresponding to the carbonyl content, or the degree of oxidation (DO) was calculated from equation II.2:

$$\mathbf{DO} = \frac{\mathbf{162C(V_2 - V_1)}}{\mathbf{w - 36C(V_2 - V_1)}} \qquad \textbf{(Equation II.2)}$$

where C is the NaOH concentration (mol/L), V_1 and V_2 are the amount of NaOH shown in conductimetric titration curves, and w (g) is the weight of a-CNCs [99]. The conductometric titrations were performed in triplicate.

2.2.3.1.2 Fourier Transform Infrared Spectroscopy (FTIR)

Fourier Transform Infrared Spectroscopy (FTIR) is an infrared (IR) spectroscopy technique that is based on the measurement of the absorption (or transmission) of infrared radiation by a

material as a function of wavelength (or frequency), being their plot known as IR spectrum [100]. The absorption of infrared radiation results in transitions between quantized vibrational energy states of a molecule [100]. So, when a sample is exposed to IR radiation, different functional groups will absorb the energy of the radiation at specific wavelengths characteristic of each group, which is equal to the energy of a vibrational transition of each functional group [100]. Since each molecule has a unique IR spectrum often referred to as the "fingerprint", its identification can be achieved by comparing its absorption peak to a reference bank of spectra. Therefore, this technique allows the chemical analysis of the molecular composition of samples, the quantitative determination of species in complex mixtures, the determination of the molecular composition of surface species, the differentiation of structural and geometric isomers, and the determination of molecular orientation in polymers and solutions, of a wide variety solid, liquid, or gas specimens [100].

Furthermore, FTIR spectroscopic measurements can be obtained by transmission, reflectance, or attenuated total reflectance (ATR) methodologies. In this work, only transmission and ATR modes were applied. For traditional transmission FTIR, the incident IR radiation passes directly through the sample while for the ATR technique, IR radiation passes through an internal reflection element (IRE) crystal material, which surface is in contact with the sample to be measured and as the IR light passes through the IRE crystal it interacts at the crystal/sample interface [101]. Since the depth of penetration is very small, the ATR spectrum primarily provides information about the sample surface or the sample closest to the IRE surface and will not yield information of the bulk sample properties, which can be achieved by the conventional FTIR [100].

Regarding this work, to evaluate the modification of CNCs, FTIR spectroscopy was applied to acquire information about the characteristic absorbance peaks of functional groups in CNCs before and after the functionalization. For this purpose, Hap, CNCs, a-CNCs, and m-CNCs freeze-dried samples were used for FTIR analysis. The spectra of all samples were collected using an FTIR spectrophotometer (IRPrestige 21, Shimadzu, Japan), in 400–4000 cm^{-1} range, recording 32 scans at a resolution of 4 cm^{-1}. All data was analysed and processed using OriginPro 2018.

2.2.3.1.3 X-Ray Diffraction (XRD)

X-ray diffraction (XRD) is a non-destructive technique used for the characterisation of the crystalline or semi-crystalline structure of materials by measuring the average spacing between layers or rows of atoms [102]. This methodology provides information on their structures, phases, preferred crystal orientations (texture), and other structural parameters, such as average grain size

and shape, crystallinity, strain, and crystal defects [102]. Moreover, it also allows to study the deviation of a particular component from its ideal composition and/or structure [102].

The working principle behind this method is based on the scattering of a collimated beam of x-rays by the periodic lattice of a material, as a result of the interactions of the photons with the electrons of the material [102]. Each crystalline material has a characteristic atomic structure, which upon irradiation with x-rays causes a constructive and destructive interference of the scattered x-ray beam, at specific angles, generating a unique diffraction pattern that presents several peaks, known as Bragg diffraction peaks [102]. Consequently, the XRD pattern is the "fingerprint" of periodic atomic arrangements of each material. The diffraction of X-rays by a crystal is described by the Bragg law that relates the wavelength of the x-rays to the interatomic spacing and is given by the equation II.3:

$$\mathbf{2d \sin \theta = n\lambda} \qquad \textbf{(Equation II.3)}$$

where d is the perpendicular distance between pairs of adjacent planes, θ is the angle of incidence or Bragg angle, λ is the wavelength of the beam, and n denotes an integer number, known as the order of the reflection and is the path difference, in terms of wavelength, between waves scattered by adjacent planes of atoms [102]. XRD patterns of the crystalline samples reveal the presence of well-defined peaks at specific scattering angles, while amorphous samples show an intensity maximum that extends over several degrees (2θ).

Regarding the crystallite size, XRD can provide additional information that can be used to calculate the average crystallite size by the peak broadening of the diffraction peaks using the Scherrer equation (equation II.4):

$$\mathbf{t = \frac{k\lambda}{\beta \cos \theta}} \qquad \textbf{(Equation II.4)}$$

where t is the crystallite size, λ is the wavelength of the incident x-ray beam, β is the full width at half of the maximum intensity of the reflection peak, and k is the Scherrer constant [102].

Experimentally, samples from CNCs and m-CNCs formulations were freeze-dried and then pressed on the sample holder to form a uniform film of material for analysis. The XRD diffraction patterns measurements were performed using a conventional Bragg–Brentano diffractometer (Bruker D8 Advance DaVinci, Germany) equipped with Cu Kα radiation. Data sets were collected in the 2θ range of 10–80° with a step size of 0.05° and 1 s for each step and processed using

OriginPro 2018 software. Subsequently, the average crystallite size was calculated using the Scherrer equation.

2.2.3.1.4 Energy-Dispersive X-Ray Spectroscopy (EDS)

Energy-dispersive X-ray spectroscopy (EDS or EDX) is a surface analytical technique that identifies and maps or quantifies the elements (elemental composition) present in any given material [103], [104]. This method relies on the ionization of atoms in a sample by an electron beam which excites an electron in an inner shell, causing its ejection and the formation of an electron-hole in the electronic structure of the element [103], [104]. Subsequently, this void can be filled by an electron from a higher energy shell and the difference of energy between these two shells is expelled as x-rays [103], [104]. Therefore, the amount of energy of the emitted x-rays is specific for each element and its detection provides important information on the presence of specific elements on a sample, using an adequate energy-dispersive detector [103], [104]. Generally, elements present in concentrations higher than 1% by mass are usually detectable and EDS is commonly combined with scanning electron microscopy (SEM) since its modules are coupled within electron microscopes.

EDS analysis (INCAx-Act, PentaFET Precision, Oxford Instruments, UK) incorporated in scanning electron microscope (JSM-6010 LV, JEOL, Japan) was performed on the samples to estimate the Ca/P molar ratio of the Hap formed on the surface of CNCs. For this purpose, 0.01 and 0.001% (v/v) CNCs and m-CNCs dilutions were prepared from the stock solutions and sonicated (5 min, 60%; VCX750, Sonics & Materials Inc, USA) to disperse the nanoparticles. Then, a drop of each solution was placed on top of aluminium stubs fitted with conductive adhesive carbon tape (Media Lab System S.r.l., Italy) and tissue coverslips (polyethylene terephthalate, glycol-modified (PET-G); Sarstedt, Germany) cut at half, and allowed to dry until the procedure was performed. After drying, the samples were transferred into the EDS chamber and imaged at RT with an incident electron beam accelerated to 10 kV. After this, the Ca/P molar ratios were calculated for each sample.

2.2.3.1.5 Thermogravimetric analysis (TGA)

Thermogravimetric analysis (TGA) is a low-cost but destructive analytical method that monitors materials weight change as a function of temperature/time in a controlled environment [105]–[107]. This technique is widely used to study physical phenomena of materials as mass

variations, thermal stability, oxidation/reduction behaviour, decomposition, corrosion studies, water content, compositional analysis, and fraction of volatile components [105]–[107].

TGA comprises a furnace, a microbalance, a temperature controller, and a data acquisition system [105]–[107]. The materials' weight is measured on the microbalance while subject to a crescent or decreasing temperature at a constant rate or an isothermal temperature in the furnace, according to the desired method, and the values are recorded through time [105]–[107]. Moreover, the measurement is usually carried out in the presence of an oxygen-rich or free atmosphere, simulating or not the air atmosphere.

Within this work, a nitrogen (N_2) and a nitrogen/oxygen (N_2O_2; 79% to 21%) atmospheres were used to determine CNCs and m-CNCs water content and degradation temperature, and amount (%) of Hap, respectively, using a simultaneous thermal analyser (STA7200, Hitachi, Japan). In this sense, samples were freeze-dried and further weighted and transferred into a platinum pan and heated according to the desired purpose. For the determination of the water content and degradation temperature, samples were heated from 40°C to 105°C and then from 105°C to 600°C both at a 10°C/min heating rate for 15 min, under a N_2 atmosphere. Whereas, for the determination of the percentage of Hap, they were heated from 40°C to 600°C at 10°C/min heating rate for 15 min, after a 2-min isothermal period at 40°C under a N_2O_2 atmosphere.

2.2.3.2 Morphological characterization

2.2.3.2.1 High-Resolution Scanning Electron microscopy (SEM)

High-Resolution scanning electron microscopy (SEM) is a versatile surface-imaging technique, which produces high-resolution and high-magnification images of samples surface. For this purpose, a focused electron beam generated under high vacuum and accelerated through high voltage scans the specimens surface causing the emission of characteristic X-rays, elastically backscattered (or primary) electrons, secondary inelastic electrons, and Auger electrons from the atoms on the surface of the sample [102], [108]. This emission of electrons is detected by specific detectors and then displayed in a visual mode. Backscattered and secondary electrons are the most valuable in SEM to study the topography, morphology, and the atomic composition of the scanned specimen surface [102], [108]. Moreover, in SEM, the samples surface must be electrically conductive and grounded to prevent the accumulation of electrostatic charge, as this results in electrostatically distorted images and artefacts. To prevent this issue, the surface of

nonconductive samples should be coated with an ultrathin layer of an electrically conducting material, such as gold (Au), gold/palladium (Au/Pd) alloys, or platinum (Pt) [102].

Regarding this work, SEM analysis was performed to confirm if the decoration of CNCs with Hap was successful and to study Hap morphology, using a high-resolution field emission scanning electron microscope (Auriga Compact, Zeiss, Germany), which compared to conventional SEM produces clearer and less electrostatically distorted images. For this, CNCs and m-CNCs dilutions (0.01 and 0.001% v/v) were prepared from the stock solutions and sonicated (5 min, 60%; VCX750, Sonics & Materials Inc, USA) to disperse the nanoparticles. Then, a drop of each solution was placed on top of aluminium stubs fitted with conductive adhesive carbon tape (Media Lab System S.r.l., Italy) and circular coverglasses (13 mm Ø; 0.16-0.19 mm thickness; optical quality borosilicate; Agar Scientific Ltd, UK) cut at half, and allowed to dry until the procedure was performed. After drying, the samples were then transferred into the SEM chamber and imaged at RT with an incident electron beam accelerated to 3 kV.

2.2.4 Development of the cryogels

PL-based cryogels incorporating CNCs modified with aldehyde groups, and/or coated with Hap, were produced by cryogelation, following the procedure developed by Mendes *et al.* [78].

Towards this, the PL-m-CNCs cryogels were prepared by blending PL with a mixture of aCNCs and m-CNCs, at 1:1 volume ratio, using a double-barrel syringe, fitted with a static mixer placed at the outlet (Medmix, Germany) to homogenously extrude the cryogel precursors solutions into square molds (12 well silicone chamber, Ibidi, Germany). For PL-CNCs cryogels without m-CNCs, barrel A was filled with PL and barrel B with a-CNCs dispersion at 2.4 wt % concentration. Whereas, for PL-m-CNCs cryogels, barrel A was also filled with PL and barrel B with aCNCs (1.8–2.4 wt %) and m-CNCs dispersions (0.6–2.4 wt %). Before extrusion, the viscous aCNCs suspensions with or without M-CNCs nanoparticles were dispersed with an ultrasonic processor (30 s, 3 cycles, 60% amplitude; VCX750, Sonics & Materials Inc, USA) and sterilized under UV for 30 min. After extrusion into the molds, the cryogel precursors were frozen at -80°C on top of styrofoam and subsequently freeze-dried until full cryogelation. Figure II.6 depicts the working principle of the system developed in chapter III.

The final cryogel formulations were named according to the m-CNCs nanoparticles used and their concentrations: 0 wt % (Control), 0.6 wt % m-CNCs 6.9/20 (Amorphous-Low or A-Low), 2.4 wt % m-CNCs 6.9/20 (Amorphous-High or A-High), 0.6 wt % m-CNCs 7.9/20 (Crystalline-Low

or C-Low), and 2.4 wt % m-CNCs 7.9/20 (Crystalline-High or C-High). Table II.1 summarizes the different conditions used to develop the cryogels, as well the abbreviations that will be used to refer the different formulations.

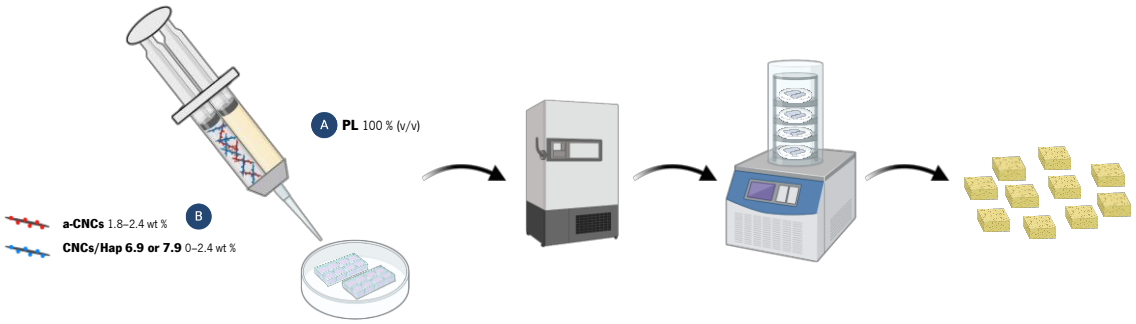

Figure II.6: Schematic representation of cryogelation process to obtain the different formulations of the PL-m-CNCs cryogels.

Table II.1: List of the developed formulations of the PL-m-CNCs cryogels studied within this thesis. Amorphous or crystalline nomenclature was adopted after XRD analysis.

Formulation	Concentration of PL (% v/v)	Concentration of a-CNCs (% v/v; wt %)	Concentration of m-CNCs (% v/v; wt %)
Control	50	(50%; 2.4)	(0%; 0)
		m-CNCs 6.9/20	
A-Low	50	(37.5%; 1.8)	(12.5%; 0.6)
A-High		(25%; 2.4)	(25%; 2.4)
		m-CNCs 7.9/20	
C-Low	50	(37.5%; 1.8)	(12.5%; 0.6)
C-High		(25%; 2.4)	(25%; 2.4)

2.2.5 Physical characterization of cryogels

The developed cryogels were analyzed in terms of microstructure, water uptake and degradation profiles, and mechanical properties.

2.2.5.1 Microstructure

Micro-computed tomography (micro-CT) uses X-rays for non-destructive 3D analysis of the bulk structure of scaffolds and tissue samples. The output is the general structure as a 3D model with micrometre resolution, more importantly, the subsequent analysis can yield information in

relation to pore size, pore distribution and pore interconnectivity in 3D, as well as pore wall thickness, material distribution, and the differentiation in between crystalline and hard materials inside samples.

In this work, PL-M-CNCs cryogels formulations (7 × 7 × 5 mm, n = 5) were scanned using an X-ray scan micrograph (micro-CT; SkyScan 1272; Bruecker, Kontich, Belgium). Series of two-dimensional projections, with a resolution of 10 μm were acquired over a rotation range of 180°, at a rotation step of 0.45°, by cone-beam acquisition. The data was reconstructed using the software NRecon (Version: 1.6.6.0, Skyscan), and analyzed on CT analyzer (Version: 1.17.0.0, Skyscan). The region of interest (ROI) was defined as a 6 x 6 mm square centred over the specimen. By auto-interpolation the manually defined ROI was yielded a representative 6 mm thick cobblestone-shaped volume of interest (VOI), which was the essential basis for the quantitative analyses. For the 3D morphological analysis, the Batman tool of CT analyzer software was used. The object was automatically defined (Ridler-Calvard method) to produce binarized projections, and the total porosity (Po.V (tot); vol. %), structure thickness (Tb.Th; μm), and pore size (Tb.Sp; μm) were calculated. The interconnectivity (InterConn) of the pores present in each sample was calculated according to equation II.5.

$$\mathbf{InterConn} = \mathbf{1} - \frac{\mathbf{TV.2px - Obj.V.2px}}{\mathbf{TV - Obj.V}} \qquad \textbf{(Equation II.5)}$$

In Equation II.5, TV.2px is the total VOI volume; Obj.V.2px is the object volume after shrink over holes with a diameter of 4 voxels (40 μm^2), defined as the lower dimensions for an interconnective pore; TV is the total VOI volume, and Obj.V is the object volume. The 3D reconstructions were produced using the CTVOX software.

2.2.5.2 Water uptake and degradation profiles

The stability and degradability of cryogels in vivo is dependent on several physicochemical and biological factors that include hydrolysis and degradation with specific enzymes, phagocytosis, and dissolution/erosion. Given that, the water uptake and degradation behaviour of the cryogels was tested in simulated physiological conditions to conclude about their biodegradability and stability, according to their m-CNCs content.

For determining the water uptake behaviour of the developed cryogels, the samples were initially weighed (Wi) and subsequently immersed, for 30 s, in 1 mL phosphate buffered saline

(PBS, Sigma-Aldrich, USA). The samples were immediately weighed (Wf) and the water uptake (mg/mg sample) was calculated using Equation II.6. All experiments were performed in triplicate.

$$\mathbf{Water\ Uptake} = \frac{\mathbf{W_f - W_i}}{\mathbf{W_i}} \qquad \textbf{(Equation II.6)}$$

Regarding the degradation properties, the weight loss of the cryogels over time was also analysed. For that, the specimens were incubated in 1 mL of PBS at 37°C for 2 h. After removing the excess PBS, the initial mass of the cryogel was measured (Wi) and successively weighed at different pre-selected time points (Wf) to determine the weight loss (%), according to equation II.7. The results are expressed as an average of three samples.

$$\text{Weight loss } (\%) = \frac{\mathbf{W_i}\text{-}W_f}{\mathbf{W_i}} \times 100\% \qquad \textbf{(Equation II.7)}$$

2.2.5.3 Evaluation of the mechanical properties

For bone TERM, it is very important to ensure that the implant has compatible mechanical properties compatible to the bone tissue. The uniaxial compressive test provides a simple, effective, and inexpensive way to characterize the developed cryogels behaviour and response while it experiences a compressive load. In this type of mechanical test, the sample is placed on the lower plate and compressed by moving the upper plate by a hydraulic piston. The specimen is strained at a constant speed and the applied load is shown as the load supported by the specimen over time.

For this, the specimen is subjected to a controlled compression and, by analysing the changes in length and resulting load, it is possible to calculate a stress-strain profile and assess some properties, such as the Young's modulus (E) or the compressive stress. The compressive stress (σ) is calculated by relating the applied force, P, expressed in Newtons (N), measured by the load cell, and the initial surface cross-sectional area perpendicular to the applied force (before load application), A, in m^2, as shown in equation II.8 [111].

$$\boldsymbol{\sigma} = \frac{\mathbf{P}}{\mathbf{A}} \left(\mathbf{N.\,m^{-2}\ or\ Pa}\right) \qquad \textbf{(Equation II.8)}$$

The dimensions of each sample were also measured and the compressive strain (ε) was calculated using equation II.9, where ΔL stands for the elongation that corresponds to the difference between the initial length (L_0; before any load applied) and the final length - L, both in millimeters (mm) [111].

$$\boldsymbol{\varepsilon} = \frac{\mathbf{\Delta L}}{\mathbf{L_0}} = \frac{\mathbf{L - L_0}}{\mathbf{L_0}}\ (\%) \qquad \textbf{(Equation II.9)}$$

Since this material has an initial elastic behaviour, stress and strain are linearly related in this region and, upon unloading, the deformation is elastically recoverable. The Elastic Modulus or Young's Modulus (E) corresponds to the slope of the stress-strain plot, within the linear elastic regime, and characterizes the stiffness of a material in units of force per unit area. It can be calculated by Hooke's Law, which relates the compressive stress and strain, as described by the equation II.10.

$$\mathbf{E} = \frac{\boldsymbol{\sigma}}{\boldsymbol{\varepsilon}} \ (\mathbf{Pa}) \qquad \textbf{(Equation II.10)}$$

At least three samples of each cryogel formulation were tested in a universal mechanical testing machine (Instron 5540, USA) equipped with a load cell of 50 N, under unidirectional compression. The hydrated (10 min in PBS) PL-m-CNCs cryogels (7 × 7 × 5 mm, n = 5) were set on the lower plate and compressed by moving the upper plate at a compression rate of 1 mm per min at RT. For cyclic tests, the samples were subjected to three successive loading and unloading cycles at a compression rate of 1 mm per min and ε = 50%. The obtained stress–strain curves were used to determine the Young's modulus (i.e., the average slope of the stress–strain curve in the initial linear region) to evaluate the structural integrity of the cryogels and their recovery capacity.

2.2.6 *In vitro* evaluation of the developed systems

Biological analysis of the designed systems was employed to study their performance *in vitro* when seeded with human adipose-derived stem cells (hASCs) and human dental pulp cells (hDPCs). Therefore, the effect of the Hap coating density and m-CNCs concentration in the potential modulation of bone regeneration of the cryogels was evaluated. For this, both cell types were seeded on the different samples and their behaviour in terms of viability, metabolic activity, proliferation, morphology, differentiation, and migration was evaluated.

2.2.6.1 Expansion of human Adipose tissue-derived Stem Cells (hASCs)

Adipose tissue-derived stem cells (ASCs) are mesenchymal stem cells (MSCs) obtained from adipose tissues, which are a rich source of multipotent stromal/stem cells that can differentiate along the adipogenic, chondrogenic, osteogenic, myogenic, neurogenic, endothelial, and other lineage pathways [112], [113]. ASCs high abundance in adipose tissue, lower collection morbidity [114]–[116], higher proliferation rate *in vitro* comparing to bone marrow derived stem cells (BMSCs) [117], [118], and comparable osteogenic potential [114]–[117], [119] have been supporting ASCs as a good alternative to BMSCs for bone TE. Despite displaying slightly lower

osteogenic potential compared with BMSCs, this potential is maintained during cells´ aging, unlike the rest of the MSCs [120]–[122]. Moreover, clinical studies conducted by Mesimäki et al. and Sandor et al. showed that ASCs hold great potential in oral and maxillofacial rehabilitation [123]–[125]. Therefore, hASCs were chosen for this work to be seeded onto PL-m-CNCs cryogels to address the regeneration of injured bone tissues.

Human adipose-derived stem cells (hASCs) were obtained from lipoaspirate samples of the abdominal region of healthy donors undergoing plastic surgery under the scope of an established protocol with Hospital da Prelada (Porto, Portugal) and with the approval of the Hospital Ethics Committee (approval number 005/2019). The hASCs isolation was performed using a previously optimized protocol [112]. hASCs were maintained in α-MEM (Sigma-Aldrich, USA) supplemented with 10% fetal bovine serum (FBS, Gibco, ThermoFisher Scientific, USA) and 1% antibiotic/antimycotic (A/A, Gibco, ThermoFisher Scientific, USA) and incubated at 37°C in a 5% CO_2 high-humidity environment, with medium replacements every 2 to 3 days. Cells until passage 5 were used for this study.

2.2.6.2 Expansion of human Dental Pulp Cells (hDPCs)

Human dental pulp cells (hDPCs) constitute an excellent mesenchymal stem cell source for dental tissue regeneration, owing to their high accessibility, motility, and multilineage differentiation potential [126]. Moreover, hDPCs have been able to regenerate dentin-pulp-like complexes with a similar ECM architecture as the natural tissue, exhibiting odontoblasts aligned with the dentinal wall to produce new dentin, and also to promote angiogenesis [127]. Therefore, hDPCs were chosen for this work to be seeded into PL cryogels laden with m-CNCs to address the regeneration of injured dental bone tissues.

hDPCs were isolated from human third molars, removed by orthodontic reasons, under a protocol established with the Malo Clinic (Porto, Portugal), as described by Almeida *et al.* [59]. Cells were expanded in 150 cm^2 culture flasks (TPP, Switzerland) and cultured with α-MEM (Sigma-Aldrich, USA) with 10% fetal bovine serum (FBS, Gibco, ThermoFisher Scientific, USA) and 1% antibiotic/antimycotic (A/A, Gibco, ThermoFisher Scientific, USA), as supplements. All cultures were incubated at 37°C in a 5% CO_2 high-humidity environment, with medium replacements every 2 to 3 days. Cells until passage 5 were used for this study.

2.2.6.3 Expansion of human umbilical vein cell line (EA.hy926)

Endothelial cells are intrinsic and essential to blood vessels structure and functionality, by surrounding the lumen and constituting the endothelium, the physical separation between the circulating blood and the surrounding tissues [128]. Moreover, they have an active role in maintaining vascular homeostasis by being involved in the processes of angiogenesis, that consists in their recruitment, proliferation, migration, organization and remodelling, thrombosis, blood pressure, and inflammation [129].

Human umbilical vein cell line (EA.hy926) was established by fusing primary human umbilical vein endothelial cells (HUVECs) with permanent human cell line A549 from carcinomic human alveolar basal epithelial cells [130], [131]. The resultant immortalized hybrid cell line retained many vascular endothelial properties of HUVECs such as expression of Von Willebrand factor, coagulation factor VIII (anti-hemophilic factor), tissue plasminogen activator, and thrombomodulin [130]–[132]. Furthermore, EA.hy926 cells grow faster in culture without any special requirement in terms of supplementation compared to HUVECs, and possess a unique marker that makes their identification easier. These cells are widely used as a model system for human vascular endothelial cells for the purification endothelial-specific factors, and identification and analysis of compounds that treat endothelial-mediated pathologies such as: high/low blood pressure, blood clotting, atherosclerosis, angiogenesis, and inflammation [130]–[132].

EA.hy926 were expanded and cultured using DMEM – low glucose (Sigma-Aldrich, USA) with 10% FBS (Gibco, ThermoFisher Scientific, USA) and 1% A/A (Gibco, ThermoFisher Scientific, USA). All cultures were incubated at 37°C in a 5% CO_2 high-humidity environment, with medium replacements every 2 to 3 days.

2.2.6.4 Cell seeding onto PL-m-CNCs cryogels

The ability of the cryogels to support cell adhesion and proliferation and to control cellular behaviours is crucial for successful TE applications. Thus, two different cell types were selected, and their behaviour was studied, when seeded on the developed cryogels, to address bone regeneration in **chapter III**.

For this, PL-m-CNCs cryogels were produced following the same procedure described in section 2.2.4, under sterile conditions. Afterwards, cultured cells, hASCs or hDPCs, were detached by trypsin, counted, and centrifuged at 300 xg for 5 min, at RT. The obtained cell pellets were resuspended in basal culture media (α-MEM) and 1×10^5 cells were seeded on the surface of

each sample, using 150 µL of cell suspension, and placed in 48-well plates. After 90 min of incubation at standard culture conditions to allow cell adhesion onto the cryogels, α-MEM with 10% FBS and 1% antibiotic/antimycotic was added to cover the samples. Then, the cryogel formulations were incubated at 37°C in a 5% CO_2 high-humidity environment for 1, 3, 7, 14, and 21 days, with medium replacement every 2 to 3 days. All formulations for each time point and assay were produced in quadruplicate.

2.2.6.5 Preliminary determination of cell viability by live/dead assay

Before the differentiation assays, there was a need to assess the biocompatibility of the developed cryogels. Therefore, cell viability was evaluated using a live/dead double cell staining using calcein AM and propidium iodide (PI). Calcein AM, is membrane-permeant and is hydrolysed by cells creating a negatively charged green, fluorescent calcein, that is retained in the cytoplasm, allowing to differentiate live cells. On the other hand, PI is not permeant to the membrane and therefore only stains cells in which that barrier has been breached, allowing to distinguish dead cells.

At the end of 4 days of culture, the cells were rinsed with PBS and incubated with Calcein AM (Invitrogen, USA) 1:500 v/v in PBS for 30 min at 37°C. Thereafter, samples were rinsed again with PBS and incubated in PI (Invitrogen, USA) 1:1000 v/v solution in PBS for 30 min at 37°C. Then, the cells were washed again with PBS to minimize background fluorescence. Processed samples were observed using a confocal microscope TCS SP8 (Leica Microsystems, Germany). Each experiment was performed in triplicate.

2.2.6.6 Evaluation of metabolic activity by Alamar Blue assay

Alamar Blue fluorescence assay is a rapid and sensitive method for quantitatively measure cell´s metabolic activity and cytotoxicity. This assay relies on the colorimetric properties of a blue, non-toxic, non-fluorescent reduction-oxidation indicator known as resazurin (7-hydroxy-10-oxidophenoxazin-10-ium-3-one) that is reduced into a highly fluorescent red coloured compound named resorufin, in response to chemical reduction reactions resulting from cells metabolic activity, specifically in the respiratory chain [133]. The resorufin concentration can be determined by fluorescence spectroscopy and the differences in its detection are proportional to the number of metabolic active cells. It also provides additional information on their overall viability. The experiment was performed according to the manufacturer´s recommendations.

Briefly, at each pre-selected time point, a 10% (v/v) Alamar Blue (Bio-Rad, UK) solution was prepared using culture medium and protected from light. Then, the culture medium was removed, and each sample was thoroughly washed with PBS. Afterwards, each sample was incubated in 500 µL of the 10% Alamar Blue solution for 3 h at 37°C in a standard 5% CO_2 humidified atmosphere, shielded from light exposure. After incubation, 100 µL of each sample supernatant were collected in triplicate and transferred to a 96-well plate. Background was also performed by incubating the Alamar Blue solution in the same conditions but in empty wells. Thereafter, the fluorescence was measured using a Synergy HT microplate reader (Bio-Tek Instruments, USA) at excitation and emission wavelengths of 570 and 600 nm, respectively. Background fluorescence was retracted from the fluorescence values of each sample.

2.2.6.7 Determination of cell proliferation by DNA quantification

Cell proliferation was determined by quantifying the total amount of double-stranded deoxyribonucleic acid (dsDNA) present at different culture times (1, 3, 7, 14, and 21 days) using a Quant-iT™ PicoGreen® dsDNA dsDNA Assay Kit (Molecular Probes, Invitrogen, USA), according to the manufacturer's instructions. Quant-iT™ PicoGreen® dsDNA reagent is an ultra-sensitive fluorescent nucleic acid stain for the quantification of dsDNA in a solution. After assessing the metabolic activity for each time-point, the cryogels were washed with PBS and then incubated with 1 mL of ultra-pure water for an h at 37°C in a standard 5% CO_2 humidified atmosphere. After this, the samples were frozen at -80°C until further use.

Upon testing, the samples were thawed at RT and then sonicated using an ultrasonic ice-cold water bath (DT 100 H Sonorex Digitec, Bandelin, Germany) for 15 min or an ultrasonic processor (VCX-130PB-220, Sonics, USA) for 3 cycles of 5 seconds, to fully lyse the cells and guarantee that all cell content was released. Meanwhile, a set of DNA standards were prepared in concentrations of 2, 1, 0.5, 0.25, 0.125, 0.0625, 0.03125, and 0 µg/mL, using the DNA standard (100 µg/mL) provided by the kit. Moreover, a 1x TE buffer solution was also prepared by dilution of the provided 20x TE reagent with ultra-pure water, with a volume necessary to the total amount of samples. The Quant-iT™ PicoGreen® dsDNA reagent was diluted 200-fold with the 1x TE, protecting it from light. Afterwards, 28.7 µL of standard or sample as well as 100 µL of 1x TE and 71.3 µL of the prepared PicoGreen solution were placed into each well of 96-well white opaque plates. The plate was incubated for 10 min in the dark at RT and the fluorescence was measured using a microplate reader (Synergy HT, BioTek Instruments, USA) at an excitation and emission

wavelengths of 485 and 528 nm, respectively. Four cryogels of each condition were analysed, and the fluorescence readings were performed in triplicate for each sample. The DNA concentration for each sample was calculated using a standard calibration curve relating the standards' concentration and the measured fluorescence intensity.

2.2.6.8 Alkaline phosphatase (ALP) quantification

Alkaline phosphatase (ALP) is a glycoprotein that plays an important role in bone tissue formation by hydrolysing naturally occurring inorganic phosphate-based mineralization inhibitors and releasing their phosphate for Hap synthesis. Therefore, ALP is the most used biochemical functional marker of osteoblastic bone formation [134]. ALP activity can be assessed using the p-nitrophenol (pnP) assay, where p-nitrophenyl phosphate (pNPP), a colourless phosphatase substrate, is hydrolysed by ALP into a yellow-coloured product, p-nitrophenol (pnP), which has its maximal absorbance at 405 nm. The reaction is then stopped by the addition of NaOH, and the absorbance read in the microplate.

In this work, the ALP activity was determined at different time points (7, 14, and 21 days), using the abovementioned assay. In short, cell lysis was induced as previously described (2.2.6.5). Further, all samples were centrifuged at 13500 rpm for 15 min using a microcentrifuge (ScanSpeed Mini, Labogene, Denmark) and the supernatant was used. Meanwhile, a set of ALP standards were prepared in concentrations of 200, 40, 13.3, 8, 1.6, 0.32, and 0 pmol/min, using a calf intestinal ALP enzyme (1 μmol/min; Promega, USA) and ALP buffer solution (1.5 M and pH 10.3; Sigma-Aldrich, Merck, USA), to obtain a standard curve. Afterwards, in each well of a 96-well plate, 80 μL of standard or sample were mixed with 20 μL ALP buffer solution and 100 μL of the phosphate substrate (pnPP, Sigma-Aldrich, Merck, USA). The plate was allowed to incubate for 1 h protected from light at 37°C. After the incubation period, 100 μL of a stop solution, 0.3 M NaOH (Panreac Quimica, Spain) was added to each well. Absorbance was measured using a microplate reader (Synergy HT, BioTek Instruments, USA) at 405 nm and the ALP concentrations were calculated using the obtained standard calibration curve, that relates the standards' concentration and the measured absorbance intensity. Four cryogels of each condition were analysed, and the absorbance readings were performed in duplicate for each sample.

2.2.6.9 Evaluation of gene expression through Polymerase Chain Reaction

Reverse Transcriptase Polymerase Chain Reaction (RT-PCR) is a technique extensively applied in molecular biology that combines the process of reverse transcription of ribonucleic acid

(RNA) into DNA and the amplification of DNA segments by PCR to study gene expression [135]. It consists of three steps: (1) the reverse transcriptase-based conversion of RNA into complementary DNA (cDNA); (2) the amplification of cDNA through PCR; and (3) the detection of the amplification product [135]. In order to monitor specific genes expression, a well-designed gene specific primer is necessary to accurately and successfully analyse its expression [135].

The process of RT-PCR starts with the isolation of intact and high-quality RNA. At the end of each time point, samples were thoroughly washed with PBS and collected into Eppendorf tubes. In each tube, 500 μL of TRIReagent (Sigma-Aldrich, Merck, USA) were added and all tubes were stored at -80°C until further use. Total RNA was isolated from cells using the TRIReagent, according to the manufacturer´s protocol. The total RNA concentration was quantified at 260 nm using the NanoDrop 1000 spectrophotometer (Thermo Fisher Scientific, USA). Afterwards, cDNA was synthesized using the same amount of isolated RNA (500 ng) and the qScript cDNA Synthesis Kit (Quanta Biosciences, USA) to reverse transcribe it, according to the supplier instructions. Aliquots of each cDNA sample were diluted and frozen (-20°C) until the PCR reactions were carried out.

Real-time PCR was performed for two reference genes, glyceraldehyde-3-phosphate dehydrogenase (GAPDH) and β-Actin and target genes (Table II.2). Real-time PCR was performed in a mastercycler (Realplex, Eppendorf, Germany) using PerfeCTa SYBR Green FastMix (Quanta Biosciences, USA). Each reaction contained 7 μl of master mix (Perfecta SYBR Green FastMix, Quanta Biosciences, USA), the sense and the antisense specific primers (0.5 μM) and cDNA sample (3 μl) in a final volume of 10 μl. The amplification program consisted of a pre-incubation step for denaturation of the template cDNA (2 min, 95°C), followed by 40 cycles of denaturation (5 s, 95°C), an annealing step (15 s, 60°C) and an extension step (20 s, 72°C). After each cycle, fluorescence was measured at 72°C. A negative control without cDNA template was run in each assay. All samples were normalized by the geometric mean of the expression levels of reference genes β-Actin and GAPDH, and fold changes were related to the control groups using the ΔΔCt method, where Ct is the crossing point of the reaction amplification curves determined by the Realplex 2.2 software (Eppendorf, Germany).

Table II 2: Primer sequences for real time PCR. F: forward primer; R: reverse primer

Gene	Function	Sequence (5'-3')
β-Actin	Cytoskeletal protein involved in cell structure and motility	F: CTGGAACGGTGAAGGTGACA R: AAGGGACTTCCTGTAACAA
Glyceraldehyde-3-phosphate dehydrogenase (GAPDH)	Key enzyme in glycolysis that also modulates the organization and assembly of the cytoskeleton	F: GGGAGCCAAAAGGGTCATCA R: GCATGGACTGTGGTCATGAGT
Runt-related transcription factor 2 (RUNX2)	Transcription factor involved in osteoblastic differentiation (promotes stem cells differentiation to preosteoblasts and preosteoblasts into osteoblasts)	F: TTCCAGACCAGCAGCACTC R: CAGCGTCAACACCATCATTC
Alpha-1 type I collagen (COL1A1)	Related with the deposition of type I collagen, the main component of bone ECM	F: CCCCAGCCACAAAGAGTCTAC R: TTGGTGGGATGTCTTCGTCT
Alkaline Phosphatase (ALP)	Hydrolyses inhibitors of mineral deposition (pyrophosphates), increasing phosphate concentration and mineralization	F: GAAGGAAAAGCCAAGCAGGC R: GGGGGCCAGACCAAAGATAG
Osteocalcin (OC)	Late-stage marker for osteoblastic differentiation and may regulate the osteoclasts activity and process	F: CTCACACTCCTCGCCCTATTG R: GCTTGGACACAAAGGCTGCAC
Osteopontin (OPN)	Modulates the intrafibrillar nanoscale mineralization of collagen	F: GGGGACAACTGGAGTGAAAA R: CCCACAGACCCTTCCAAGTA
Bone Morphogenetic Protein-2 (BMP-2)	Important regulation factor in osteogenesis, inducing undifferentiated stem cells into bone tissue	F: TGAATCAGAATGCAAGCAGG R: TCTTTTGTGGAGAGGATGCC
Osterix (OSX)	Transcription factor essential for osteoblast differentiation and bone formation	F: CCCTTTACAAGCACTAATGG R: ACACTGGGCAGACAGTCAG
Osteoprotegerin (OPG)	Key cytokine receptor for RANKL to inhibit osteoclastogenesis (bone resorption)	F: CCTCCTGGATTTGGAGTGGT R: CTCACACAGGGTAACATCTATTCCA
Receptor Activator of NF-kβ Ligand (RANKL)	Crucial cytokine to promote osteoclastogenesis (involved in bone resorption)	F: CAGAGCGCAGATGGATCCTAA R: TCCTTTTGCACAGCTCCTTGA
Dickkopf-related Protein 1 (DKK-1)	Protein that antagonizes with osteogenesis by inhibiting the Wnt signaling pathway	F: TTGACAACTACCAGCCGTACC R: TTTGCAGTAATTCCCGGGGC

2.2.6.10 Immunocytochemistry

Immunocytochemistry (ICC) is a widely used technique for the detection and visualization of proteins or other antigens in cells using antibodies that specifically recognize the target of interest. The antibody is directly or indirectly linked to a reporter, such as a fluorophore or enzyme. The reporter gives rise to a signal, such as fluorescence or colour from an enzymatic reaction, which can be detected by confocal microscopy or other equipment.

For this purpose, the previously cultured cells on the scaffolds are subjected to immunostaining, which involves fixation, permeabilization, antibodies incubation, and posterior imaging [136]. Fixation retains the proteins at their location in the cell and preserves their chemical and structural state at the time of fixation. It can be done by crosslinking or by precipitating the proteins using organic solvents. Upon permeabilization, membranes are punctured using solvents or detergents, allowing the relatively large antibodies to cross the cellular membranes. The permeabilization requires fixation, and hence limits the technique to studying dead cells. During

antibody incubation, primary antibodies are allowed to bind to target antigens within or on the cells, and if required, the secondary antibodies bind to the primary. Thereafter, the antigen-antibody coloured, or fluorescent bounds are visualized by microscopy, producing images of the desired cellular structures.

In this work, we studied the effect of our scaffolds containing Hap on the phenotype of the differentiating stem cells. Thus, the osteogenic phenotype of the seeded hASCs onto the different cryogels developed was assessed by immunodetection of bone-specific proteins. Osteopontin (OPN) is one the most abundant non-collagenous proteins in bone. It binds to several ECM molecules, including type I collagen, fibronectin, and osteocalcin (OC), and even cells, and may add physical strength to the ECM. Moreover, it is involved in the modulation of the intrafibrillar nanoscale mineralization of collagen [137].

Furthermore, the morphology of cells can also be evaluated by staining specific cellular structures as the nucleus or the actin filaments of cytoskeleton with fluorescent cell markers, such as 4,6-diamidino-2-phenyindole dilactate (DAPI) or Phalloidin (Phalloidin–Tetramethylrhodamine B isothiocyanate), respectively. DAPI is a blue coloured nucleus marker that binds with the nucleus dsDNA creating fluorescent complexes, and the Phalloidin is a red coloured cytoskeleton marker, that stains actin filaments.

For this, at the end of the last time point (21 days), the samples were fixed in 100% Methanol (Honeywell, USA) for 10-20 min at 4°C, washed thoroughly with PBS, and kept at 4°C in PBS until further use. Cells were permeabilised with 0.1% (v/v) Triton X-100 for 20 min, at RT under gentle agitation. Then samples were rinsed with PBS and blocked with 2% (w/v) bovine serum albumin (BSA) in PBS for 1h, at RT. Thereafter, cryogels were incubated with a primary antibody against osteopontin (OPN) (rabbit anti-OPN antibody, 1:1000, Abcam ab8448) in 0.1% (w/v) BSA in PBS, overnight at 4 °C under gentle agitation. After removing the antibody solution, all sample were washed 3 times with PBS for 15 min. Thereafter, the samples were incubated with the corresponding secondary antibody labelled with AlexaFluor 488 (donkey anti-rabbit IgG (H+L), A21206, Invitrogen, 1:200), for 2 h at RT protected from light under mild agitation. Finally, once the samples were washed with PBS, nuclei, and cytoskeleton were stained with DAPI (1:1000 in PBS) and phalloidin-TRITC (1:200 in PBS), respectively, at RT for 1 h. After a final washing, the samples were kept in PBS at 4 °C until the imaging. The cryogels were visualized using a confocal

laser scanning microscope TCS SP8 (Leica Microsystems, Germany). Each experiment was performed in duplicate.

2.2.6.11 Immunohistochemistry

Immunohistochemistry (IHC) is a powerful technique for visualizing cellular components, as proteins or other macromolecules in tissue samples. The strength of IHC is the intuitive visual output that reveals the existence and localization of the target-protein in the context of different cell types, biological states, and/or subcellular localization within complex tissues. In this work, three different histological stains were used to evaluate the osteogenic differentiation and the biomineralization. For that, hematoxylin and eosin (H&E), Masson´s Trichrome, and Alizarin Red were used. H&E is the most widely used stain in histology and allows localization of nuclei and extracellular proteins [138]. It contains hematoxylin, not a dye itself, which produces the blue hematin via an oxidation reaction with nuclear histones causing nuclei to show blue [138]. Eosin is employed as a counterstain to stain tissues with a red (acetic cytoplasm) blue, pink (collagen or muscle) or purplish (basic cytoplasm) colour [138]. Furthermore, Masson's trichrome is a three-color stain designed to distinguish cells and connective tissue [138]. For most applications, connective tissue (collagen) is stained blue, nuclei stain deep red, and cytoplasm is a lighter red or pink [138]. Alizarin red is used for the staining of cartilage and bone. It reacts with calcium, thereby helping in the diagnosis of calcium deposits.

In this sense, after 21 days of culture, PL-m-CNCs cryogels were washed with PBS and then fixed in 10% formalin (Thermo Fisher Scientific, USA) for 30 min at RT. The samples were embedded in Histogel specimen processing gel (Thermo Fisher Scientific, USA), dehydrated through graded ethanol solutions, and embedded in paraffin for further sectioning using a microtome (HM355S, Microm, Thermo Scientific). Sections of 10 μm thickness were prepared and stained with H&E, Masson´s Trichrome, and alizarin red. Sections were observed under a transmitted light Microscope (Zeiss, Germany).

2.2.6.12 Proangiogenic properties of the PL-M-CNCs cryogels

Bone complex vasculature arrangement not only maintains the vitality of tissue, but also plays a major role in bone physiology, by providing a sufficient amount of nutrients, including oxygen, the removal of metabolic waste products, and assure the immune response against microbial invasion [139]–[143]. Vascularization takes an important role in achieving an optimal microenvironment that supports angiogenesis, cell-cell crosstalk, cell migration, and differentiation

[142], [143]. Therefore, securing a good blood supply, from the formation of a capillary network, is a critical and long-standing challenge for the survival and success of bone TE constructs [142], [143]. To achieve a vascular network, the scaffold should possess an adequate porosity for the penetration and ingrowth of capillaries [142], [143]. Besides porosity, angiogenesis may be accomplished by the incorporation of GFs or hemoderivatives in the scaffolds or by co-culturing progenitor/target cells with endothelial cells [142].

In this work, the cryogels ability to promote vascular regeneration was assessed by seeding EA.hy926 cells an hASCs onto the PL-m-CNCs cryogels, in 4:1 ratio. For this, PL-m-CNCs cryogels were produce following the same procedure described in section 2.2.4, under sterile conditions, within a week in advance. Afterwards, cultured cells, EA.hy926 and hASCs, were detached by trypsin, counted, and centrifuged at 300 xg for 5 min, at RT. The obtained cell pellets were resuspended in basal culture media in 4:1 (EA.hy926:hASCs) ratio (α-MEM) and 1×10^5 cells were seeded on the surface of each sample, using 200 µL of cell suspension, and placed in 48-well plates. After 90 min of incubation at standard culture conditions to allow cell adhesion onto the cryogels, α-MEM with 10% FBS and 1% antibiotic/antimycotic was added to cover the samples. Then, the cryogel formulations were incubated at 37ºC in a 5% CO_2 high-humidity environment for 7 days, with medium replacement every 2 to 3 days. All formulations were produced in quadruplicate.

To evaluate the vascularization, cryogels were immunostained using specific vascular markers, such as such as cluster of differentiation 31 (CD31), also known as platelet endothelial cell adhesion molecule (PECAM-1). For that, samples were fixed and permeabilized, as previously described. Then, samples were incubated with the primary antibody CD31-APC conjugated (FAB3567A, R&D Systems, USA). Afterwards, nuclei and cytoskeleton were stained using DAPI and Phalloidin, as previously described. The samples were visualized using confocal laser scanning microscope.

2.3 Statistical Analysis

Statistical analysis was performed to determine if significant differences were observed among the studied parameters. Different tests were used depending on the number of test groups and the sample size. The statistical analysis was conducted with the software GraphPad Prism version 9.0 (GraphPad Software Inc., San Diego, CA, USA) using one-way analyses of variance (ANOVA) followed by Tukey post hoc test, or a two-way ANOVA with Bonferroni post-test, to study

the influence of two categorical independent variables. The values were considered different for a level of significance of $p<0.05$ (minimum of 95% confidence interval). Statistically significant values are annotated in their respective graphs and the data is represented by mean ± standard error.

2.4 References

[1] M. A. S. Azizi Samir, F. Alloin, and A. Dufresne, "Review of recent research into cellulosic whiskers, their properties and their application in nanocomposite field," *Biomacromolecules*, vol. 6, no. 2, pp. 612–626, 2005, doi: 10.1021/bm0493685.

[2] M. Börjesson and G. Westman, "Crystalline Nanocellulose — Preparation, Modification, and Properties," *Cellul. - Fundam. Asp. Curr. Trends*, 2015, doi: 10.5772/61899.

[3] J. George and S. N. Sabapathi, "Cellulose nanocrystals: Synthesis, functional properties, and applications," *Nanotechnol. Sci. Appl.*, vol. 8, pp. 45–54, 2015, doi: 10.2147/NSA.S64386.

[4] Y. Habibi, L. A. Lucia, and O. J. Rojas, "Cellulose nanocrystals: Chemistry, self-assembly, and applications," *Chem. Rev.*, vol. 110, no. 6, pp. 3479–3500, 2010, doi: 10.1021/cr900339w.

[5] R. J. Moon, A. Martini, J. Nairn, J. Simonsen, and J. Youngblood, *Cellulose nanomaterials review: Structure, properties and nanocomposites*, vol. 40, no. 7. 2011.

[6] R. M. A. Domingues, M. E. Gomes, and R. L. Reis, "The potential of cellulose nanocrystals in tissue engineering strategies," *Biomacromolecules*, vol. 15, no. 7, pp. 2327–2346, 2014, doi: 10.1021/bm500524s.

[7] D. Bondeson, A. Mathew, and K. Oksman, "Optimization of the isolation of nanocrystals from microcrystalline cellulose by acid hydrolysis," *Cellulose*, vol. 13, no. 2, pp. 171–180, 2006, doi: 10.1007/s10570-006-9061-4.

[8] S. Eyley and W. Thielemans, "Surface modification of cellulose nanocrystals," *Nanoscale*, vol. 6, no. 14, pp. 7764–7779, 2014, doi: 10.1039/c4nr01756k.

[9] R. H. Marchessault, F. F. Morehead, and M. J. Koch, "Some Hydrodynamic Properties of Neutral As Related To Size and Shape 1," *J. Colloid Sci.*, vol. 344, pp. 327–344, 1961.

[10] R. M. A. Domingues *et al.*, "Development of Injectable Hyaluronic Acid/Cellulose Nanocrystals Bionanocomposite Hydrogels for Tissue Engineering Applications," *Bioconjug. Chem.*, vol. 26, no. 8, pp. 1571–1581, 2015, doi: 10.1021/acs.bioconjchem.5b00209.

[11] S. Beck-Candanedo, M. Roman, and D. G. Gray, "Effect of reaction conditions on the properties and behavior of wood cellulose nanocrystal suspensions," *Biomacromolecules*, vol. 6, no. 2, pp. 1048–1054, 2005, doi: 10.1021/bm049300p.

[12] S. Elazzouzi-Hafraoui, Y. Nishiyama, J. L. Putaux, L. Heux, F. Dubreuil, and C. Rochas, "The shape and size distribution of crystalline nanoparticles prepared by acid hydrolysis of native cellulose," *Biomacromolecules*, vol. 9, no. 1, pp. 57–65, 2008, doi: 10.1021/bm700769p.

[13] R. Dash, M. Foston, and A. J. Ragauskas, "Improving the mechanical and thermal properties of gelatin hydrogels cross-linked by cellulose nanowhiskers," *Carbohydr. Polym.*,

vol. 91, no. 2, pp. 638–645, 2013, doi: 10.1016/j.carbpol.2012.08.080.

[14] J. Han, T. Lei, and Q. Wu, "High-water-content mouldable polyvinyl alcohol-borax hydrogels reinforced by well-dispersed cellulose nanoparticles: Dynamic rheological properties and hydrogel formation mechanism," *Carbohydr. Polym.*, vol. 102, no. 1, pp. 306–316, 2014, doi: 10.1016/j.carbpol.2013.11.045.

[15] T. Abitbol, T. Johnstone, T. M. Quinn, and D. G. Gray, "Reinforcement with cellulose nanocrystals of poly(vinyl alcohol) hydrogels prepared by cyclic freezing and thawing," *Soft Matter*, vol. 7, no. 6, pp. 2373–2379, Mar. 2011, doi: 10.1039/c0sm01172j.

[16] X. Zhang *et al.*, "Structure and properties of polysaccharide nanocrystal-doped supramolecular hydrogels based on Cyclodextrin inclusion," *Polymer (Guildf).*, vol. 51, no. 19, pp. 4398–4407, 2010, doi: 10.1016/j.polymer.2010.07.025.

[17] Y. Habibi and A. Dufresne, "Highly filled bionanocomposites from functionalized polysaccharide nanocrystals," *Biomacromolecules*, vol. 9, no. 7, pp. 1974–1980, Jul. 2008, doi: 10.1021/bm8001717.

[18] Y. Habibi, A. L. Goffin, N. Schiltz, E. Duquesne, P. Dubois, and A. Dufresne, "Bionanocomposites based on poly(ε-caprolactone)-grafted cellulose nanocrystals by ring-opening polymerization," *J. Mater. Chem.*, vol. 18, no. 41, pp. 5002–5010, 2008, doi: 10.1039/b809212e.

[19] A. Junior de Menezes, G. Siqueira, A. A. S. Curvelo, and A. Dufresne, "Extrusion and characterization of functionalized cellulose whiskers reinforced polyethylene nanocomposites," *Polymer (Guildf).*, vol. 50, no. 19, pp. 4552–4563, Sep. 2009, doi: 10.1016/j.polymer.2009.07.038.

[20] J. Yang, C. R. Han, J. F. Duan, F. Xu, and R. C. Sun, "Mechanical and viscoelastic properties of cellulose nanocrystals reinforced poly(ethylene glycol) nanocomposite hydrogels," *ACS Appl. Mater. Interfaces*, vol. 5, no. 8, pp. 3199–3207, Apr. 2013, doi: 10.1021/am4001997.

[21] R. Cha, Z. He, and Y. Ni, "Preparation and characterization of thermal/pH-sensitive hydrogel from carboxylated nanocrystalline cellulose," *Carbohydr. Polym.*, vol. 88, no. 2, pp. 713–718, Apr. 2012, doi: 10.1016/j.carbpol.2012.01.026.

[22] Q. Dai and J. F. Kadla, "Effect of nanofillers on carboxymethyl cellulose/hydroxyethyl cellulose hydrogels," *J. Appl. Polym. Sci.*, vol. 114, no. 3, pp. 1664–1669, Nov. 2009, doi: 10.1002/app.30789.

[23] R. M. A. Domingues, S. Chiera, P. Gershovich, A. Motta, R. L. Reis, and M. E. Gomes, "Enhancing the Biomechanical Performance of Anisotropic Nanofibrous Scaffolds in Tendon Tissue Engineering: Reinforcement with Cellulose Nanocrystals," *Adv. Healthc. Mater.*, vol. 5, no. 11, pp. 1364–1375, Jun. 2016, doi: 10.1002/adhm.201501048.

[24] R. R. Lahiji, X. Xu, R. Reifenberger, A. Raman, A. Rudie, and R. J. Moon, "Atomic force microscopy characterization of cellulose nanocrystals," *Langmuir*, vol. 26, no. 6, pp. 4480–4488, 2010, doi: 10.1021/la903111j.

[25] X. Yang, E. Bakaic, T. Hoare, and E. D. Cranston, "Injectable polysaccharide hydrogels reinforced with cellulose nanocrystals: Morphology, rheology, degradation, and

cytotoxicity," *Biomacromolecules*, vol. 14, no. 12, pp. 4447–4455, 2013, doi: 10.1021/bm401364z.

[26] C. Zhou, Q. Wu, and Q. Zhang, "Dynamic rheology studies of in situ polymerization process of polyacrylamide-cellulose nanocrystal composite hydrogels," *Colloid Polym. Sci.*, vol. 289, no. 3, pp. 247–255, Feb. 2011, doi: 10.1007/s00396-010-2342-3.

[27] C. R. Silva *et al.*, "Injectable and tunable hyaluronic acid hydrogels releasing chemotactic and angiogenic growth factors for endodontic regeneration," *Acta Biomater.*, vol. 77, pp. 155–171, 2018, doi: 10.1016/j.actbio.2018.07.035.

[28] B. B. Mendes, M. Gómez-Florit, R. A. Pires, R. M. A. Domingues, R. L. Reis, and M. E. Gomes, "Human-based fibrillar nanocomposite hydrogels as bioinstructive matrices to tune stem cell behavior," *Nanoscale*, vol. 10, no. 36, pp. 17388–17401, Sep. 2018, doi: 10.1039/c8nr04273j.

[29] E. M. Rivera-muñoz and E. M., "Hydroxyapatite-Based Materials : Synthesis and Characterization," *Biomed. Eng. - Front. Challenges*, Aug. 2000, doi: 10.5772/19123.

[30] E. Andronescu *et al.*, "Nano-hydroxyapatite: Novel approaches in biomedical applications," *Nanobiomaterials Hard Tissue Eng. Appl. Nanobiomaterials*, pp. 189–213, Feb. 2016, doi: 10.1016/B978-0-323-42862-0.00006-7.

[31] R. Z. Legeros and J. P. Legeros, "Hydroxyapatite," *Bioceram. their Clin. Appl.*, pp. 367–394, 2008, doi: 10.1533/9781845694227.2.367.

[32] K. Lin and J. Chang, "Structure and properties of hydroxyapatite for biomedical applications," *Hydroxyapatite Biomed. Appl.*, vol. 4214, no. 8, pp. 3–19, 2015, doi: 10.1016/b978-1-78242-033-0.00001-8.

[33] J. A. Rincón-López, J. A. Hermann-Muñoz, A. L. Giraldo-Betancur, A. De Vizcaya-Ruiz, J. M. Alvarado-Orozco, and J. Muñoz-Saldaña, "Synthetic and Bovine-Derived Hydroxyapatite Ceramics : A Comparison," *Materials (Basel).*, vol. 11, no. 333, p. 17, 2018, doi: 10.3390/ma11020333.

[34] M. Markovic, B. O. Fowler, and M. S. Tung, "Preparation and comprehensive characterization of a calcium hydroxyapatite reference material," *J. Res. Natl. Inst. Stand. Technol.*, vol. 109, no. 6, pp. 553–568, 2004, doi: 10.6028/jres.109.042.

[35] J. Gómez-Morales, M. Iafisco, J. M. Delgado-López, S. Sarda, and C. Drouet, "Progress on the preparation of nanocrystalline apatites and surface characterization: Overview of fundamental and applied aspects," *Progress in Crystal Growth and Characterization of Materials*, vol. 59, no. 1. Pergamon, pp. 1–46, Mar. 01, 2013, doi: 10.1016/j.pcrysgrow.2012.11.001.

[36] J. C. Elliott, R. M. Wilson, and S. E. P. Dowker, "Apatite structures," *Adv. X-ray Anal.*, vol. 45, pp. 172–181, 2002.

[37] C. Huang *et al.*, "Porous artificial bone scaffold synthesized from a facile in situ hydroxyapatite coating and crosslinking reaction of crystalline nanocellulose," *Materialia*, vol. 4, pp. 237–246, Dec. 2018, doi: 10.1016/j.mtla.2018.09.008.

[38] M. Sadat-Shojai, M. T. Khorasani, E. Dinpanah-Khoshdargi, and A. Jamshidi, "Synthesis methods for nanosized hydroxyapatite with diverse structures," *Acta Biomaterialia*, vol. 9,

no. 8. Elsevier Ltd, pp. 7591–7621, Aug. 01, 2013, doi: 10.1016/j.actbio.2013.04.012.

[39] N. A. S. Mohd Pu'ad, R. H. Abdul Haq, H. Mohd Noh, H. Z. Abdullah, M. I. Idris, and T. C. Lee, "Synthesis method of hydroxyapatite: A review," in *Materials Today: Proceedings*, Jan. 2019, vol. 29, pp. 233–239, doi: 10.1016/j.matpr.2020.05.536.

[40] M. H. Fathi, A. Hanifi, and V. Mortazavi, "Preparation and bioactivity evaluation of bone-like hydroxyapatite nanopowder," *J. Mater. Process. Technol.*, vol. 202, no. 1–3, pp. 536–542, 2008, doi: 10.1016/j.jmatprotec.2007.10.004.

[41] M. Ishikawa, "Synthesis of Hydroxyapatite/Nanocellulose Composites," Kungliga Tekniska Högskolan, 2014.

[42] L. Chen, J. M. Mccrate, J. C. M. Lee, and H. Li, "The role of surface charge on the uptake and biocompatibility of hydroxyapatite nanoparticles with osteoblast cells," *Nanotechnology*, vol. 22, no. 10, p. 105708, Mar. 2011, doi: 10.1088/0957-4484/22/10/105708.

[43] M. Ishikawa, Y. Oaki, Y. Tanaka, H. Kakisawa, G. Salazar-Alvarez, and H. Imai, "Fabrication of nanocellulose-hydroxyapatite composites and their application as water-resistant transparent coatings," *J. Mater. Chem. B*, vol. 3, no. 28, pp. 5858–5863, 2015, doi: 10.1039/c5tb00927h.

[44] C. Huang *et al.*, "Biomimetic composite scaffold from an in situ hydroxyapatite coating on cellulose nanocrystals," *RSC Adv.*, vol. 9, no. 10, pp. 5786–5793, Feb. 2019, doi: 10.1039/c8ra09523j.

[45] D. Z. Chen *et al.*, "Dynamic mechanical properties and in vitro bioactivity of PHBHV/HA nanocomposite," *Compos. Sci. Technol.*, vol. 67, no. 7–8, pp. 1617–1626, Jun. 2007, doi: 10.1016/j.compscitech.2006.07.034.

[46] I. M. Pelin, S. S. Maier, G. C. Chitanu, and V. Bulacovschi, "Preparation and characterization of a hydroxyapatite-collagen composite as component for injectable bone substitute," *Mater. Sci. Eng. C*, vol. 29, no. 7, pp. 2188–2194, Aug. 2009, doi: 10.1016/j.msec.2009.04.021.

[47] P. Habibovic *et al.*, "Comparative in vivo study of six hydroxyapatite-based bone graft substitutes," *J. Orthop. Res.*, vol. 26, no. 10, pp. 1363–1370, Oct. 2008, doi: 10.1002/jor.20648.

[48] T. Kokubo and H. Takadama, "How useful is SBF in predicting in vivo bone bioactivity?," *Biomaterials*, vol. 27, no. 15, pp. 2907–2915, May 2006, doi: 10.1016/j.biomaterials.2006.01.017.

[49] E. Marini, P. Ballanti, G. Silvestrini, F. Valdinucci, and E. Bonucci, "The presence of different growth factors does not influence bone response to hydroxyapatite: Preliminary results," *Journal of Orthopaedics and Traumatology*, vol. 5, no. 1. SpringerOpen, pp. 34–43, Apr. 2004, doi: 10.1007/s10195-004-0037-6.

[50] R. Z. LeGeros, "Calcium phosphate-based osteoinductive materials," *Chemical Reviews*, vol. 108, no. 11. American Chemical Society, pp. 4742–4753, Nov. 2008, doi: 10.1021/cr800427g.

[51] S. V. Dorozhkin, "Calcium orthophosphates in nature, biology and medicine," *Materials*, vol. 2, no. 2. Multidisciplinary Digital Publishing Institute (MDPI), pp. 399–498, 2009, doi:

10.3390/ma2020399.

[52] L. Lin, K. L. Chow, and Y. Leng, "Study of hydroxyapatite osteoinductivity with an osteogenic differentiation of mesenchymal stem cells," *J. Biomed. Mater. Res. - Part A*, vol. 89, no. 2, pp. 326–335, May 2009, doi: 10.1002/jbm.a.31994.

[53] U. Ripamonti, "Osteoinduction in porous hydroxyapatite implanted in heterotopic sites of different animal models," *Biomaterials*, vol. 17, no. 1, pp. 31–35, Jan. 1996, doi: 10.1016/0142-9612(96)80752-6.

[54] A. K. Gosain *et al.*, "A 1-Year Study of Osteoinduction in Hydroxyapatite-Derived Biomaterials in an Adult Sheep Model: Part I," *Plast. Reconstr. Surg.*, vol. 109, no. 2, 2002, [Online]. Available: https://journals.lww.com/plasreconsurg/Fulltext/2002/02000/A_1_Year_Study_of_Osteoinduction_in.32.aspx.

[55] L. Cheng *et al.*, "Osteoinduction of hydroxyapatite/β-tricalcium phosphate bioceramics in mice with a fractured fibula," *Acta Biomater.*, vol. 6, no. 4, pp. 1569–1574, Apr. 2010, doi: 10.1016/j.actbio.2009.10.050.

[56] H. Yuan *et al.*, "Osteoinductive ceramics as a synthetic alternative to autologous bone grafting," *Proc. Natl. Acad. Sci. U. S. A.*, vol. 107, no. 31, pp. 13614–13619, Aug. 2010, doi: 10.1073/pnas.1003600107.

[57] J. P. Ribeiro, E. A. Astudillo-Ortiz, P. S. Babo, and M. E. Gomes, "Tissue engineering strategies for the treatment of skeletal maxillofacial defects resulting from neoplasms resections," in *Biomaterials for 3D Tumor Modeling*, Elsevier, 2020, pp. 697–730.

[58] B. B. Mendes, M. Gómez-Florit, P. S. Babo, R. M. Domingues, R. L. Reis, and M. E. Gomes, "Blood derivatives awaken in regenerative medicine strategies to modulate wound healing," *Adv. Drug Deliv. Rev.*, vol. 129, pp. 376–393, Apr. 2018, doi: 10.1016/j.addr.2017.12.018.

[59] L. D. F. F. Almeida *et al.*, "Hyaluronic acid hydrogels incorporating platelet lysate enhance human pulp cell proliferation and differentiation," *J. Mater. Sci. Mater. Med.*, vol. 29, no. 6, p. 88, 2018, doi: 10.1007/s10856-018-6088-7.

[60] N. Fekete *et al.*, "Platelet lysate from whole blood-derived pooled platelet concentrates and apheresis-derived platelet concentrates for the isolation and expansion of human bone marrow mesenchymal stromal cells: Production process, content and identification of active comp," *Cytotherapy*, vol. 14, no. 5, pp. 540–554, 2012, doi: 10.3109/14653249.2012.655420.

[61] R. Crespo-Diaz *et al.*, "Platelet lysate consisting of a natural repair proteome supports human mesenchymal stem cell proliferation and chromosomal stability," *Cell Transplant.*, vol. 20, no. 6, pp. 797–811, 2011, doi: 10.3727/096368910X543376.

[62] T. M. Fortunato, C. Beltrami, C. Emanueli, P. A. De Bank, and G. Pula, "Platelet lysate gel and endothelial progenitors stimulate microvascular network formation in vitro: Tissue engineering implications," *Sci. Rep.*, vol. 6, no. 1, pp. 1–15, May 2016, doi: 10.1038/srep25326.

[63] P. S. P. S. Babo, V. E. V. E. Santo, M. E. M. E. Gomes, and R. L. R. L. Reis, "Development

of an Injectable Calcium Phosphate/Hyaluronic Acid Microparticles System for Platelet Lysate Sustained Delivery Aiming Bone Regeneration," *Macromol. Biosci.*, vol. 16, no. 11, pp. 1662–1677, Nov. 2016, doi: 10.1002/mabi.201600141.

[64] P. Babo *et al.*, "Platelet lysate membranes as new autologous templates for tissue engineering applications," *Inflamm. Regen.*, vol. 34, no. 1, pp. 033–044, 2014, doi: 10.2492/inflammregen.34.033.

[65] P. S. Babo, R. L. Reis, and M. E. Gomes, "Production and characterization of hyaluronic acid microparticles for the controlled delivery of growth factors using a spray/dehydration method," *J. Biomater. Appl.*, vol. 31, no. 5, pp. 693–707, 2016, doi: 10.1177/0885328216669475.

[66] M. C. Phipps, Y. Xu, and S. L. Bellis, "Delivery of Platelet-Derived Growth Factor as a Chemotactic Factor for Mesenchymal Stem Cells by Bone-Mimetic Electrospun Scaffolds," *PLoS One*, vol. 7, no. 7, p. e40831, Jul. 2012, doi: 10.1371/journal.pone.0040831.

[67] K. Schallmoser *et al.*, "Human platelet lysate can replace fetal bovine serum for clinical-scale expansion of functional mesenchymal stromal cells," *Transfusion*, vol. 47, no. 8, pp. 1436–1446, Aug. 2007, doi: 10.1111/j.1537-2995.2007.01220.x.

[68] J. Kurita *et al.*, "Enhanced vascularization by controlled release of platelet-rich plasma impregnated in biodegradable gelatin hydrogel," *Ann. Thorac. Surg.*, vol. 92, no. 3, pp. 837–844, Sep. 2011, doi: 10.1016/j.athoracsur.2011.04.084.

[69] M. Matsui and Y. Tabata, "Enhanced angiogenesis by multiple release of platelet-rich plasma contents and basic fibroblast growth factor from gelatin hydrogels," *Acta Biomater.*, vol. 8, no. 5, pp. 1792–1801, May 2012, doi: 10.1016/j.actbio.2012.01.016.

[70] P. Van Pham *et al.*, "Activated platelet-rich plasma improves adipose-derived stem cell transplantation efficiency in injured articular cartilage," 2013. doi: 10.1186/scrt277.

[71] V. E. Santo, A. R. C. Duarte, E. G. Popa, M. E. Gomes, J. F. Mano, and R. L. Reis, "Enhancement of osteogenic differentiation of human adipose derived stem cells by the controlled release of platelet lysates from hybrid scaffolds produced by supercritical fluid foaming," *J. Control. Release*, vol. 162, no. 1, pp. 19–27, Aug. 2012, doi: 10.1016/j.jconrel.2012.06.001.

[72] P. Blair *et al.*, "Enhancement of osteogenic differentiation of human adipose derived stem cells by the controlled release of platelet lysates from hybrid scaffolds produced by supercritical fluid foaming," *Transfusion*, vol. 4, no. 4, pp. 19–27, 2012, doi: 10.1016/j.blre.2009.04.001.

[73] N. Chevallier *et al.*, "Osteoblastic differentiation of human mesenchymal stem cells with platelet lysate," *Biomaterials*, vol. 31, no. 2, pp. 270–278, Jan. 2010, doi: 10.1016/j.biomaterials.2009.09.043.

[74] R. Costa-Almeida *et al.*, "The effects of platelet lysate patches on the activity of tendon-derived cells," *Acta Biomater.*, Jan. 2018, doi: 10.1016/j.actbio.2018.01.006.

[75] P. S. Babo *et al.*, "Platelet Lysate-Loaded Photocrosslinkable Hyaluronic Acid Hydrogels for Periodontal Endogenous Regenerative Technology," *ACS Biomater. Sci. Eng.*, vol. 3, no. 7, pp. 1359–1369, 2017, doi: 10.1021/acsbiomaterials.6b00508.

[76] V. E. Santo, M. E. Gomes, J. F. Mano, and R. L. Reis, "Chitosan-chondroitin sulphate nanoparticles for controlled delivery of platelet lysates in bone regenerative medicine," *J. Tissue Eng. Regen. Med.*, vol. 6, no. SUPPL. 3, Dec. 2012, doi: 10.1002/term.1519.

[77] P. S. P. S. Babo *et al.*, "The Role of a Platelet Lysate-Based Compartmentalized System as a Carrier of Cells and Platelet-Origin Cytokines for Periodontal Tissue Regeneration," *Tissue Eng. - Part A*, vol. 22, no. 19–20, pp. 1164–1175, Oct. 2016, doi: 10.1089/ten.tea.2016.0226.

[78] B. B. Mendes *et al.*, "Intrinsically Bioactive Cryogels Based on Platelet Lysate Nanocomposites for Hemostasis Applications," *Biomacromolecules*, vol. 21, no. 9, pp. 3678–3692, 2020, doi: 10.1021/acs.biomac.0c00787.

[79] U. J. Kim, S. Kuga, M. Wada, T. Okano, and T. Kondo, "Periodate oxidation of crystalline cellulose," *Biomacromolecules*, vol. 1, no. 3, pp. 488–492, 2000, doi: 10.1021/bm0000337.

[80] F. Lindberg, J. Heinrichs, F. Ericson, P. Thomsen, and H. Engqvist, "Hydroxylapatite growth on single-crystal rutile substrates," *Biomaterials*, vol. 29, no. 23, pp. 3317–3323, Aug. 2008, doi: 10.1016/j.biomaterials.2008.04.034.

[81] G. Thrivikraman *et al.*, "Rapid fabrication of vascularized and innervated cell-laden bone models with biomimetic intrafibrillar collagen mineralization," *Nat. Commun.*, vol. 10, no. 1, 2019, doi: 10.1038/s41467-019-11455-8.

[82] A. L. Boskey and P. G. Robey, "The Composition of Bone," in *Primer on the Metabolic Bone Diseases and Disorders of Mineral Metabolism: Eighth Edition*, Wiley Blackwell, 2013, pp. 49–58.

[83] J. P. Gorski, "Biomineralization of bone: A fresh view of the roles of non-collagenous proteins," *Front. Biosci.*, vol. 16, no. 7, pp. 2598–2621, Jun. 2011, doi: 10.2741/3875.

[84] L. Yu and M. Wei, "Biomineralization of Collagen-Based Materials for Hard Tissue Repair," *Int. J. Mol. Sci. 2021, Vol. 22, Page 944*, vol. 22, no. 2, p. 944, Jan. 2021, doi: 10.3390/IJMS22020944.

[85] G. He, T. Dahl, A. Veis, and A. George, "Nucleation of apatite crystals in vitro by self-assembled dentin matrix protein 1," *Nat. Mater.*, vol. 2, no. 8, pp. 552–558, Jul. 2003, doi: 10.1038/nmat945.

[86] S. I. Stupp, G. C. Mejicano, and J. A. Hanson, "Organoapatites: Materials for artificial bone. II. Hardening reactions and properties," *J. Biomed. Mater. Res.*, vol. 27, no. 3, pp. 289–299, Mar. 1993, doi: 10.1002/JBM.820270303.

[87] J. D. Hartgerink, E. Beniash, and S. I. Stupp, "Self-Assembly and Mineralization of Peptide-Amphiphile Nanofibers," *Science (80-.).*, vol. 294, no. 5547, pp. 1684–1688, Nov. 2001, doi: 10.1126/SCIENCE.1063187.

[88] E. D. Spoerke, S. G. Anthony, and S. I. Stupp, "Enzyme Directed Templating of Artificial Bone Mineral," *Adv. Mater.*, vol. 21, no. 4, pp. 425–430, Jan. 2009, doi: 10.1002/ADMA.200802242.

[89] L. Niu *et al.*, "Collagen intrafibrillar mineralization as a result of the balance between osmotic equilibrium and electroneutrality," *Nat. Mater. 2016 163*, vol. 16, no. 3, pp. 370–

378, Nov. 2016, doi: 10.1038/nmat4789.

[90] Y. Liu *et al.*, "Intrafibrillar Collagen Mineralization Produced by Biomimetic Hierarchical Nanoapatite Assembly," *Adv. Mater.*, vol. 23, no. 8, pp. 975–980, Feb. 2011, doi: 10.1002/ADMA.201003882.

[91] T. T. Thula, D. E. Rodriguez, M. H. Lee, L. Pendi, J. Podschun, and L. B. Gower, "In vitro mineralization of dense collagen substrates: A biomimetic approach toward the development of bone-graft materials," *Acta Biomater.*, vol. 7, no. 8, pp. 3158–3169, Aug. 2011, doi: 10.1016/J.ACTBIO.2011.04.014.

[92] D. Gebauer *et al.*, "A transparent hybrid of nanocrystalline cellulose and amorphous calcium carbonate nanoparticles," *Nanoscale*, vol. 3, no. 9, pp. 3563–3566, Sep. 2011, doi: 10.1039/C1NR10681C.

[93] P. R. Amable *et al.*, "Platelet-rich plasma preparation for regenerative medicine: optimization and quantification of cytokines and growth factors," *Stem Cell Res. Ther. 2013 43*, vol. 4, no. 3, pp. 1–13, Jun. 2013, doi: 10.1186/SCRT218.

[94] B. J. Kirby and E. F. Hasselbrink, "Zeta potential of microfluidic substrates: 1. Theory, experimental techniques, and effects on separations," *Electrophoresis*, vol. 25, no. 2, pp. 187–202, Jan. 2004, doi: 10.1002/ELPS.200305754.

[95] A. F. D. De Namor and M. Shehab, "Recognition of biologically and environmentally important phosphate anions by calix[4]pyrrole: Thermodynamic aspects," *J. Phys. Chem. A*, vol. 108, no. 35, pp. 7324–7330, Sep. 2004, doi: 10.1021/jp031343x.

[96] T. Abitbol, E. Kloser, and D. G. Gray, "Estimation of the surface sulfur content of cellulose nanocrystals prepared by sulfuric acid hydrolysis," *Cellulose*, vol. 20, no. 2, pp. 785–794, 2013, doi: 10.1007/s10570-013-9871-0.

[97] S. Beck, M. Méthot, and J. Bouchard, "General procedure for determining cellulose nanocrystal sulfate half-ester content by conductometric titration," *Cellulose*, vol. 22, no. 1, pp. 101–116, 2015, doi: 10.1007/s10570-014-0513-y.

[98] X. M. Dong, J. F. Revol, and D. G. Gray, "Effect of microcrystallite preparation conditions on the formation of colloid crystals of cellulose," *Cellulose*, vol. 5, no. 1, pp. 19–32, 1998, doi: 10.1023/A:1009260511939.

[99] D. da Silva Perez, S. Montanari, and M. R. Vignon, "TEMPO-mediated oxidation of cellulose III," *Biomacromolecules*, vol. 4, no. 5, pp. 1417–1425, Sep. 2003, doi: 10.1021/bm034144s.

[100] J. S. Gaffney, N. A. Marley, and D. E. Jones, "Fourier Transform Infrared (FTIR) Spectroscopy," in *Characterization of Materials*, Hoboken, NJ, USA: John Wiley & Sons, Inc., 2012, pp. 1–33.

[101] M. M. Beasley, E. J. Bartelink, L. Taylor, and R. M. Miller, "Comparison of transmission FTIR, ATR, and DRIFT spectra: Implications for assessment of bone bioapatite diagenesis," *J. Archaeol. Sci.*, vol. 46, no. 1, pp. 16–22, Jun. 2014, doi: 10.1016/j.jas.2014.03.008.

[102] M. Kaliva and M. Vamvakaki, "Nanomaterials characterization," in *Polymer Science and Nanotechnology*, Elsevier, 2020, pp. 401–433.

[103] A. Polini and F. Yang, "Physicochemical characterization of nanofiber composites," in *Nanofiber Composites for Biomedical Applications*, Elsevier Inc., 2017, pp. 97–115.

[104] R. D. Holbrook, A. A. Galyean, J. M. Gorham, A. Herzing, and J. Pettibone, "Overview of Nanomaterial Characterization and Metrology," in *Frontiers of Nanoscience*, vol. 8, Elsevier Ltd, 2015, pp. 47–87.

[105] K. R. Rajisha, B. Deepa, L. A. Pothan, and S. Thomas, "Thermomechanical and spectroscopic characterization of natural fibre composites," in *Interface Engineering of Natural Fibre Composites for Maximum Performance*, Elsevier, 2011, pp. 241–274.

[106] B. T. Tomoda *et al.*, "Characterization of biopolymer membranes and films: Physicochemical, mechanical, barrier, and biological properties," in *Biopolymer Membranes and Films*, Elsevier, 2020, pp. 67–95.

[107] S. A. Hashemifard, A. Khosravi, F. Abdollahi, Z. Alihemati, and M. Rezaee, "Synthetic polymeric membranes for gas and vapor separations," in *Synthetic Polymeric Membranes for Advanced Water Treatment, Gas Separation, and Energy Sustainability*, Elsevier, 2020, pp. 217–272.

[108] A. Barhoum and M. Luisa García-Betancourt, "Physicochemical characterization of nanomaterials: Size, morphology, optical, magnetic, and electrical properties," in *Emerging Applications of Nanoparticles and Architectural Nanostructures: Current Prospects and Future Trends*, Elsevier Inc., 2018, pp. 279–304.

[109] P. D. Nellist, "Scanning transmission electron microscopy," in *Springer Handbooks*, Springer, 2019, pp. 49–99.

[110] J. Liu, "Scanning transmission electron microscopy and its application to the study of nanoparticles and nanoparticle systems," *Microscopy*, vol. 54, no. 3, pp. 251–278, Jun. 2005, doi: 10.1093/jmicro/dfi034.

[111] C. F. Guimarães, L. Gasperini, A. P. Marques, and R. L. Reis, "The stiffness of living tissues and its implications for tissue engineering," *Nature Reviews Materials*, vol. 5, no. 5. Nature Research, pp. 351–370, May 01, 2020, doi: 10.1038/s41578-019-0169-1.

[112] P. P. Carvalho *et al.*, "The Effect of Storage Time on Adipose-Derived Stem Cell Recovery from Human Lipoaspirates," *Cells Tissues Organs*, vol. 194, no. 6, pp. 494–500, Nov. 2011, doi: 10.1159/000324892.

[113] A. O. Luby, K. Ranganathan, J. V. Lynn, N. S. Nelson, A. Donneys, and S. R. Buchman, "Stem cells for bone regeneration: Current state and future directions," *J. Craniofac. Surg.*, vol. 30, no. 3, pp. 730–735, 2019, doi: 10.1097/SCS.0000000000005250.

[114] J. R. Dudas *et al.*, "The osteogenic potential of adipose-derived stem cells for the repair of rabbit calvarial defects," *Ann. Plast. Surg.*, vol. 56, no. 5, pp. 543–548, May 2006, doi: 10.1097/01.sap.0000210629.17727.bd.

[115] C. Pendleton, Q. Li, D. A. Chesler, K. Yuan, H. Guerrero-Cazares, and A. Quinones-Hinojosa, "Mesenchymal Stem Cells Derived from Adipose Tissue vs Bone Marrow: In Vitro Comparison of Their Tropism towards Gliomas," *PLoS One*, vol. 8, no. 3, p. e58198, Mar. 2013, doi: 10.1371/journal.pone.0058198.

[116] P. A. Zuk *et al.*, "Human adipose tissue is a source of multipotent stem cells," *Mol. Biol.*

Cell, vol. 13, no. 12, pp. 4279–4295, Dec. 2002, doi: 10.1091/mbc.E02-02-0105.

[117] C. M. Cowan *et al.*, "Adipose-derived adult stromal cells heal critical-size mouse calvarial defects," *Nat. Biotechnol.*, vol. 22, no. 5, pp. 560–567, May 2004, doi: 10.1038/nbt958.

[118] L. N. Melek, "Tissue engineering in oral and maxillofacial reconstruction," *Tanta Dent. J.*, vol. 12, no. 3, pp. 211–223, 2015, doi: 10.1016/j.tdj.2015.05.003.

[119] S. Kern, H. Eichler, J. Stoeve, H. Klüter, and K. Bieback, "Comparative Analysis of Mesenchymal Stem Cells from Bone Marrow, Umbilical Cord Blood, or Adipose Tissue," *Stem Cells*, vol. 24, no. 5, pp. 1294–1301, May 2006, doi: 10.1634/stemcells.2005-0342.

[120] A. Schäffler and C. Büchler, "Concise Review: Adipose Tissue-Derived Stromal Cells-Basic and Clinical Implications for Novel Cell-Based Therapies," *Stem Cells*, vol. 25, no. 4, pp. 818–827, 2007, doi: 10.1634/stemcells.2006-0589.

[121] O. G. Davies, P. R. Cooper, R. M. Shelton, A. J. Smith, and B. A. Scheven, "A comparison of the in vitro mineralisation and dentinogenic potential of mesenchymal stem cells derived from adipose tissue, bone marrow and dental pulp," *J. Bone Miner. Metab.*, vol. 33, no. 4, pp. 371–382, 2015, doi: 10.1007/s00774-014-0601-y.

[122] N. Kishimoto and S. Tran, "Dedifferentiated Fat (DFAT) Cells: a cell source for oral and maxillofacial tissue engineering," *Oral Dis.*, vol. 24, no. 7, pp. 42–49, 2018, doi: 10.1111/ijlh.12426.

[123] G. K. Sándor *et al.*, "Adipose Stem Cell Tissue–Engineered Construct Used to Treat Large Anterior Mandibular Defect: A Case Report and Review of the Clinical Application of Good Manufacturing Practice–Level Adipose Stem Cells for Bone Regeneration," *J. Oral Maxillofac. Surg.*, vol. 71, no. 5, pp. 938–950, May 2013, doi: 10.1016/j.joms.2012.11.014.

[124] G. B. Sándor, "Tissue engineering of bone: Clinical observations with adipose-derived stem cells, resorbable scaffolds, and growth factors," *Ann. Maxillofac. Surg.*, vol. 2, no. 1, p. 8, 2012, doi: 10.4103/2231-0746.95308.

[125] K. Mesimäki *et al.*, "Novel maxillary reconstruction with ectopic bone formation by GMP adipose stem cells," *Int. J. Oral Maxillofac. Surg.*, vol. 38, no. 3, pp. 201–209, 2009, doi: 10.1016/j.ijom.2009.01.001.

[126] H.-H. Sun, T. Jin, Q. Yu, and F.-M. Chen, "Biological approaches toward dental pulp regeneration by tissue engineering," *J. Tissue Eng. Regen. Med.*, vol. 5, no. 4, pp. e1–e16, Apr. 2011, doi: 10.1002/term.369.

[127] G. T. J. Huang, S. Gronthos, and S. Shi, "Critical reviews in oral biology & medicine: Mesenchymal stem cells derived from dental tissues vs. those from other sources: Their biology and role in Regenerative Medicine," *J. Dent. Res.*, vol. 88, no. 9, pp. 792–806, 2009, doi: 10.1177/0022034509340867.

[128] C. Michiels, "Endothelial cell functions," *J. Cell. Physiol.*, vol. 196, no. 3, pp. 430–443, Sep. 2003, doi: 10.1002/jcp.10333.

[129] P. Carmeliet, "Mechanisms of angiogenesis and arteriogenesis," *Nature Medicine*, vol. 6, no. 4. Nature Publishing Group, pp. 389–395, Apr. 2000, doi: 10.1038/74651.

[130] K. Ahn, S. Pan, K. Beningo, and D. Hupe, "A permanent human cell line (EA.hy926) preserves the characteristics of endothelin converting enzyme from primary human umbilical vein endothelial cells," *Life Sci.*, vol. 56, no. 26, pp. 2331–2341, 1995, doi: 10.1016/0024-3205(95)00227-W.

[131] C. J. Edgell, C. C. McDonald, and J. B. Graham, "Permanent cell line expressing human factor VIII-related antigen established by hybridization.," *Proc. Natl. Acad. Sci. U. S. A.*, vol. 80, no. 12, pp. 3734–7, Jun. 1983, doi: 10.1073/pnas.80.12.3734.

[132] M. Boerma, G. R. Burton, J. Wang, L. M. Fink, R. E. McGehee, and M. Hauer-Jensen, "Comparative expression profiling in primary and immortalized endothelial cells: Changes in gene expression in response to hydroxy methylglutaryl-coenzyme A reductase inhibition," *Blood Coagul. Fibrinolysis*, vol. 17, no. 3, pp. 173–180, 2006, doi: 10.1097/01.mbc.0000220237.99843.a1.

[133] J. O'Brien, I. Wilson, T. Orton, and F. Pognan, "Investigation of the Alamar Blue (resazurin) fluorescent dye for the assessment of mammalian cell cytotoxicity," *Eur. J. Biochem.*, vol. 267, no. 17, pp. 5421–5426, Sep. 2000, doi: 10.1046/j.1432-1327.2000.01606.x.

[134] P. Magnusson, L. Larsson, M. Magnusson, M. W. J. Davie, and C. A. Sharp, "Isoforms of bone alkaline phosphatase: Characterization and origin in human trabecular and cortical bone," *J. Bone Miner. Res.*, vol. 14, no. 11, pp. 1926–1933, Nov. 1999, doi: 10.1359/jbmr.1999.14.11.1926.

[135] J. Jozefczuk and J. Adjaye, "Quantitative real-time PCR-based analysis of gene expression," in *Methods in Enzymology*, vol. 500, Academic Press Inc., 2011, pp. 99–109.

[136] B. Ziaeian, J. L. Nourse, T. Palmer, P. H. Schwartz, and L. A. Flanagan, "Immunocytochemical Analysis of Human Stem Cells," in *Human Stem Cell Manual*, Elsevier Inc., 2012, pp. 249–270.

[137] D. E. Rodriguez *et al.*, "Multifunctional role of osteopontin in directing intrafibrillar mineralization of collagen and activation of osteoclasts," *Acta Biomater.*, vol. 10, no. 1, pp. 494–507, Jan. , doi: 10.1016/j.actbio.2013.10.010.

[138] J. A. Cooper, B. R. Mintz, S. L. Palumbo, and W. J. Li, "Assays for determining cell differentiation in biomaterials," in *Characterization of Biomaterials*, Elsevier Ltd., 2012, pp. 101–137.

[139] B. Matthews and D. Andrew, "Microvascular Architecture and Exchange in Teeth," *Microcirculation*, vol. 2, no. 4, pp. 305–313, Jan. 1995, doi: 10.3109/10739689509148275.

[140] S. Yoshida and H. Ohshima, "Distribution and organization of peripheral capillaries in dental pulp and their relationship to odontoblasts," *Anat. Rec.*, vol. 245, no. 2, pp. 313–326, 1996, doi: 10.1002/(SICI)1097-0185(199606)245:2<313::AID-AR14>3.0.CO;2-S.

[141] J. W. Yang, Y. F. Zhang, Z. Y. Sun, G. T. Song, and Z. Chen, "Dental pulp tissue engineering with bFGF-incorporated silk fibroin scaffolds," *J. Biomater. Appl.*, vol. 30, no. 2, pp. 221–229, 2015, doi: 10.1177/0885328215577296.

[142] W. L. Dissanayaka and C. Zhang, "The Role of Vasculature Engineering in Dental Pulp Regeneration," *J. Endod.*, vol. 43, no. 9, pp. S102–S106, 2017, doi:

10.1016/j.joen.2017.09.003.

[143] J. Rouwkema, J. De Boer, and C. A. Van Blitterswijk, "Endothelial cells assemble into a 3-dimensional prevascular network in a bone tissue engineering construct," *Tissue Eng.*, vol. 12, no. 9, pp. 2685–2693, 2006, doi: 10.1089/ten.2006.12.2685.

Chapter III.

Bioinspired organic-inorganic nanocomposite scaffolds for bone tissue engineering

This chapter is based on the following publication:

J. P. Ribeiro, R. M. A. Domingues, P. S. Babo, R. L. Reis, M. Gómez-Florit and M. E. Gomes, "Bioinspired organic-inorganic nanocomposite scaffolds for bone tissue engineering", submitted.

CHAPTER III. Bioinspired organic-inorganic nanocomposite scaffolds for bone tissue engineering

J. P. Ribeiro[1,2], R. M. A. Domingues[1,2], P. S. Babo[1,2], R. L. Reis[1,2], M. Gómez-Florit[1,2] and M. E. Gomes[1,2]

[1] 3B's Research Group, I3Bs – Research Institute on Biomaterials, Biodegradables and Biomimetics, University of Minho, Headquarters of the European Institute of Excellence on Tissue Engineering and Regenerative Medicine, AvePark, Parque de Ciência e Tecnologia, Zona Industrial da Gandra, 4805-017 Barco, Guimarães, Portugal

[2] ICVS/3B's - PT Government Associate Laboratory, Braga/Guimarães, Portugal

2.1. Abstract

Bone is an organic-inorganic composite whose extracellular matrix (ECM) is heavily mineralized on the nanoscale, and where cells and their processes are embedded. Nowadays, there are no strategies that fully and successfully emulate the true complexity of bone tissue and the nanoscale biomineralized architecture. Herein, we propose a biomimetic strategy where a bioactive cryogel scaffold based on platelet lysate (PL) crosslinked through aldehyde-functionalized cellulose nanocrystals (a-CNCs) incorporates mineralized CNCs (m-CNCs) in order to replicate the nanoscale biomineralization microenvironment and promote the osteogenic differentiation of stem cells. Moreover, we intended to mimic the native non-collagenous proteins (NCPs) role on regulating the deposition of both intra- and extrafibrillar apatite in collagen with the m-CNCs. The developed cryogels enhanced stem cell proliferation, metabolic activity, and alkaline phosphatase activity as well as up-regulated the expression of bon-related markers, without osteogenic supplementation, demonstrating their osteoinductive properties. Ultimately, the proposed nanoscale mineralized cryogel scaffolds provide an alternative biomaterial for bone tissue engineering applications with a great level of biomimicry that may be applied in broad bone regenerative approaches.

Keywords: Nanoscale biomineralization, non-collagenous proteins, cryogels, cellulose nanocrystals, hydroxyapatite, platelet lysate

2.2. Introduction

Bone is a composite material whose extracellular matrix (ECM) consists mostly of type I collagen fibrils co-assembled with non-collagenous proteins and apatite crystals that form a highly complex and organized scaffold [1]–[3]. On a ultrastructural level, these hydroxyapatite (Hap) crystals have a platelet-shaped form and are hierarchically allocated both within and between the collagen fibres, providing bone outstanding load-bearing function [1], [3], [4]. During bone biomineralization, the deposition of apatite crystals within (intrafibrillar) and between (extrafibrillar) collagen fibrils is regulated by matrix non-collagenous proteins (NCPs), among other factors [6]. NCPs, such as osteocalcin (OC) and osteopontin (OPN), are anionic matrix proteins able to regulate the sequestration of mineral ions to form metastable nanodroplets of amorphous calcium phosphate, which penetrate the interstices of collagen fibrils, later transforming into thermodynamically stable carbonated, calcium-deficient Hap crystals [5], [6]. NCPs might not only stabilize the amorphous phase by inhibiting apatite nucleation, but also play an active role in aiding the formation of negatively charged complexes of mineral precursors that allow them to enter into collagen through electrostatic attraction and thus allowing the intrafibrillar collagen mineralization [6].

Bone defects caused by trauma, tumor excision, or pathologic bone resorption affect and limit patients aesthetically and functionally, reducing their quality of life [7] In the case of critical-size defects, the gold standard for bone reconstruction is the use of autologous or allogenic bone grafts, normally from tibia or fibula [8], iliac crest [9], or ribs [10]. Nevertheless, their use presents major drawbacks including discomfort, pain, invasive harvest, risk of donor site morbidity, and limited functional and aesthetic recovery [9]. On the other hand, allografts can induce disease transmission and immune rejection [9], [11], [12]. Over the past years, several tissue engineering and regenerative medicine (TERM) approaches have been proposed for bone regeneration [13]. Normally, they are the result of a combination of inorganic (ceramics, metals, or metallic alloys) and/or organic (synthetic or natural origin polymers) biomaterials-based scaffolds, progenitor cells, and biophysical/biochemical stimuli [14], [15]. These strategies have deeply contributed for the increasing level of success towards bone regeneration. For instance, the combination of ceramics, as calcium phosphates, with different polymers, such as polycaprolactone, chitosan, or fibrin, among others, has demonstrated to enhance the ability for osteoblasts to migrate through the pores of the scaffolds, promote osteogenic differentiation and, consequently, new bone growth [16]–[21]. However, these strategies fail to mimic the true complexity of bone tissue, including the

nanoscale-calcified ECM and biofunctional properties that favors the biomineralization process and vascularization.

Naturally-occurring cellulose nanocrystals (CNCs) have been extensively applied in TERM strategies as nanofillers and crosslinking agents due to their high mechanical strength, biocompatibility, low density, high aspect ratio and surface area, and convenient surface chemistry [22]. Moreover, their typical production process results in a negative surface charge that improves their colloidal stability [23]. Owing to its reactive surface chemistry, we have previously modified CNCs with aldehyde groups (a-CNCs) to increase the crosslinking of low strength matrices, such as hyaluronic acid or platelet lysate (PL) [24]–[26]. Actually, PL is a liquid blood derivative prepared from clinical-standard platelet concentrates rich in growth factors and self-assembling structural proteins, among others, capable of enhancing angiogenesis, stem cells recruitment and tissue regeneration, which has been used to produce various types of PL-based hydrogels and scaffolds for different TERM strategies [24]–[26].

In this work, bioinspired by the role of negatively charged NCPs in the formation of apatite crystals in bone, we aimed to mimic their function using negatively charged CNCs to then emulate the initial stage of the intrafibrillar biomineralization process. We hypothesized that scaffolds composed of PL reinforced with varying contents of a-CNCs and mineralized CNCs (m-CNCs) would mimic the nanoscale biomineralization microenvironment while acting as a stable three-dimensional (3D) network and locally delivering the biologically relevant PL-derived proteins to promote the osteogenic differentiation of progenitor/stem cells. The scaffolds and its precursors were thoroughly characterized regarding their chemical, morphological, microstructural, and mechanical properties, as well as their swelling and degradation profiles. The biological performance, particularly the osteogenic potential, of the developed cryogel scaffolds was evaluated using human adipose tissue-derived stem cells (hASCs) and human dental pulp cells (hDPCs) in vitro. For this, the impact of the mineralized cryogel scaffolds on cells proliferation, metabolic activity, differentiation, and gene expression was assessed.

2.3. Materials and Methods

2.3.1. Production of cryogels precursors

Synthesis of CNCs and aldehyde functionalization. CNCs were isolated from microcrystalline cellulose (MCC, Sigma-Aldrich, USA), following a well-established sulfuric acid hydrolysis described by Bondeson *et al.* and adapted by Domingues *et al* [27], [28]. Then,

aldehyde-modified CNCs (a-CNCs) were produced through sodium periodate ($NaIO_4$) oxidation route, according to the procedures described elsewhere with minor modifications [28]–[30]. Further details can be found in Supporting Information.

CNCs mineralization. m-CNCs production was inspired by strategies reported elsewhere [31] with some modifications. In brief, a simplified simulated body fluid (s-SBF) solution composed of 140.0 mM sodium chloride (NaCl, Honeywell, USA), 2.5 mM calcium chloride hexahydrate ($CaCl_2.6H_2O$, Sigma-Aldrich, USA), 1.0 mM disodium hydrogen phosphate (Na_2HPO_4, 98%, abcr GmbH, Germany), and 20 mM hydrochloric acid (HCl, VWR, France) was prepared 24 h in advance and stored at RT preventing air and light exposure to avoid undesired precipitation. Thereafter, CNCs aqueous solution of 0.8% (w/v), prepared from the original CNCs stock solution (2.5 wt.%), was added to s-SBF in a closed flask in different amounts to obtain the calcium ions (in s-SBF) and sulfonic groups (in CNCs) molar ratio (Ca^{2+}/SO_3) of 10:1, 20:1, and 40:1. The suspension was then vigorously stirred using a magnetic stirrer until no bulk particles were apparent and then moved to an ultrasonic water bath (DT 100 H Sonorex Digitec, Bandelin, Germany) for 30 min to disperse evenly. Afterwards, the mixture pH was adjusted to two different values, 6.9 and 7.9, with the addition of tris(hydroxymethyl)aminomethane (Trisbase, Alfa Aesar, Germany), to avoid that Ca^{2+}/SO_3^- molar ratio was disturbed. After this, the solutions were placed in an orbital/linear thermostatic shaking water bath (OLS 200, Grant, UK) at 37°C and 150 rpm for 1 h. The ultrasound and shaking steps were repeated three times. Subsequently, the precipitated products were collected by centrifugation (Eppendorf 5810R, Germany) at 3220 xg and 15°C for 10 min and washed several times with anhydrous ethanol and ultrapure water (Milli-Q, 18.2 MΩ.cm) to remove the residual salts. Finally, CNCs/Hap nanocomposites were stored at 4 °C until further use.

Platelet lysate. PL used in this project was produced from platelet concentrates (PC) obtained from buffy coats, provided by "Serviço de Imunohemoterapia do Centro Hospitalar de São João" (CHSJ, Porto, Portugal), under an established cooperation protocol, approved by the Hospital Ethical Committee (approval number 363/18). The platelet count was performed at the CHSJ and the sample volume was adjusted to one million platelets per mL. PC lots were biologically qualified according to the Portuguese legislation (Decreto-Lei 100/2011) and stored at -80°C five days after collection. Thereafter, PC lots from ten different donors were subjected to three repeated freeze/thaw cycles (frozen with liquid nitrogen at −196°C and thawed in a 37°C water bath), lysing

the platelets and releasing their protein content. Then, the cellular debris were removed by centrifugation at 3220 xg for 5 min, and the supernatant was filtered through 0.45 μm sterile filters (TPP, Switzerland).

2.3.2. Physicochemical characterization of CNCs

Zeta potential. Surface charge was calculated for 0.1% (w/v) CNC suspensions in DI water. Briefly, 1 mL of each suspension was transferred into a Folded Capillary cell (DTS1060, Malvern) and zeta potential was measured by Zetasizer (Nano ZS, Malvern) (N=3).

Fourier transform infrared spectroscopy (FTIR) analysis. FTIR spectra were collected in attenuated total reflectance (ATR) mode (IRPrestige 21, Shimadzu, Japan) recording 32 scans in the range of 400–4000 cm^{-1} at a resolution of 4 cm^{-1}. All the measurements were performed using OriginPro 2018 software after baseline correction (N=3).

X-ray diffraction (XRD) analysis. The different CNCs samples were freeze-dried and then pressed on the sample holder to form a uniform film of material for analysis. The diffraction patterns measurements were performed using a Bragg–Brentano diffractometer (D8 Advance, Bruker, Germany) equipped with Cu Kα radiation. Data sets were collected in the 2θ range of 10–80° with a step size of 0.05° and 1 s for each step and processed using OriginPro 2018 software. Subsequently, the average crystallite size was calculated using the Scherrer equation (N=3).

Energy dispersive spectroscope (EDS) analysis. In order to estimate the Ca/P molar ratio of the Hap formed on the surface of CNCs, an EDS detector (INCAx-Act, PentaFET Precision, Oxford Instruments, UK) incorporated in scanning electron microscope (JSM-6010 LV, JEOL, Japan) was used. For this purpose, 0.01 and 0.001% (v/v) CNCs and CNCs/Hap dilutions were prepared from the stock solutions and sonicated (5 min, 60%; VCX750, Sonics & Materials Inc, USA) to disperse the nanoparticles. Then, a drop of each solution was placed on top of aluminium stubs fitted with conductive adhesive carbon tape (Media Lab System S.r.l., Italy) and tissue coverslips (polyethylene terephthalate, glycol-modified (PET-G); Sarstedt, Germany) cut at half, and allowed to dry until the procedure was performed. After drying, the samples were transferred into the EDS chamber and imaged at RT with an incident electron beam accelerated to 10 kV. After this, the Ca/P molar ratios were calculated for each sample (N=3).

Thermogravimetric analysis. CNCs samples were freeze-dried, weighted, transferred into platinum pans, and analysed according to the desired purpose using a simultaneous thermal analyser (STA7200, Hitachi, Japan) (N=3). For the determination of the water content and degradation temperature, samples were heated from 40°C to 105°C and then from 105°C to 600°C both at a 10°C/min heating rate for 15 min, under a N_2 atmosphere. Whereas, for the determination of the percentage of Hap, they were heated from 40°C to 600°C at 10°C/min heating rate for 15 min, after a 2-min isothermal period at 40°C under a N_2O_2 atmosphere.

2.3.3. Nanocomposite cryogels production

Nanocomposite cryogel scaffolds were prepared by mixing PL with different blends of a-CNCs and m-CNCs, using a double-barrel syringe (1:1 volume ratio) fitted with a static mixer placed at the outlet (Medmix, Germany) to homogenously extrude the cryogel scaffold precursor solution into square molds (12 well silicone chamber, Ibidi, Germany). For cryogel scaffolds without m-CNCs, barrel A was filled with PL and barrel B with a-CNCs dispersion at 2.4 wt.% concentration. For mineralized cryogels, barrel A was also filled with PL and barrel B with a-CNCs (1.8–2.4 wt.%) and m-CNCs dispersions (0.6–2.4 wt.%) to obtain a final nanoparticles concentration of 2.4 wt.%. Before extrusion, the viscous a-CNCs suspensions with or without m-CNCs were dispersed with an ultrasonic processor (30 s, 3 cycles, 60% amplitude; VCX750, Sonics & Materials Inc, USA) and sterilized under UV for 30 min. After extrusion into the molds, the cryogel precursors were frozen at -80°C on top of styrofoam and subsequently freeze-dried until full cryogelation. The final cryogel scaffolds formulations were named according to the type (defined after XRD analysis) of m-CNCs used and their concentrations: 0 wt.% (Control), 0.6 wt.% m-CNCs 6.9/20 (Amorphous-Low or A-Low), 2.4 wt.% m-CNCs 6.9/20 (Amorphous-High or A-High), 0.6 wt.% m-CNCs 7.9/20 (Crystalline-Low or C-Low), and 2.4 wt.% m-CNCs 7.9/20 (Crystalline-High or C-High).

2.3.4. Cellular Experiments

Human adipose-derived stem cells (hASCs). hASCs are multipotent stem cells which exhibit the ability to undergo osteogenic, chondrogenic, and adipogenic differentiation while expressing stem cell markers [32]–[35]. hASCs were obtained from lipoaspirate samples of the abdominal region of healthy donors undergoing plastic surgery under the scope of an established protocol with Hospital da Prelada (Porto, Portugal) and with the approval of the Hospital Ethics Committee (approval number 005/2019). The hASC isolation was performed using a previously optimized protocol [32]. hASCs were maintained in α-MEM (Sigma-Aldrich) supplemented with 10%

fetal bovine serum (FBS, ThermoFisher Scientific, USA) and 1% antibiotic/antimycotic (A/A, ThermoFisher Scientific) and incubated at 37°C in a 5% CO_2 high-humidity environment, with medium replacements every 2 to 3 days. Cells until passage 5 were used for this study.

Human dental pulp cells (hDPCs). hDPCs were isolated from human third molars, removed by orthodontic reasons, under a protocol established with the Malo Clinic (Porto, Portugal), approved by the ethical commission at 23/12/2014, as described by Almeida *et al.* [36]. Cells were expanded in 150 cm^2 culture flasks (TPP, Switzerland) and cultured with α-MEM (Sigma-Aldrich) supplemented with 10% FBS (ThermoFisher Scientific) and 1% A/A (ThermoFisher Scientific) using the standard culture conditions described previously. Cells until passage 5 were used for this study.

Live/Dead assay. After 4 days of culture, samples seeded with hASCs were gently rinsed with PBS, incubated with Calcein AM (Invitrogen, USA) 1:500 v/v in PBS for 30 min at 37°C and then with PI (Invitrogen) 1:1000 v/v solution in PBS also for 30 min at 37°C. Lastly, the cryogels were washed again with PBS to minimize background fluorescence and visualized using a confocal microscope (TCS SP8, Leica, Germany) (N=3).

Metabolic activity. The metabolic activity was quantitatively evaluated by the Alamar Blue assay, according to the manufacturer's instructions. Briefly, at each pre-selected time point, a 10% (v/v) Alamar Blue solution (Bio-Rad, UK) in culture media was replaced the previous culture media for 3 h in standard culture conditions. After incubation, 100 µL of each sample (N=4) supernatant were collected in triplicate and transferred to a 96-well plate. Background was also included by incubating the Alamar Blue solution in the same conditions but in empty wells. Thereafter, the absorbance was measured using a microplate reader (Synergy HT, Bio-Tek Instruments, USA) at excitation and emission wavelengths of 570 and 600 nm, respectively.

DNA quantification. Cell proliferation was determined by quantifying the total amount of double-stranded DNA (dsDNA) using Quant-iT™ PicoGreen® dsDNA dsDNA Assay Kit (ThermoFisher Scientific), according to the manufacturer's instructions. Briefly, samples were washed with PBS and then incubated with 1 mL of ultra-pure water for 1 h at 37°C. After this, samples were frozen at -80°C and then thawed and sonicated using an ultrasonic processor (VCX-130PB-220, Sonics, USA) for 3 cycles of 5 s, to fully lyse the cells and guarantee that all cell content was released. The fluorescence readings were performed in triplicate for each sample (N=4) in 96-well white plates. The fluorescence was measured using a microplate reader (Synergy

HT) at excitation and emission wavelengths of 485/20 and 528/20 nm, respectively. The DNA concentration for each sample was calculated using a standard calibration curve included in the assay.

Alkaline phosphatase activity. Lysed samples (from DNA quantification) were centrifuged at 13500 rpm for 15 min using a microcentrifuge (ScanSpeed Mini, Labogene, Denmark). ALP activity was determined from the supernatant by measuring the hydrolysis of p-nitrophenylphosphate (pNPP) in the yellow end-product p-nitrophenol by ALP. For this, 100 μL of pNPP (Sigma-Aldrich) and 20 μL of alkaline buffer solution (Sigma-Aldrich) were added to each sample. The reaction was stopped with 100 μL of 0.3 M NaOH (Panreac Quimica, Spain) and absorbance was measured at 405 nm using a microplate reader (Synergy HT). Four samples of each condition were analysed (N=4), and the absorbance readings were performed in duplicate for each sample. The ALP concentration for each sample was calculated from a standard calibration curve included in the assay prepared using a calf intestinal ALP enzyme (1 μmol/min; Promega, USA).

Gene expression. At each time point, the total ribonucleic acid (RNA) from each sample (N=4) was isolated using TriReagent (Sigma-Aldrich), according to the manufacturer's instructions. After determining the purity and concentration of the extracted RNA by Nanodrop spectrophotometer at 260 nm (Thermo Fisher Scientific), complementary DNA was reverse transcribed using qScript cDNA Synthesis Kit (Quanta biosciences, USA). Aliquots of each cDNA sample were frozen until the polymerase chain reactions (PCRs) were carried out. Real-time PCR was performed in a mastercycler (Realplex, Eppendorf, Germany) using PerfeCTa SYBR Green FastMix (Quanta Biosciences). The amplification program consisted of a pre-incubation step for denaturation of the template cDNA (2 min, 95°C), followed by 40 cycles of denaturation (5 s, 95°C), an annealing step (15 s, 60°C), and an extension step (20 s, 72°C). Glyceraldehyde-3-phosphate dehydrogenase (GAPDH) and β-actin were used as reference genes. All samples were normalized by the geometric mean of the expression levels of reference genes, and fold changes were related to the control groups using the ΔΔCt method, where Ct is the crossing point of the reaction amplification curves determined by the Realplex 2.2 software (Eppendorf).

Immunostaining. Samples were fixed in freeze-cold 100% methanol (Honeywell, USA) for 20 min at 4°C and then washed thoroughly with PBS. Cells were permeabilised with 0.1% (v/v) Triton X-100 (Sigma-Aldrich) for 20 min at RT under gentle agitation. Then, samples were rinsed

with PBS and blocked with 2% (w/v) bovine serum albumin (BSA) in PBS for 1 h at RT. Thereafter, samples were incubated with a primary antibody against osteopontin (OPN; rabbit anti-OPN antibody, 1:1000, ab8448, Abcam, UK) in 0.1% (w/v) BSA in PBS, overnight at 4°C under gentle agitation. After removing the antibody solution, samples were washed 3 times with PBS for 15 min. Thereafter, the samples were incubated with the corresponding secondary antibody labelled with AlexaFluor 488 (donkey anti-rabbit IgG (H+L), 1:200, A21206, ThermoFisher Scientific), for 2 h at RT protected from light under mild agitation. Finally, once the samples were washed with PBS, nuclei, and cytoskeleton were stained with DAPI (1:1000 in PBS, Sigma-Aldrich) and phalloidin-TRITC (1:200 in PBS, Sigma-Aldrich), respectively, at RT for 1 h. After a final washing, samples were visualized using a confocal laser scanning microscope (TCS SP8). Each experiment was performed in duplicate.

Histology. Samples were washed with PBS and fixed in 10% formalin (Thermo Fisher Scientific) for 30 min at RT. Then, samples were embedded in Histogel specimen processing gel (Thermo Fisher Scientific), dehydrated through graded ethanol solutions, and embedded in paraffin for further sectioning using a microtome (HM355S, Microm, Thermo Scientific). Sections of 10 μm thickness were prepared and stained with Masson´s Trichrome. Sections were observed under a transmitted light microscope (Zeiss, Germany).

2.3.5. Statistical Analysis

The statistical analysis was conducted with GraphPad Prism version 9.0 (GraphPad Software Inc., San Diego, USA) using one-way analyses of variance (ANOVA) followed by Tukey post hoc test, or a two-way ANOVA with Bonferroni post-test, to study the influence of two categorical independent variables. The values were considered different for a level of significance of $p<0.05$. Statistically significant values are annotated in their respective graphs and the data is represented by mean ± standard deviation.

2.4. Results and Discussion

2.4.1. Bioinspired mineralization of CNCs

Nanocellulose materials have been considered a natural source for revolutionary applications in materials science [37]. Leveraging on the surface chemistry and high strength of CNCs, we used them as crosslinkers after functionalization with aldehyde groups or as biofunctional nanofillers after promoting mineralization on their surface, in order to improve the mechanical strength and biofunctionality of the scaffolds for bone TERM applications.

We produced CNCs by the typical sulfuric acid hydrolysis of microcrystalline cellulose derived from wood pulp [27], [28]. The produced CNCs exhibited the characteristic rod-shaped morphology with length of 100-200 nm and height of 2-6 nm in agreement with previous works [24], [28]. During its production, CNCs are simultaneously grafted with anionic sulfate half-ester groups on their surface, which results in 225 ± 10 mmol/kg of surface sulfonate groups ($=SO_3^-$). These results are in agreement with those reported for CNCs isolated from different cellulose sources by sulfuric acid hydrolysis that typically contain 80-350 mmol/kg of anionic sulfate half-esters introduced at some of the surface hydroxyl groups [28], [38].

In native bone tissue, the precipitation of calcium and phosphate ions to form hydroxyapatite (Hap) is regulated by anionic NCPs, which are supposed to act as nucleation inhibitors by stabilizing its amorphous calcium phosphates precursors [6]. Bioinspired by this nanoscale mineralization process, we incubated CNCs with a simplified SBF (s-SBF) solution without Mg^{2+}, HCO_3^-, and SO_4^{2-} to effectively precipitate Hap precursors on their surface and prevent other undesired precipitation products. During this process, calcium divalent cations (Ca^{2+}) and phosphate ions from the supersaturated s-SBF are combined with the sulfonic and hydroxyl groups on the surface of CNCs via hydrogen and ionic bonding, to form a stable mineralization droplet that further grows into the crystal grain of Hap [39]–[41]. Consequently, variations of pH and [Ca^{2+}/SO_3^-] ratios alter the relative concentrations of the protonated forms of phosphate ion ($H_2PO_4^-$, pH < 7 or $HPO4^{2-}$ and PO_4^{3-}, pH > 7) and thus the chemical composition, the amount, and solubility of the apatite that is being formed [42]–[44]. Therefore, we screened different mineral formation conditions, varying the pH of s-SBF solution (6.9 or 7.9) and the ratio between calcium ions [Ca^{2+}] and CNCs surface functional groups [$=SO_3^-$] (molar ratio = 20 or 40).

Scanning electron microscopy (SEM) images of non-mineralized controls (figure III.1a) showed a visible distinction from mineralized samples obtained with a Ca^{2+}/SO_3^- ratio = 20 (figure III.1b-c), pointing to the presence of mineral nanosized structures on CNCs' surface. Moreover, SEM images also showed that detached nanoparticles were formed when the Ca^{2+}/SO_3^- ratio = 40 (figure S.2, Supporting Information). As the [Ca^{2+}/SO_3^-] ratio raises from 20 to 40, more calcium and phosphate ions are available in the s-SBF solution rather than CNCs sulfonic groups which leads to the formation of more Hap but that is not linked to the nanoparticles. In this sense, it is crucial to establish the right balance between Ca^{2+}/SO_3^- so Hap could be effectively deposited on the surface of CNCs rather than be formed spontaneously away from their surface. These results

indicated that significant Hap coating is likely to occur at higher adding amounts of CNCs (i.e., low calcium ion and sulfonic group molar ratios) [31], [45]. We therefore infer that at [Ca^{2+}/SO_3^-] ratio = 20 the interactions between the mineral ions in s-SBF and the chemical groups on the surface CNCs reach their optimal stage, as previously suggested using amorphous calcium carbonate nanoparticles [46]. Thus, CNCs mineralized at Ca^{2+}/SO_3^- ratio = 20 produced from 6.9 and 7.9 pH of s-SBF were selected for further analysis and later incorporation into the cryogel scaffolds.

Furthermore, we also found that the pH of s-SBF solution influenced the formation of these nanostructures (figure III.1b-c and figure S.2, Supporting Information). In basic conditions (pH 7.9), the formation of nanosized structures is higher than in slightly acidic conditions (pH 6.9) (figure III.1b-c). This can be explained by the presence of a more reactive and less protonated form of phosphate ion ($HPO4^{2-}$ and PO_4^{3-}, pH > 7) that reacts with the calcium that is linked to the sulfonic groups of CNCs in a greater proportion and rate, forming increased amounts of Hap [42]–[44]. These results agree with the quantification of mineral content using thermogravimetric analysis (TGA), as depicted figure III.1 d. The results showed that mineral content as well as their tendency to aggregate is higher when pH increased (figure III.1 b-c) [31], [45].

Energy dispersive spectroscopy (EDS) profiling was used to determine the Ca/P ratio of the nanostructures formed on the surface of mineralized CNCs (m-CNCs) (figure III.1 e). m-CNCs produced with a ratio (Ca^{2+}/SO_3^-) = 20 and at pH 6.9 and 7.9, showed Ca/P ratio of 1.85 and 1.7, respectively. These results are consistent with the literature that reports values close to ratio 1.67 for Hap and native human bone [39], [40], [47], suggesting that the nanostructures formed on the surface of m-CNCs are nanosized Hap. The slightly higher Ca/P ratios found on our samples can probably be related with the formation of some other calcium minerals as calcium carbonate or calcium hydroxide during the mineralization process [45]. We further characterized the chemical composition of our samples using Fourier transform infrared spectroscopy (FTIR) (figure III.1 f). The FTIR spectral data of the samples after the mineralization protocol showed the typical peaks of CNCs (Figure S.3, Supporting Information) [48], [49]. Thus, CNCs reference spectrum was subtracted to each sample spectra to better visualize Hap functional groups signals. As shown in the FTIR spectra (figure III.1 f), the signals at 559 and 599, and 1020 cm^{-1} are associated to the vibration, bending, and stretching modes of PO_4^{3-} in Hap [50], [51]. In addition, a signal at 632 cm^{-1}, which is assigned to the bending mode of hydroxyl groups in pure Hap [52] could be also

observed. All of these signals can also be seen in FTIR spectra of native bone [5]. These results suggest the presence of Hap around the CNCs.

Next, we evaluated the crystallinity of the nanocomposites by X-ray diffraction analysis (XRD) (Figure III.1 g). The characteristic peaks of cellulose at 2θ = 16° and 22.5° were assigned to the typical planes (110) and (200) of cellulose, respectively [39], [40]. After the mineralization protocol, the samples produced at pH 6.9 exhibited the known peaks of Hap at 2θ = 26.0° (002), 32.1° (211), 34.3° (202) and 39.7° (310), 46.7° (222), while the samples produced at pH 7.9 also showed a peak at 49.7° (213) [40], [45]. These results corroborate FTIR data and confirm that after the mineralization protocol, m-CNCs samples contain Hap. More importantly, we could also observe that depending on the pH of the mineralization solution m-CNCs exhibited more amorphous or more crystalline structures. The mineralization protocol at pH 7.9 resulted in m-CNCs exhibiting more characteristic and higher intensity peaks typical of hexagonal crystal form of Hap than the protocol at pH 6.9. Moreover, the peaks corresponding to Hap of m-CNCs samples produced at pH 7.9 were higher than those corresponding to the background cellulose, indicating that more Hap was successfully formed on the CNCs showing a more crystalline structure compared to a more amorphous structure obtained with the pH 6.9 protocol.

We also determined the surface charge of the different nanoparticles (figure III.1h). The results show that both amorphous and crystalline m-CNCs have a comparable net negative surface (-24.0±0.6 and -23.3±0.4 mV, respectively) but significantly less negative than pristine CNCs (-63.3±0.3 mV). These results are specially interesting considering the role of NCPs not only as regulators of the sequestration of mineral ions, but also as key players in the formation of negatively charged complexes of mineral precursors that enter into collagen through electrostatic attraction and promote intrafibrillar collagen mineralization [6]. Overall, these results indicate that the bioinspired mineralization protocol of CNCs results in Hap formation with amorphous and crystalline structures, depending on the pH of the precursor solution.

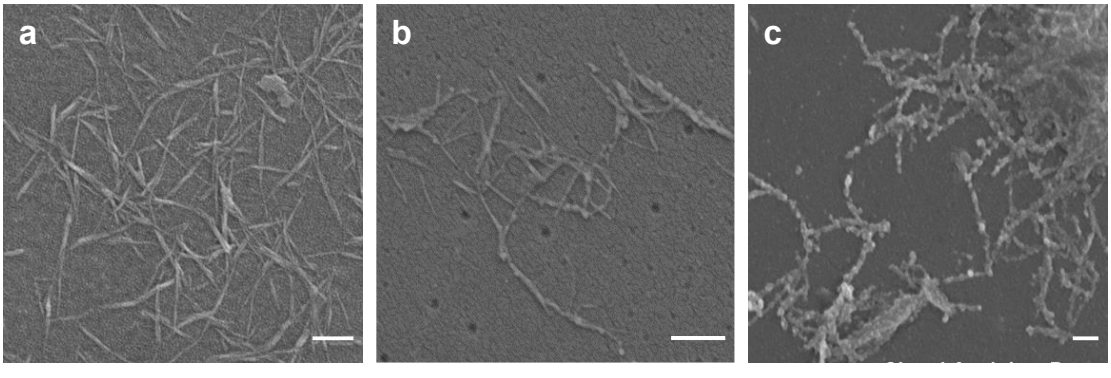

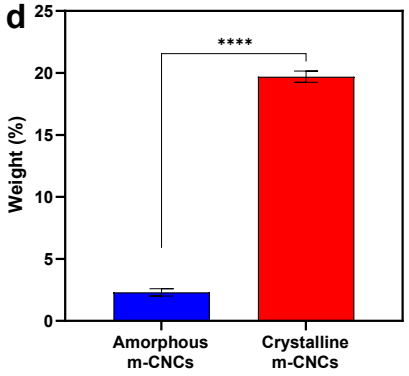

e

EDS			
Element	Content (wt%)		
	CNCs	Amorphous	Crystalline
C	46.2	46.5	33.6
O	53.4	48.4	44.7
Ca	-	2.4	12.4
P	-	1.3	7
Ca/P ratio	-	1.85	1.77

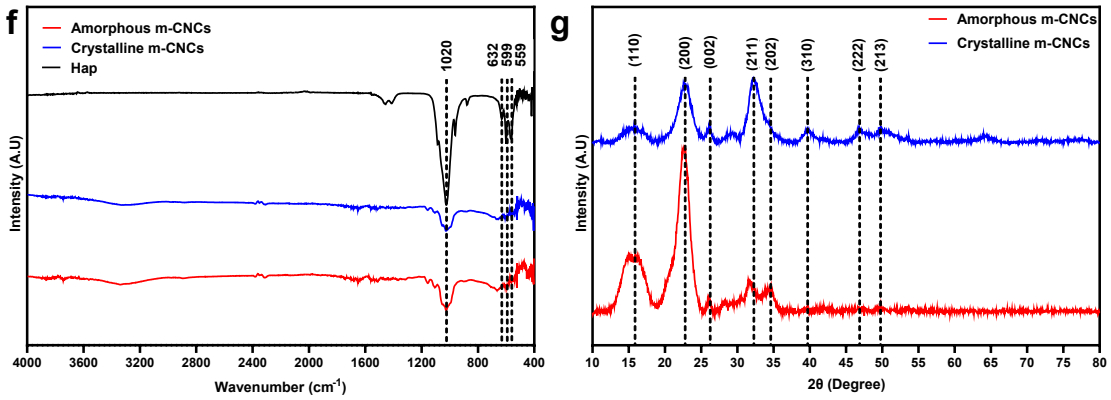

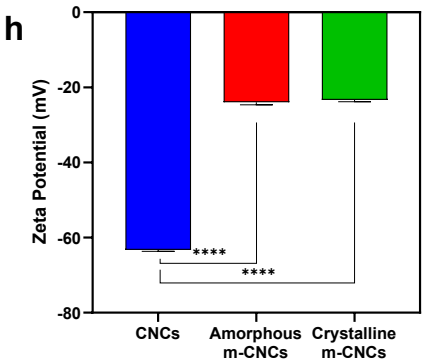

Figure III.1: Nanostructure, composition, and characterization of the biomineralized CNCs (m-CNCs). SEM images of **(a)** non-mineralized CNCs, **(b)** amorphous m-CNCs (pH 6.9), and **(c)** crystalline m-CNCs (pH 7.9). Scale bar: 100 nm; **(d)** TGA analysis of the m-CNCs; **(e)** EDS data of non-mineralized and mineralized CNCs confirmed the presence of Ca and P; **(f)** FTIR spectra of nano-Hap and m-CNCs nanocomposites after subtraction of the CNCs spectra; **(g)** XRD analysis of the amorphous and crystalline m-CNCs. Cellulose and nano-Hap were used as references;

2.4.2. Organic-inorganic cryogel scaffolds production and physical characterization

Collagen is the main organic component of bone, which has frequently inspired bioengineers to produce different types of hydrogels and scaffolds for bone TERM applications [1]. Nevertheless, the use of collagen has a number of shortcomings mainly related to its xenogenic origin and batch-to-batch variability [1]. Bioinspired by the role of platelets in tissues healing microenvironment, we previously reported bioactive cryogel scaffolds consisting of PL reinforced and crosslinked with a-CNCs that exhibit an elastic interconnected porous network [25]. During gelation at sub-zero temperatures, the aqueous component freezes and forms ice crystals that act as pore-forming agents, which exclude the solute (i.e., PL proteins, a-CNCs, and m-CNCs) from the ice lattice, compacting the pore walls between the growing ice crystals [53]. Thus, we hypothesized that the incorporation of m-CNCs in these scaffolds would mimic the intrafibrillar nanoscale biomineralization environment and promote osteogenic differentiation of stem cells.

Firstly, we tested the amount of m-CNCs that could be incorporated in the PL-based cryogel scaffolds without compromising their stability. For this, different proportions of a-CNCs (0-2.4 wt.%) and m-CNCs (0-2.4 wt.%) were mixed with PL (maintaining the total concentration of nanoparticles of 2.4 wt.%), and samples were immersed in PBS. The cryogel scaffolds with m-CNCs content higher than 75% of total nanoparticles showed fast solubilization, losing the pre-formed 3D structure. On the other hand, the other mineralized formulations (50%-High and 25%-Low of m-CNCs) maintained their structure and showed a high mould fidelity, comparable to the non-mineralized cryogel scaffolds. From these findings we could infer that the presence of a-CNCs is crucial for the structural integrity of the cryogel scaffolds due to the chemical covalent crosslinking between a-CNCs and the amine groups of PL proteins through reversible Schiff base bonds [26], [30].

We further characterized the structural integrity of our mineralized cryogel scaffolds by measuring the weight loss of the samples immersed in PBS for 21 days (Figure III.2 a). All formulations lost weight over time, though cryogel scaffolds with high amount of both amorphous and crystalline m-CNCs showed sligthly higher weight loss (47.9±4.4% and 39.9±6.1%, respectively) in comparison with the formulations containing low amount of m-CNCs (32.1±7.3% for the amorphous condition and 35.4±4.2% for the crystalline) and the control group (25.3±2.0%). As previously anticipated, the formulations with high m-CNCs content decreased the crosslinking

degree between the a-CNCs and amine groups of PL-derived proteins, which was not sufficient to jeopardize the initial and long-term structural integrity of the mineralized cryogel scaffolds.

Moreover, liquid adsorption, as water, blood, and other body fluids, is key for the proper function of the bone tissue, as the remaining tissues of the body, and more important in case of injury or regeneration [54]–[56]. Therefore, the water uptake ability of the cryogels was evaluated. Cryogels scaffolds without m-CNCs (control group), exhibited higher water uptake capability compared to the crystalline formulations and comparable to the amorphous formulations (Figure III.2 b). Regarding the amorphous and crystalline mineralized cryogel scaffold formulations, there are no significant differences between them.

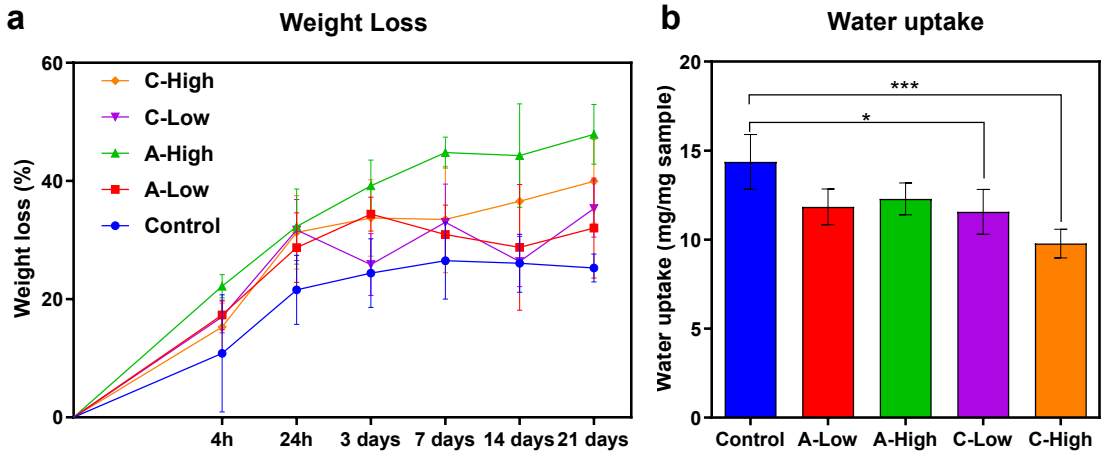

Figure III.2: Physical properties of the cryogel scaffolds. (a) Weight loss of the cryogel scaffolds over 21 days in PBS; **(b)** Water uptake was determined after 30 s immersion in PBS. Statistical significance: *P < 0.1, ***P < 0.001.

2.4.3. Biomimetic mineralization stimulates osteogenic differentiation

First, we evaluated whether the mineralized nanocomposite cryogel scaffolds could lead to reduced cell viability. For this, the viability of human adipose-derived stem cells (hASCs) seeded onto the cryogels was evaluated by live/dead staining (figure III.3 a-e). Three days after seeding, results showed a high cell viability (>90%) for all formulations without significant differences between them (figure III.3 f). Moreover, hASCs displayed a spindle-shape morphology and were distributed over the entire cryogel scaffold network, mostly due to the structural integrity of the scaffolds but also probably related with the presence of cell-adhesive proteins (e.g. fibrinogen, fibronectin, vitronectin) in PL [57]–[59] that support hASCs attachment. These results demonstrate that the designed nanocomposite scaffolds are not cytotoxic and that they are suitable for cellular growth support.

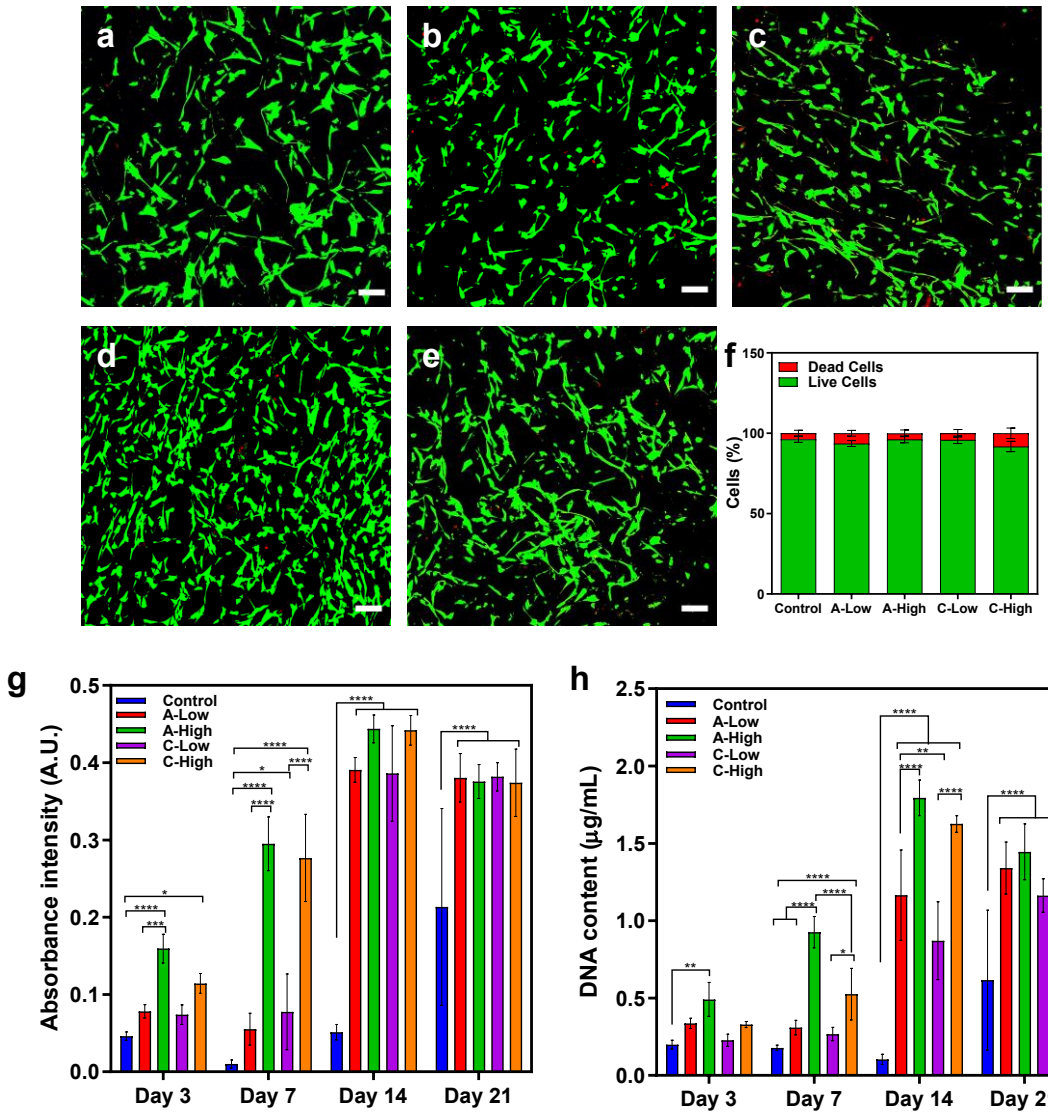

Figure III.3: In vitro evaluation of the cytocompatibility of the cryogel scaffolds. Representative images after live/dead staining (green: live cells; red: dead cells) of hASCs seeded on cryogel scaffolds after 3 days in culture: **(a)** control, **(b)** A-Low, **(c)** A-High, **(d)** C-Low, and **(e)** C-High. Scale bar: 100 µm; **(f)** Respective cell viability quantification. All groups showed more than 90% cell viability after 3 days of culture; **(g)** Metabolic activity and **(h)** DNA content of hASCs seeded on the scaffolds. Statistical significance: *P < 0.1, **P < 0.01, ***P < 0.001, and ****P

We then evaluated if the mineralized cryogel scaffolds could influence the generation of intracellular stress and the proliferation of hASCs. For that, the metabolic activity (figure III.3 g) and cell proliferation measured by DNA quantification (figure III.3 h) were evaluated over cell culture time. All formulations containing m-CNCs nanoparticles presented higher metabolic activity and cell proliferation than the control scaffolds at each time point. Moreover, no significant differences in these parameters were observed between formulations containing the same amount of amorphous and crystalline m-CNCs. Nevertheless, A-High and C-High formulations presented

increased metabolic activity and cell proliferation compared to A-Low and C-Low, respectively, until day 14 of culture. After 21 days, although the values for both indicators are comparable for all mineralized groups, DNA content increased in A-Low and C-Low formulations, while it decreased in A-High and C-High formulations compared to the previous time point, which can be potentially related to lineage commitment of cells or growth diminishment due to cell-cell contact In addition, A-High condition presented a higher value of metabolic activity and DNA content than the crystalline one, which can be possibly justified by the faster passive solubilization of amorphous calcium phosphates minerals [60]–[62]. This leads to an increased concentration of extracellular calcium and phosphate ions, which has been shown to promote osteoblasts proliferation, differentiation, and ECM mineralization by directly activating intracellular mechanisms that influence Ca-sensing receptors in osteoblastic cells [61]–[63].

It is well conceived that cells sense and respond to the biochemical and biophysical properties of the extracellular microenvironment in which they are embedded [64], [65]. To exclusively evaluate the effect of the incorporation of m-CNCs in the cryogel scaffolds on the potential osteogenic commitment of hASCs, cells were cultured in basal media (without the aid of any osteogenic supplement). The activity of alkaline phosphatase (ALP), the hallmark of functional bone, was used to determine the potential of the scaffolds to promote osteogenic differentiation of hASCs [66]. Scaffold formulations including m-CNCs showed higher ALP activity than the control group at all time points (Figure III.4 a). Moreover, ALP activity increased faster and reached higher levels on A-High and C-High formulations than on their respective Low conditions. Interestingly, we also observed that A-High induces maximum ALP activity as soon as day 7, which progressively decreases until the end of culture time, while the other mineralized formulations reach their maximum ALP activity at day 14. Since ALP is an early osteogenic differentiation marker, this demonstrates that the number of m-CNCs nanoparticles, particularly the amount Hap present, influences the rate of cells commitment towards the osteogenic lineage. This faster expression of ALP is most likely corroborated by the literature theory for the intrafibrillar nanoscale biomineralization [5], [6]. Considering that the precursors of the intrafibrillar Hap are amorphous calcium phosphates (ACPs) sequestered by NCPs, such as osteopontin, which inhibit the nucleation of Hap and consequently the extrafibrillar deposition of Hap, amorphous formulations are the ones that resemble the most the microenvironment of the nanoscale biomineralization due to the m-CNCs amorphous structure [5], [6]. In addition, the presence of an amorphous type of nano-Hap on the surface on CNCs as well as the negative charge presented by m-CNCs, besides

mimicking the ACPs and the role of NCPs in native bone, respectively, can act itself as a osteogenic supplement [67], inducing the osteogenic differentiation of seeded stem cells.

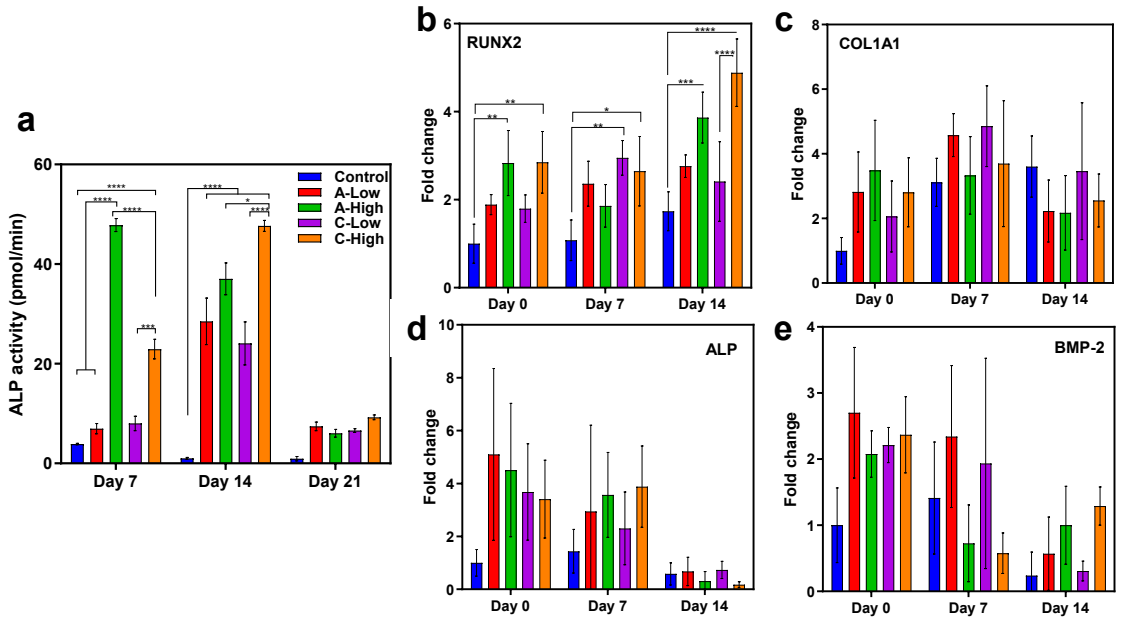

Figure III.4: In vitro evaluation of the ALP activity and gene expression of the cryogel scaffolds. (a) ALP activity of hASCs seeded on the scaffolds. Gene expression of **(b)** RUNX2, **(c)** COL1A1, **(d)** ALP, and **(e)** BMP-2 of hASCs seeded on the scaffolds. Statistical significance: *P < 0.1, **P < 0.01, ***P < 0.001, and ****P < 0.0001.

Furthermore, the transcription levels of genes associated with either osteoblastic/pre-osteocytic differentiation or bone metabolism and remodelling were also evaluated. The expression of RUNX2, a transcription factor involved in early osteogenic lineage commitment [68], was significantly upregulated on both A-High and C-High formulations, compared to control group (Figure III.4 b). In addition, significant differences can be observed among the crystalline conditions after 14 days of culture. Additionally, it is known that, during osteoblast differentiation, RUNX2 up-regulates the expression of bone matrix proteins genes, including COL1A1 [68]. This fact can be seen in our data since the up-regulation of RUNX2 is followed by an increased expression of COL1A1, although no significant differences are notorious (Figure III.4 c). Therefore, the incorporation of the m-CNCs improved the expression of RUNX2 by hASCs and subsequently enhanced the expression of COL1A1 as well, demonstrating the osteoinductive potential of the developed cryogels. Moreover, the expression levels of ALP, an early-stage marker for osteoblastic differentiation, had higher expression from the beginning (day o) until day 7 whereas by day 14 a marked decrease is observed. This diminish gene expression can be explained by the higher ALP

activity by hASCs on this day, which is corroborated by the ALP activity data. Other precursor that is involved in the osteogenic differentiation process is BMP-2, which plays an active role on inducing the osteogenic differentiation of immature osteoblasts as well as enhancing the ALP activity of cells [69]. Curiously, by day 7 both high content conditions cells down-regulate their BMP-2 expression and up-regulate their ALP activity, as expected [69]. Analogous behaviour is apparent after two weeks of culture, where cells from all decrease their BMP-2 gene expression and significantly increase their ALP activity.

Additionally, the expression of OPN was evaluated after 21 days of culture by immunostaining. OPN is abundantly secreted by MSCs and can be further upregulated during their osteogenic differentiation [70]. As expected, enhanced expression of this osteogenic marker was accomplished by mineralized cryogels compared to the control formulation (Figure III.5a-e). Additionally, the High formulations presented higher OPN expression rather than their Low homologues, which reveals the importance of the presence and amount of mineralized CNCs on the expression of this marker and in the osteogenic potential of the developed cryogels. This may be achieved by the presence of higher amounts of calcium and phosphate ions resulting from the ALP activity or solubilization of the Hap present in the nanocomposites. Since OPN is a calcium-binding protein, high levels of this marker are associated with the ECM mineralization process during the late osteogenic differentiation of osteoprogenitor cells [71]. Moreover, OPN is thought to have a multifunctional role in directing the intrafibrillar biomineralization of collagen and activation of osteoclasts, even though OPN is generally considered a mineralization inhibitor [72], [73]. These results confirm the osteoinductive, osteoconductive, and osteogenic properties of the PL-mCNCs scaffolds, presenting the capability to promote osteogenic differentiation of encapsulated hASCs without osteogenic supplements.

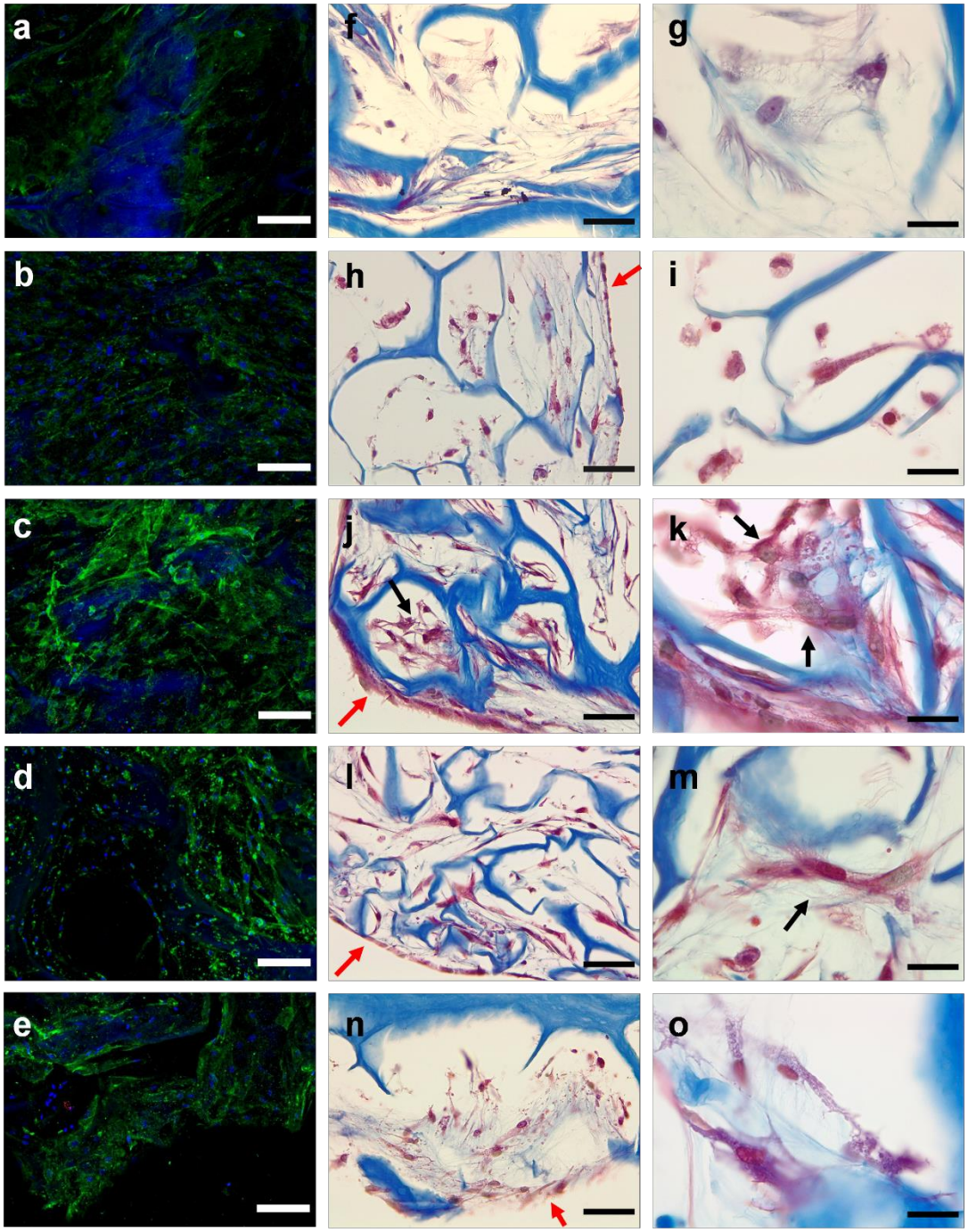

Figure III.5: Evaluation of the osteogenic commitment of hASCs seeded on the cryogel scaffolds. Representative immunocytochemistry images of the **(a)** control, **(b)** A-Low, **(c)** A-High, **(d)** C-Low and **(e)** C-High scaffolds seeded with hASCs after 21 days of culture (nuclei in blue, cytoplasm in red, and OPN in green). Scale bar: 100 μm; Immunohistochemical representative Masson´s Trichrome images of the **(f, g)** control, **(h, i)** A-Low, **(j, k)** A-High, **(l, m)** C-Low, and **(n, o)** C-High cryogels seeded with hASCs after 21 days of culture. An osteoblastic-like layer is apparent on the mineralized cryogels (red arrow) while some cells present an osteocyte-like phenotype (black arrows)**.** Scale bar: 50 μm **(f, h, j, l, and m)** and 20 μm **(g, l, k, m, and o)**.

In native bone, osteoblasts experience different morphological conformations as the surrounding matrix is transformed from a soft osteoid to a more mineralized matrix [74]. In this sense, after 21 days of culture, the samples were recovered for histological evaluation to the study hASCs morphology as well as ECM deposition (figure III.5 f-o). Regarding the control (figure III.5 f, g), it appears that more reticular connective tissue, associated to collagen deposition, is being produced by hASCs, without osteogenic commitment. All mineralized formulations showed a thin (A-Low [figure III.5 h, i] and C-High [figure III.5 n, o]) or thicker (A-High [figure III.5 j, k] and C-Low [figure III.5 l, m]) layer of cells surrounding the biomaterial (red arrows in figure III.5). Moreover, both A-High and C-Low conditions (figure III.5 j, k and l, m, respectively) showed cells with an osteocyte-like phenotype (star shape, black arrow in figure III.5) with several cellular projections between them. Moreover, the A-High formulation presented an enhanced expression of osteogenic-related markers, which suggests that it emulates better the nanoscale biomineralization process where ACP is firstly deposited and is later matured into Hap crystals [5], [6], and the faster solubilization of the amorphous Hap [60], releasing calcium ions, could also improve the osteoinduction of the biomaterial.

In the attempt of proving that the osteogenic potential of the mineralized cryogels scaffolds could be achieved with other type of cells rather than hASCs, we also used human dental pulp-derived cells (hDPCs), which have potential to differentiate into mineralizing cells (odontoblasts and osteoblasts) [75]. Similar to the results obtained with hASCs, formulations containing m-CNCs presented higher metabolic activity and cell proliferation rates than the control scaffolds at early time points although these differences between groups were smaller at later stages. It is worth mentioning that A-High formulation presented a significantly higher value for both metabolic activity and cell proliferation, which is also observed in the hASCs results (Figure III.3). Regarding the ALP activity, we expected that the mineralized cryogel scaffolds induced higher enzymatic activity than non-mineralized controls. However, comparable, or lower ALP activity than the control group was observed for the mineralized cryogel scaffold formulations after 14 and 21 days (figure III.6 c). Nonetheless, while on mineralized samples ALP activity peaked at day 14 and then decreased at day 21, which is especially evident in both A- and C-High formulations, it peaked at day 21 in non-mineralized control samples. Since ALP is considered an early mineralization marker, these results

might be related to a faster osteogenic differentiation of hDPCs in mineralized than in control samples.

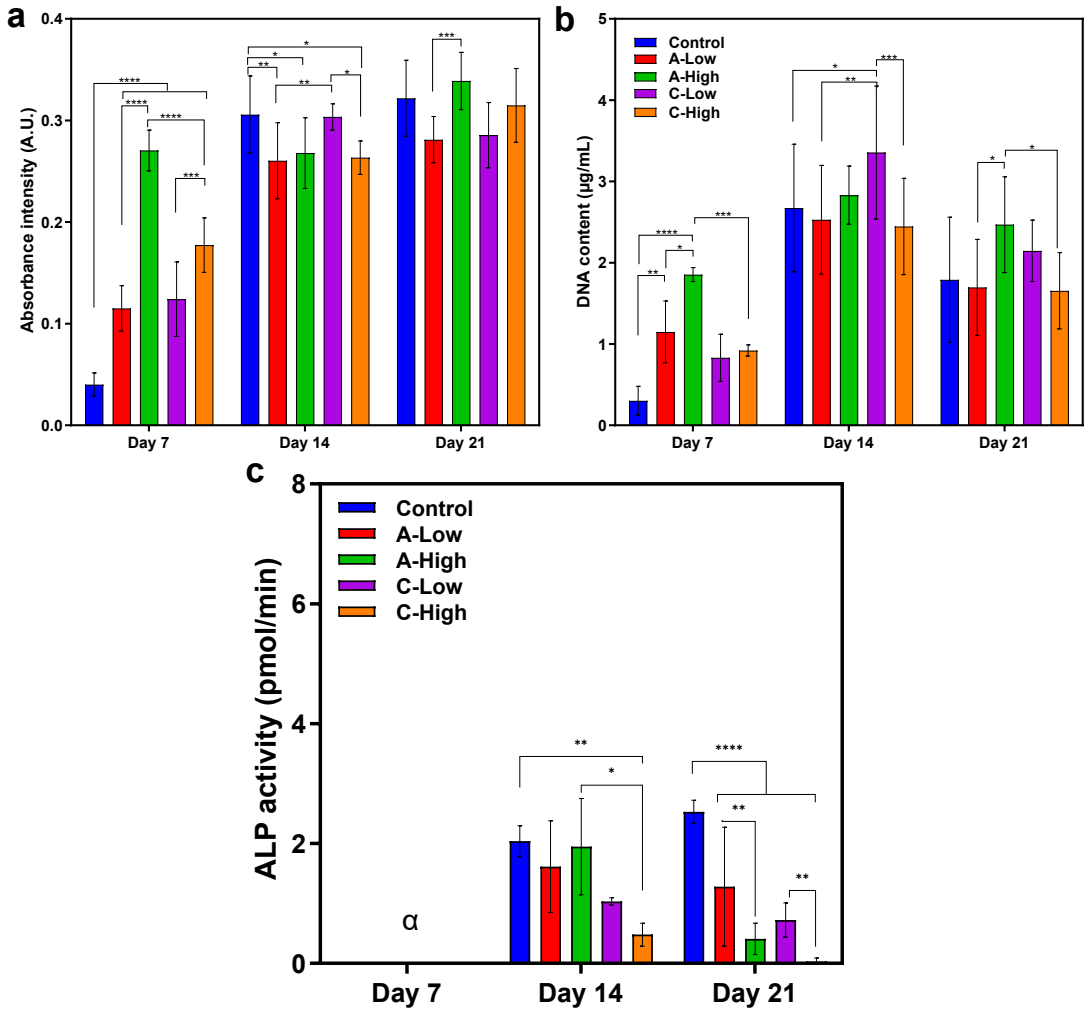

Figure III.6: In vitro osteogenic commitment of hDPCs on the cryogel scaffolds. (a) Metabolic activity, **(b)** DNA content**,** and **(c)** ALP activity of hDPCs seeded on the scaffolds. Statistical significance: *P < 0.1, **P < 0.01, ***P < 0.001, and ****P < 0.0001.

2.5. Conclusions

Herein, we developed a bioinspired scaffold that emulates the nanoscale biomineralization microenvironment in vitro. PL served as the cryogel scaffold-based material, incorporating crosslinkers and nanofillers, as a-CNCs and m-CNCs to provide enhanced functionalities. We found that the developed cryogels enhanced the metabolic activity, cell proliferation, and ALP activity of hASCs and hDPCs. Moreover, they also up-regulated the expression of bone-related markers, as RUNX2, BMP-2, ALP, OPN, and COL1A1 of hASCs. These results indicated a preferential differentiation of hASCs and hDPCs towards osteogenic lineages. Overall, results suggest that the incorporation of m-CNCs improved the biological performance of the developed cryogels by

ameliorating their osteoinductive properties. In summary, the proposed PL-m-CNCs cryogel scaffolds could be potentially useful for tissue engineering and regenerative medicine strategies due to their ability to mimic the nanoscale mineralization process and microenvironment.

2.6. Acknowledgements

We acknowledge the financial support from Research Council of Norway for project no. 287953 and from Portuguese Foundation for Science and Technology (FCT) for CEECIND/01375/2017 to MGF.

2.7. References

[1] N. Reznikov, J. A. M. Steele, P. Fratzl, and M. M. Stevens, "A materials science vision of extracellular matrix mineralization," *Nature Reviews Materials*, vol. 1, no. 8. Nature Publishing Group, pp. 1–14, Jun. 14, 2016, doi: 10.1038/natrevmats.2016.41.

[2] A. L. Boskey and P. G. Robey, "The Composition of Bone," in *Primer on the Metabolic Bone Diseases and Disorders of Mineral Metabolism: Eighth Edition*, Wiley Blackwell, 2013, pp. 49–58.

[3] F. Nudelman *et al.*, "The role of collagen in bone apatite formation in the presence of hydroxyapatite nucleation inhibitors," *Nat. Mater.*, vol. 9, no. 12, pp. 1004–1009, 2010, doi: 10.1038/nmat2875.

[4] G. S. Kumar, *Orban's oral histology and embryology*, 14th ed. Elsevier, 2015.

[5] G. Thrivikraman *et al.*, "Rapid fabrication of vascularized and innervated cell-laden bone models with biomimetic intrafibrillar collagen mineralization," *Nat. Commun.*, vol. 10, no. 1, 2019, doi: 10.1038/s41467-019-11455-8.

[6] L. Yu and M. Wei, "Biomineralization of Collagen-Based Materials for Hard Tissue Repair," *Int. J. Mol. Sci. 2021, Vol. 22, Page 944*, vol. 22, no. 2, p. 944, Jan. 2021, doi: 10.3390/IJMS22020944.

[7] D. A. Chaukar *et al.*, "Quality of life in head and neck cancer survivors: a cross-sectional survey," *Am. J. Otolaryngol.*, vol. 30, no. 3, pp. 176–180, May 2009, doi: 10.1016/j.amjoto.2008.05.001.

[8] T. Burk, J. Del Valle, R. A. Finn, and C. Phillips, "Maximum Quantity of Bone Available for Harvest From the Anterior Iliac Crest, Posterior Iliac Crest, and Proximal Tibia Using a

Standardized Surgical Approach: A Cadaveric Study," *J. Oral Maxillofac. Surg.*, vol. 74, no. 12, pp. 2532–2548, 2016, doi: 10.1016/j.joms.2016.06.191.

[9] T. M. Osborn, D. Helal, and P. Mehra, "Iliac crest bone grafting for mandibular reconstruction: 10-year experience outcomes," *J. Oral Biol. Craniofacial Res.*, vol. 8, no. 1, pp. 25–29, 2018, doi: 10.1016/j.jobcr.2017.12.001.

[10] H. M. Hahn, Y. J. Lee, and D. H. Park, "Huge Radicular Cyst of the Maxilla Treated with Complete Resection and Immediate Reconstruction by Rib Bone Graft," *J. Maxillofac. Oral Surg.*, vol. 18, no. 3, pp. 378–381, 2019, doi: 10.1007/s12663-018-1125-0.

[11] E. C. Sung, S. M. Chan, K. Sakurai, and E. Chung, "Osteonecrosis of the maxilla as a complication to chemotherapy: A case report," *Spec. Care Dentist.*, vol. 22, no. 4, pp. 142–146, 2002, doi: 10.1111/j.1754-4505.2002.tb01178.x.

[12] A. Memic *et al.*, "Latest Advances in Cryogel Technology for Biomedical Applications," *Adv. Ther.*, vol. 2, no. 4, p. 1800114, 2019, doi: 10.1002/adtp.201800114.

[13] G. L. Koons, M. Diba, and A. G. Mikos, "Materials design for bone-tissue engineering," *Nat. Rev. Mater. 2020 58*, vol. 5, no. 8, pp. 584–603, Jun. 2020, doi: 10.1038/s41578-020-0204-2.

[14] L. N. Melek, "Tissue engineering in oral and maxillofacial reconstruction," *Tanta Dent. J.*, vol. 12, no. 3, pp. 211–223, 2015, doi: 10.1016/j.tdj.2015.05.003.

[15] R. Rai, R. Raval, R. V. S. Khandeparker, S. K. Chidrawar, A. A. Khan, and M. S. Ganpat, "Tissue Engineering: Step Ahead in Maxillofacial Reconstruction.," *J. Int. oral Heal. JIOH*, vol. 7, no. 9, pp. 138–42, 2015, [Online]. Available: http://www.ncbi.nlm.nih.gov/pubmed/26435634%0Ahttp://www.pubmedcentral.nih.gov/articlerender.fcgi?artid=PMC4589709.

[16] H. H. K. Xu, M. D. Weir, and C. G. Simon, "Injectable and strong nano-apatite scaffolds for cell/growth factor delivery and bone regeneration," *Dent. Mater.*, vol. 24, no. 9, pp. 1212–1222, Sep. 2008, doi: 10.1016/j.dental.2008.02.001.

[17] A. S. Urkmez, S. G. Clark, M. B. Wheeler, M. S. Goldwasser, and R. D. Jamison, "Evaluation of chitosan/biphasic calcium phosphate scaffolds for maxillofacial bone tissue engineering," *Macromol. Symp.*, vol. 269, no. 1, pp. 100–105, 2008, doi:

10.1002/masy.200850912.

[18] M. D. Weir and H. H. K. Xu, "Culture human mesenchymal stem cells with calcium phosphate cement scaffolds for bone repair," *J. Biomed. Mater. Res. - Part B Appl. Biomater.*, vol. 93, no. 1, pp. 93–105, Apr. 2010, doi: 10.1002/jbm.b.31563.

[19] S. Konopnicki *et al.*, "Tissue-Engineered Bone With 3-Dimensionally Printed β-Tricalcium Phosphate and Polycaprolactone Scaffolds and Early Implantation: An In Vivo Pilot Study in a Porcine Mandible Model," *J. Oral Maxillofac. Surg.*, vol. 73, no. 5, pp. 1016.e1-1016.e11, May 2015, doi: 10.1016/j.joms.2015.01.021.

[20] R. S. Spitzer, C. Perka, K. Lindenhayn, and H. Zippel, "Matrix engineering for osteogenic differentiation of rabbit periosteal cells using α-tricalcium phosphate particles in a three-dimensional fibrin culture," *J. Biomed. Mater. Res.*, vol. 59, no. 4, pp. 690–696, 2002, doi: 10.1002/jbm.1277.

[21] Y. Yamada *et al.*, "Bone regeneration following injection of mesenchymal stem cells and fibrin glue with a biodegradable scaffold," *J. Cranio-Maxillofacial Surg.*, vol. 31, no. 1, pp. 27–33, 2003, doi: 10.1016/S1010-5182(02)00143-9.

[22] R. M. A. Domingues, M. E. Gomes, and R. L. Reis, "The potential of cellulose nanocrystals in tissue engineering strategies," *Biomacromolecules*, vol. 15, no. 7, pp. 2327–2346, 2014, doi: 10.1021/bm500524s.

[23] R. J. Moon, A. Martini, J. Nairn, J. Simonsen, and J. Youngblood, *Cellulose nanomaterials review: Structure, properties and nanocomposites*, vol. 40, no. 7. 2011.

[24] C. R. Silva *et al.*, "Injectable and tunable hyaluronic acid hydrogels releasing chemotactic and angiogenic growth factors for endodontic regeneration," *Acta Biomater.*, vol. 77, pp. 155–171, 2018, doi: 10.1016/j.actbio.2018.07.035.

[25] B. B. Mendes *et al.*, "Intrinsically Bioactive Cryogels Based on Platelet Lysate Nanocomposites for Hemostasis Applications," *Biomacromolecules*, vol. 21, no. 9, pp. 3678–3692, 2020, doi: 10.1021/acs.biomac.0c00787.

[26] B. B. Mendes, M. Gómez-Florit, R. A. Pires, R. M. A. Domingues, R. L. Reis, and M. E. Gomes, "Human-based fibrillar nanocomposite hydrogels as bioinstructive matrices to tune stem cell behavior," *Nanoscale*, vol. 10, no. 36, pp. 17388–17401, Sep. 2018, doi:

10.1039/c8nr04273j.

[27] D. Bondeson, A. Mathew, and K. Oksman, "Optimization of the isolation of nanocrystals from microcrystalline cellulose by acid hydrolysis," *Cellulose*, vol. 13, no. 2, pp. 171–180, 2006, doi: 10.1007/s10570-006-9061-4.

[28] R. M. A. Domingues *et al.*, "Development of Injectable Hyaluronic Acid/Cellulose Nanocrystals Bionanocomposite Hydrogels for Tissue Engineering Applications," *Bioconjug. Chem.*, vol. 26, no. 8, pp. 1571–1581, 2015, doi: 10.1021/acs.bioconjchem.5b00209.

[29] U. J. Kim, S. Kuga, M. Wada, T. Okano, and T. Kondo, "Periodate oxidation of crystalline cellulose," *Biomacromolecules*, vol. 1, no. 3, pp. 488–492, 2000, doi: 10.1021/bm0000337.

[30] R. Dash, M. Foston, and A. J. Ragauskas, "Improving the mechanical and thermal properties of gelatin hydrogels cross-linked by cellulose nanowhiskers," *Carbohydr. Polym.*, vol. 91, no. 2, pp. 638–645, 2013, doi: 10.1016/j.carbpol.2012.08.080.

[31] M. Ishikawa, Y. Oaki, Y. Tanaka, H. Kakisawa, G. Salazar-Alvarez, and H. Imai, "Fabrication of nanocellulose-hydroxyapatite composites and their application as water-resistant transparent coatings," *J. Mater. Chem. B*, vol. 3, no. 28, pp. 5858–5863, 2015, doi: 10.1039/c5tb00927h.

[32] P. P. Carvalho *et al.*, "The Effect of Storage Time on Adipose-Derived Stem Cell Recovery from Human Lipoaspirates," *Cells Tissues Organs*, vol. 194, no. 6, pp. 494–500, Nov. 2011, doi: 10.1159/000324892.

[33] P. A. Zuk *et al.*, "Human adipose tissue is a source of multipotent stem cells," *Mol. Biol. Cell*, vol. 13, no. 12, pp. 4279–4295, Dec. 2002, doi: 10.1091/mbc.E02-02-0105.

[34] L. S. Neves *et al.*, "Injectable Hyaluronic Acid Hydrogels Enriched with Platelet Lysate as a Cryostable Off-the-Shelf System for Cell-Based Therapies," *Regen. Eng. Transl. Med.*, vol. 3, no. 2, pp. 53–69, Jun. 2017, doi: 10.1007/s40883-017-0029-8.

[35] V. E. Santo, M. E. Gomes, J. F. Mano, and R. L. Reis, "Chitosan-chondroitin sulphate nanoparticles for controlled delivery of platelet lysates in bone regenerative medicine," *J. Tissue Eng. Regen. Med.*, vol. 6, no. SUPPL. 3, Dec. 2012, doi: 10.1002/term.1519.

[36] L. D. F. F. Almeida *et al.*, "Hyaluronic acid hydrogels incorporating platelet lysate enhance

human pulp cell proliferation and differentiation," *J. Mater. Sci. Mater. Med.*, vol. 29, no. 6, p. 88, 2018, doi: 10.1007/s10856-018-6088-7.

[37] D. Klemm *et al.*, "Nanocellulose as a natural source for groundbreaking applications in materials science: Today's state," *Mater. Today*, vol. 21, no. 7, pp. 720–748, 2018, doi: 10.1016/j.mattod.2018.02.001.

[38] E. J. Foster *et al.*, *Current characterization methods for cellulose nanomaterials*, vol. 47, no. 8. 2018, pp. 2609–2679.

[39] J. Si, Z. Cui, Q. Wang, Q. Liu, and C. Liu, "Biomimetic composite scaffolds based on mineralization of hydroxyapatite on electrospun poly(ε-caprolactone)/nanocellulose fibers," *Carbohydr. Polym.*, vol. 143, pp. 270–278, Jun. 2016, doi: 10.1016/J.CARBPOL.2016.02.015.

[40] A. Kumar, Y. S. Negi, V. Choudhary, and N. K. Bhardwaj, "Microstructural and mechanical properties of porous biocomposite scaffolds based on polyvinyl alcohol, nano-hydroxyapatite and cellulose nanocrystals," *Cellul. 2014 215*, vol. 21, no. 5, pp. 3409–3426, Jul. 2014, doi: 10.1007/S10570-014-0339-7.

[41] D. Gebauer, A. Völkel, and H. Cölfen, "Stable Prenucleation Calcium Carbonate Clusters," *Science (80-.).*, vol. 322, no. 5909, pp. 1819–1822, Dec. 2008, doi: 10.1126/SCIENCE.1164271.

[42] A. K. Lynn and W. Bonfield, "A Novel Method for the Simultaneous, Titrant-Free Control of pH and Calcium Phosphate Mass Yield," *Acc. Chem. Res.*, vol. 38, no. 3, pp. 202–207, Mar. 2005, doi: 10.1021/AR040234D.

[43] L. Wang and G. H. Nancollas, "Calcium Orthophosphates: Crystallization and Dissolution," *Chem. Rev.*, vol. 108, no. 11, pp. 4628–4669, Nov. 2008, doi: 10.1021/CR0782574.

[44] J. P. Simmer and A. G. Fincham, "Molecular Mechanisms of Dental Enamel Formation:," *http://dx.doi.org/10.1177/10454411950060020701*, vol. 6, no. 2, pp. 84–108, Dec. 2016, doi: 10.1177/10454411950060020701.

[45] C. Huang *et al.*, "Biomimetic composite scaffold from an in situ hydroxyapatite coating on cellulose nanocrystals," *RSC Adv.*, vol. 9, no. 10, pp. 5786–5793, Feb. 2019, doi: 10.1039/c8ra09523j.

[46] D. Gebauer *et al.*, "A transparent hybrid of nanocrystalline cellulose and amorphous calcium carbonate nanoparticles," *Nanoscale*, vol. 3, no. 9, pp. 3563–3566, Sep. 2011, doi: 10.1039/C1NR10681C.

[47] E. P. Erasmus, R. Sule, O. T. Johnson, J. Massera, and I. Sigalas, "In vitro Evaluation of Porous borosilicate, borophosphate and phosphate Bioactive Glasses Scaffolds fabricated using Foaming Agent for Bone Regeneration," *Sci. Reports 2018 81*, vol. 8, no. 1, pp. 1–13, Feb. 2018, doi: 10.1038/s41598-018-22032-2.

[48] M. Fan, D. Dai, and B. Huang, "Fourier Transform Infrared Spectroscopy for Natural Fibres," *Fourier Transform - Mater. Anal.*, May 2012, doi: 10.5772/35482.

[49] D. Ciolacu, F. Ciolacu, and V. I. Popa, "AMORPHOUS CELLULOSE-STRUCTURE AND CHARACTERIZATION," *Cellul. Chem. Technol. Cellul. Chem. Technol*, vol. 45, no. 2, pp. 13–21, 2011.

[50] J. Ryu, S. H. Ku, H. Lee, and C. B. Park, "Mussel-Inspired Polydopamine Coating as a Universal Route to Hydroxyapatite Crystallization," *Adv. Funct. Mater.*, vol. 20, no. 13, pp. 2132–2139, Jul. 2010, doi: 10.1002/ADFM.200902347.

[51] G. Wei, J. Reichert, J. Bossert, and K. D. Jandt, "Novel Biopolymeric Template for the Nucleation and Growth of Hydroxyapatite Crystals Based on Self-Assembled Fibrinogen Fibrils," *Biomacromolecules*, vol. 9, no. 11, pp. 3258–3267, Nov. 2008, doi: 10.1021/BM800824R.

[52] X. Cai, H. Tong, X. Shen, W. Chen, J. Yan, and J. Hu, "Preparation and characterization of homogeneous chitosan–polylactic acid/hydroxyapatite nanocomposite for bone tissue engineering and evaluation of its mechanical properties," *Acta Biomater.*, vol. 5, no. 7, pp. 2693–2703, Sep. 2009, doi: 10.1016/J.ACTBIO.2009.03.005.

[53] V. I. Lozinsky, I. Y. Galaev, F. M. Plieva, I. N. Savina, H. Jungvid, and B. Mattiasson, "Polymeric cryogels as promising materials of biotechnological interest," *Trends Biotechnol.*, vol. 21, no. 10, pp. 445–451, Oct. 2003, doi: 10.1016/J.TIBTECH.2003.08.002.

[54] X. Zhao, B. Guo, H. Wu, Y. Liang, and P. X. Ma, "Injectable antibacterial conductive nanocomposite cryogels with rapid shape recovery for noncompressible hemorrhage and

wound healing," *Nat. Commun. 2018 91*, vol. 9, no. 1, pp. 1–17, Jul. 2018, doi: 10.1038/s41467-018-04998-9.

[55] S. A. Bencherif *et al.*, "Injectable cryogel-based whole-cell cancer vaccines," *Nat. Commun. 2015 61*, vol. 6, no. 1, pp. 1–13, Aug. 2015, doi: 10.1038/ncomms8556.

[56] N. Sultana and T. H. Khan, "Water absorption and diffusion characteristics of nanohydroxyapatite (nHA) and poly(hydroxybutyrate-co-hydroxyvalerate-) based composite tissue engineering scaffolds and nonporous thin films," *J. Nanomater.*, vol. 2013, 2013, doi: 10.1155/2013/479109.

[57] N. Fekete *et al.*, "Platelet lysate from whole blood-derived pooled platelet concentrates and apheresis-derived platelet concentrates for the isolation and expansion of human bone marrow mesenchymal stromal cells: Production process, content and identification of active comp," *Cytotherapy*, vol. 14, no. 5, pp. 540–554, 2012, doi: 10.3109/14653249.2012.655420.

[58] B. B. Mendes, M. Gómez-Florit, P. S. Babo, R. M. Domingues, R. L. Reis, and M. E. Gomes, "Blood derivatives awaken in regenerative medicine strategies to modulate wound healing," *Adv. Drug Deliv. Rev.*, vol. 129, pp. 376–393, Apr. 2018, doi: 10.1016/j.addr.2017.12.018.

[59] P. Babo *et al.*, "Platelet lysate membranes as new autologous templates for tissue engineering applications," *Inflamm. Regen.*, vol. 34, no. 1, pp. 033–044, 2014, doi: 10.2492/inflammregen.34.033.

[60] P. S. P. S. Babo, V. E. V. E. Santo, M. E. M. E. Gomes, and R. L. R. L. Reis, "Development of an Injectable Calcium Phosphate/Hyaluronic Acid Microparticles System for Platelet Lysate Sustained Delivery Aiming Bone Regeneration," *Macromol. Biosci.*, vol. 16, no. 11, pp. 1662–1677, Nov. 2016, doi: 10.1002/mabi.201600141.

[61] A. Hoppe, N. S. Güldal, and A. R. Boccaccini, "A review of the biological response to ionic dissolution products from bioactive glasses and glass-ceramics," *Biomaterials*, vol. 32, no. 11, pp. 2757–2774, Apr. 2011, doi: 10.1016/J.BIOMATERIALS.2011.01.004.

[62] S. Maeno *et al.*, "The effect of calcium ion concentration on osteoblast viability, proliferation and differentiation in monolayer and 3D culture," *Biomaterials*, vol. 26, no. 23, pp. 4847–

4855, Aug. 2005, doi: 10.1016/J.BIOMATERIALS.2005.01.006.

[63] P. J. Marie, "The calcium-sensing receptor in bone cells: A potential therapeutic target in osteoporosis," *Bone*, vol. 46, no. 3, pp. 571–576, Mar. 2010, doi: 10.1016/J.BONE.2009.07.082.

[64] W. T. Hsieh, Y. S. Liu, Y. H. Lee, M. G. Rimando, K. H. Lin, and O. K. Lee, "Matrix dimensionality and stiffness cooperatively regulate osteogenesis of mesenchymal stromal cells," *Acta Biomater.*, vol. 32, pp. 210–222, Mar. 2016, doi: 10.1016/J.ACTBIO.2016.01.010.

[65] M. P. Lutolf, P. M. Gilbert, and H. M. Blau, "Designing materials to direct stem-cell fate," *Nat. 2009 4627272*, vol. 462, no. 7272, pp. 433–441, Nov. 2009, doi: 10.1038/nature08602.

[66] P. Magnusson, L. Larsson, M. Magnusson, M. W. J. Davie, and C. A. Sharp, "Isoforms of bone alkaline phosphatase: Characterization and origin in human trabecular and cortical bone," *J. Bone Miner. Res.*, vol. 14, no. 11, pp. 1926–1933, Nov. 1999, doi: 10.1359/jbmr.1999.14.11.1926.

[67] F. Viti, M. Landini, A. Mezzelani, L. Petecchia, L. Milanesi, and S. Scaglione, "Osteogenic Differentiation of MSC through Calcium Signaling Activation: Transcriptomics and Functional Analysis," *PLoS One*, vol. 11, no. 2, p. e0148173, Feb. 2016, doi: 10.1371/JOURNAL.PONE.0148173.

[68] T. Komori, "Regulation of bone development and extracellular matrix protein genes by RUNX2," *Cell Tissue Res. 2009 3391*, vol. 339, no. 1, pp. 189–195, Aug. 2009, doi: 10.1007/S00441-009-0832-8.

[69] Y. A *et al.*, "Recombinant human bone morphogenetic protein-2 stimulates osteoblastic maturation and inhibits myogenic differentiation in vitro," *J. Cell Biol.*, vol. 113, no. 3, pp. 681–687, 1991, doi: 10.1083/JCB.113.3.681.

[70] Q. Chen *et al.*, "An Osteopontin-Integrin Interaction Plays a Critical Role in Directing Adipogenesis and Osteogenesis by Mesenchymal Stem Cells," *Stem Cells*, vol. 32, pp. 327–337, 2014, doi: 10.1002/stem.1567.

[71] A. Przekora, "The summary of the most important cell-biomaterial interactions that need to

be considered during in vitro biocompatibility testing of bone scaffolds for tissue engineering applications," *Mater. Sci. Eng. C*, vol. 97, pp. 1036–1051, Apr. 2019, doi: 10.1016/J.MSEC.2019.01.061.

[72] D. E. Rodriguez *et al.*, "Multifunctional role of osteopontin in directing intrafibrillar mineralization of collagen and activation of osteoclasts," *Acta Biomater.*, vol. 10, no. 1, pp. 494–507, Jan. , doi: 10.1016/j.actbio.2013.10.010.

[73] T. Iline-Vul *et al.*, "Osteopontin regulates biomimetic calcium phosphate crystallization from disordered mineral layers covering apatite crystallites," *Sci. Reports 2020 101*, vol. 10, no. 1, pp. 1–16, Sep. 2020, doi: 10.1038/s41598-020-72786-x.

[74] L. F. Bonewald, "The amazing osteocyte," *J. Bone Miner. Res.*, vol. 26, no. 2, pp. 229–238, Feb. 2011, doi: 10.1002/JBMR.320.

[75] G. T. J. Huang, S. Gronthos, and S. Shi, "Critical reviews in oral biology & medicine: Mesenchymal stem cells derived from dental tissues vs. those from other sources: Their biology and role in Regenerative Medicine," *J. Dent. Res.*, vol. 88, no. 9, pp. 792–806, 2009, doi: 10.1177/0022034509340867.

[76] T. Abitbol, E. Kloser, and D. G. Gray, "Estimation of the surface sulfur content of cellulose nanocrystals prepared by sulfuric acid hydrolysis," *Cellulose*, vol. 20, no. 2, pp. 785–794, 2013, doi: 10.1007/s10570-013-9871-0.

[77] S. Beck, M. Méthot, and J. Bouchard, "General procedure for determining cellulose nanocrystal sulfate half-ester content by conductometric titration," *Cellulose*, vol. 22, no. 1, pp. 101–116, 2015, doi: 10.1007/s10570-014-0513-y.

[78] X. M. Dong, J. F. Revol, and D. G. Gray, "Effect of microcrystallite preparation conditions on the formation of colloid crystals of cellulose," *Cellulose*, vol. 5, no. 1, pp. 19–32, 1998, doi: 10.1023/A:1009260511939.

[79] X. Yang, E. Bakaic, T. Hoare, and E. D. Cranston, "Injectable polysaccharide hydrogels reinforced with cellulose nanocrystals: Morphology, rheology, degradation, and cytotoxicity," *Biomacromolecules*, vol. 14, no. 12, pp. 4447–4455, 2013, doi: 10.1021/bm401364z.

[80] D. da Silva Perez, S. Montanari, and M. R. Vignon, "TEMPO-mediated oxidation of cellulose

III," *Biomacromolecules*, vol. 4, no. 5, pp. 1417–1425, Sep. 2003, doi: 10.1021/bm034144s.

[81] E. E. Brown, D. Hu, N. Abu Lail, and X. Zhang, "Potential of nanocrystalline cellulose-fibrin nanocomposites for artificial vascular graft applications," *Biomacromolecules*, vol. 14, no. 4, pp. 1063–1071, Apr. 2013, doi: 10.1021/bm3019467.

2.8. Supporting Information

2.8.1. Materials and methods

Production of CNCs. CNCs were isolated from microcrystalline cellulose (MCC, Sigma-Aldrich, USA), following a well-established sulfuric acid hydrolysis described by Bondeson *et al.* and adapted by Domingues *et al.* Briefly, 42 g of MCC were mixed with 189 mL of DI water with vigorous mechanical agitation for 20 min and at 500 rpm while cooled in an ice bath, and concentrated sulfuric acid (188.3 mL, 95-97% (v/v), Honeywell, USA) was added dropwise up to a final concentration of 64 wt%. The suspension was heated to 44°C in a pre-warmed water bath, under continuous stirring at 500 rpm for 2 h. Afterwards, the reaction was stopped by diluting the suspension with a 5-fold excess of cold deionized (DI) water and left to decant at 4°C for 2 h. Thereafter, the supernatant was discarded, and the remaining suspension was successively centrifuged (Eppendorf 5810R, Germany) for 10 min at 3220 xg and 5°C, until the supernatant became turbid, with continuous replacement of the supernatant with DI water and subsequent resuspension of the solution in each cycle.

The resulting suspension was collected into dialysis membranes (MWCO: 14 kDa, Sigma-Aldrich, USA) and extensively dialyzed against DI water for a week until neutral pH was reached, with regular water replacement. Dialysis membranes were previously treated by washing and submerging them for 2 h in warm DI water several times. After dialysis, the content was sonicated with an ultrasonic processor (VCX750, Sonics & Materials Inc, USA) and using an ultrasound probe (½" Threaded End Part No. 630-0220) for 3 cycles of 5 min at 60% of amplitude output, under ice-cooling, to prevent overheating, which can lead to the desulfation of CNCs. The sonication process helps to disperse the CNCs avoiding the formation of possible aggregates and provides reasonable stability to the suspension. Then, the cloudy suspension was centrifuged one more time (10 min, 5°C, 3220 xg) to remove big particles aggregates and the final supernatant containing the CNCs was collected. The suspension of CNCs was further filtered using a vacuum pump chemically resistant (PTFE) (N820.3FT18, KNF Neuberger), and a fritted funnel D2. The

concentration of CNCs in the final solution (stock solution) was determined gravimetrically to be 2.5 wt.% and was stored at 4°C until further use.

Morphological characterization of CNCs. To characterize the size distribution of the produced CNCs, atomic force microscopy (AFM) was used. For this, a solution of 0.0015% w/v of the CNCs suspension in ultrapure water was prepared and sonicated using an ultrasonic processor (VCX-130PB-220 from Sonics) with an ultrasound probe at 40% amplitude output. Sonication was performed 3 times for 1 min with a 1 min break between cycles. One drop of the diluted solution was placed on a freshly cleaved mica disk that after removing the excess liquid, was left to dry overnight at room temperature, in a desiccator. The CNCs were characterized with AFM Dimension Icon (Bruker, USA), which was used in PeakForce Tapping (ScanAsyst) in air mode with a MultiMode AFM connected to a NanoScope V controller (Veeco, USA). The scans were collected with an AFM cantilever (ScanAsyst-Air, Bruker) made of silicon nitride with a spring constant of 0.4 N/m and frequency of 70 kHz. USA). Several images were collected, and these were then edited and analysed to determine CNCs length and height using the NanoScope Analysis 1.5 software and the Gwyddion software (version: 2.43), respectively. At least 50 nanoparticles were randomly selected from different images for size measurements.

Sulfation degree of CNCs. The amount of protonated sulfate half-ester groups introduced onto the surface of the CNCs during the hydrolysis reaction was determined by conductometric titration with sodium hydroxide (NaOH), following the procedure described elsewhere with minor adjustments [76], [77]. Succinctly, a CNCs suspension containing 150 mg CNCs was diluted with ultrapure water to give a total volume of 200 mL, followed by the addition of 2 mL NaCl solution (0.1 M, Honeywell, USA) for a final concentration of 1 mM NaCl. Thereafter, the solution was titrated with a solution of 10 mM NaOH (Panreac Quimica, Spain), added in 0.25 mL increments over 30-40 min with constant stirring to equilibrate the mixture after each NaOH addition. Titration conductivity values (μS/cm) were recorded using a conductivity meter (DDS-11AW, SCANSCI, UK) and corrected for dilution effects, and plotted against the added volume of NaOH. The typical titration curves show two distinct linear regions: (1) an initial decrease in conductivity with the added NaOH as the protons associated with the sulfate ester groups are consumed and (2) an increase in conductivity with the addition of NaOH which happens once all the charged groups have been neutralized [76]. Furthermore, the inflection point, determined by the intersection of the two linear regions, provides the volume of NaOH (V_{NaOH}) with a defined concentration (C_{NaOH}) required

for the neutralization. Since this is related to the surface charge density of the crystallites, it can be reported as percent sulfur content (%S) by weight, through the following calculation described in equation II.1 [78]:

$$\%\boldsymbol{S} = \frac{\boldsymbol{V_{NaOH} C_{NaOH} M_W(S)}}{\boldsymbol{m_{susp} C_{susp}}} \times \mathbf{100}\% \qquad \textbf{(Equation III.1)}$$

Where m_{susp} and c_{susp} are the mass and concentration (mass %) of the CNCs suspension and M_w (S) is the atomic mass of sulphur. The CNCs conductometric titration was performed in triplicate.

Aldehyde functionalization of CNCs. CNCs were functionalized through sodium periodate ($NaIO_4$) oxidation route, according to the procedures described elsewhere with minor modifications [28]–[30]. In this sense, 3.95 g of sodium (meta) periodate ($NaIO_4$, Sigma Aldrich, Portugal) were added to 200 mL CNCs aqueous suspension (1.5 wt.%) in a 1:1 molar ratio ($NaIO_4$/CNCs). The suspension was stirred for 6 h protected from light exposure and at RT. Non-reacted periodate was quenched by the addition of 8 mL ethylene glycol (Sigma-Aldrich, Portugal). Thereafter, the solution was loaded into dialysis membranes (MWCO: 14kDa, Sigma-Aldrich, USA), previously treated by washing and submerging them for 2 h in warm DI water several times, and then dialyzed against ultrapure water (Milli-Q, 18.2 MΩ.cm) for a week with regular water replacement. The final aldehyde-modified CNCs (a-CNCs) suspension was then collected and stored at 4°C until further use. To concentrate a-CNCs a reverse osmosis procedure was used. Briefly, a suspension of a-CNCs was concentrated against poly(ethylene glycol) (average MW 20,000 kDa, Sigma-Aldrich, USA) using benzoylated cellulose dialysis membranes (2000 Da NMWCO, Sigma-Aldrich, USA). The final a-CNC concentration was determined gravimetrically.

Moreover, the number of aldehyde groups on a-CNCs and the corresponding degree of oxidation were also quantified by acid-base conductometric titration after selectively oxidizing the aldehyde groups to carboxylic acid groups using silver(I) oxide, according to Yang *et al.* with minor modifications [79]. In a typical run, 3.6 mL of a-CNCs aqueous suspension (0.8 wt.%, 0.0288 g) and 0.025 g (0.62 mmol) of NaOH were dispersed in a final volume of 10 mL of ultra-pure water. Afterwards, 0.193 g of silver(I) oxide (Sigma-Aldrich, USA) were added to the solution, which was allowed to stir overnight, whilst selectively oxidizing the aldehyde groups to carboxylic acids. Next, to remove the unreacted silver particles, which may alter the reliability of the conductivity results, the suspension was centrifuged for 10 min at 3220 xg and 15 °C. Then, 5 mL of the supernatant from the centrifuged mixture were diluted with 80 mL of ultrapure water and the pH was adjusted

to 3.5 with 1M HCl (VWR, France) added dropwise. Later, the solution was titrated using a 0.01M NaOH solution, added in 0.25 mL increments for 30-40 min with constant stirring to equilibrate the mixture after each NaOH addition. Lastly, the conductivity values, registered using a conductivity meter (DDS-11AW, SCANSCI, UK) were plotted against the volume of NaOH (in mL) and used to determine the content of carbonyl groups. The total amount of carboxyl groups corresponding to the carbonyl content, or the degree of oxidation (DO) was calculated from equation II.2:

$$\boldsymbol{DO = \frac{162C(V_2 - V_1)}{w - 36C(V_2 - V_1)}} \qquad \textbf{(Equation III.2)}$$

where C is the NaOH concentration (mol/L), V_1 and V_2 are the amount of NaOH shown in conductimetric titration curves, and w (g) is the weight of a-CNCs [80]. The conductometric titrations were performed in triplicate.

Scanning electron microscopy of CNCs. High-Resolution scanning electron microscopy (HR-SEM) analysis was performed to confirm if the decoration of CNCs with Hap was successful and to study Hap morphology, using a high-resolution field emission scanning electron microscope (Auriga Compact, Zeiss, Germany), which compared to conventional SEM produces clearer and less electrostatically distorted images. For this, CNCs and CNCs/Hap dilutions (0.01 and 0.001% v/v) were prepared from the stock solutions and sonicated (5 min, 60%; VCX750, Sonics & Materials Inc, USA) to disperse the nanoparticles. Then, a drop of each solution was placed on top of aluminium stubs fitted with conductive adhesive carbon tape (Media Lab System S.r.l., Italy) and circular coverglasses (13 mm Ø; 0.16-0.19 mm thickness; optical quality borosilicate; Agar Scientific Ltd, UK) cut at half, and allowed to dry until the procedure was performed. After drying, the samples were then transferred into the SEM chamber and imaged at RT with an incident electron beam accelerated to 3 kV.

Water uptake and degradation profile of cryogel scaffolds. For determining the water uptake behaviour of the developed cryogels, the samples were initially weighed (Wi) and subsequently immersed, for 30 s, in 1 mL phosphate buffered saline (PBS, Sigma-Aldrich, USA). The samples were immediately weighed (Wf) and the water uptake (mg/mg sample) was calculated using Equation II.3. All experiments were performed in triplicate.

$$\boldsymbol{Water\ Uptake = \frac{W_f - W_i}{W_i}} \qquad \textbf{(Equation III.3)}$$

Regarding the degradation properties, the weight loss of the cryogels over time was also analysed. For that, the specimens were incubated in 1 mL of PBS at 37 °C for 2 h. After removing the excess PBS, the initial mass of the cryogel was measured (Mi) and successively weighed at different pre-selected time points (Mf) to determine the weight loss (%), according to equation II.4. The results are expressed as an average of three samples.

$$\text{Weight loss (\%)} = \frac{W_i - W_f}{W_i} \times 100\% \qquad \textbf{(Equation III.4)}$$

2.8.2. Results and discussion

Aldehyde functionalization of CNCs (a-CNCs). After the oxidation protocol of CNCs, the carbonyl content and corresponding degree of oxidation was quantified by conductometric titration after selectively oxidizing the aldehydes to carboxylic acid using silver(I) oxide [79]. It was estimated that 0.18 ± 0.04 mmol of carbonyl groups per gram of CNCs have been oxidatively introduced. This result is comparable to the results obtained by Dash *et al.* [30], but lower than the ones reported by Yang *et al.* [79] for periodate oxidised a-CNCs. The degree of chemical modification achieved guarantees sufficient reactivity while preserving the integrity of crystalline structure of CNCs and thus its potential as reinforcement agent, since higher degrees of oxidation showed to affect its original crystalline properties [81]. The effective aldehyde functionalization of CNC was also confirmed by FTIR, demonstrated by the characteristic C=O stretching vibration band at 1647 cm^{-1} from the aldehyde groups visible on modified a-CNCs and not on unmodified CNCs reference (Figure S.1)

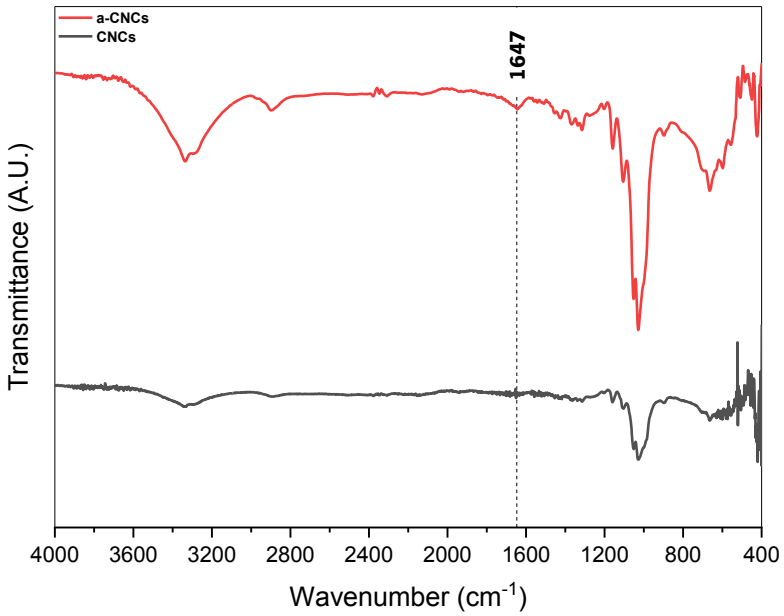

Figure S.1: FTIR spectra of CNCs and aCNCs. The characteristic peak of aldehyde group (C=O) is highlighted.

Morphological characterization of mineralized CNCs. SEM images showed that for higher Ca^{2+}/SO_3^- ratios (i.e., 40) more Hap is being formed, as expected, although more detached nanoparticles could be seen (figure S.2). Moreover, we also confirm the tendency for Hap to aggregate at basic pH values as 7.9 (figure S.2 b), as postulate before [45].

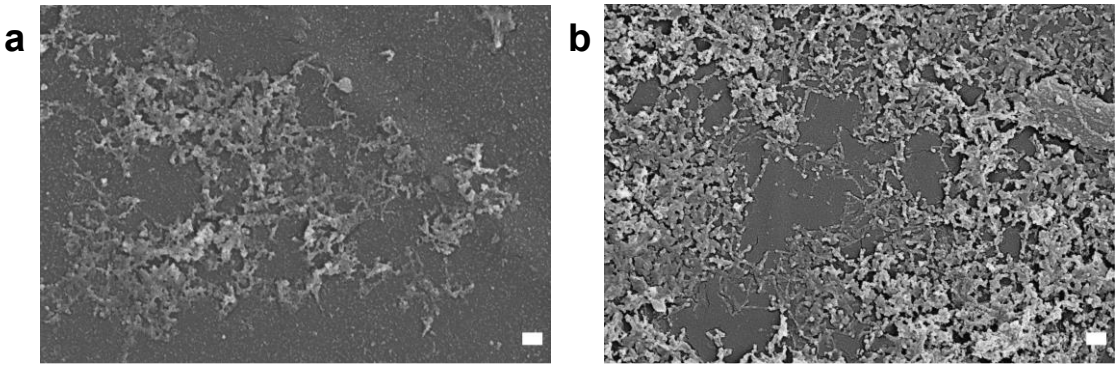

Figure S.2: Morphological characterization of Ca^{2+}/SO_3^- =40 ratio m-CNCs. SEM images of **(a)** m-CNCs pH 6.9 and **(b)** m-CNCs pH 7.9 produced with a ratio Ca^{2+}/SO_3^- =40. Scale bar: 300 nm.

FTIR analysis of CNCs and m-CNCs. The FTIR spectrum of m-CNCs (figure S.3) exhibited an adsorption at 1637 cm^{-1}, corresponding to the O–H bending of the water adsorbed by cellulose [31], [45]. Furthermore, other typical peaks of CNCs can be observed in the developed m-CNCs at 1428 cm^{-1} (CH_2 scissoring motion), 1369 cm^{-1} (C–H bending), 1316 cm^{-1} (CH_2 wagging vibration), 1159 cm^{-1} (C–C ring stretching) and 1054 cm^{-1} (C–O–C stretching vibration) [31], [45]. Moreover, the band seen at 895 cm^{-1} was assigned to the cellulosic b-glycosidic linkages [31], [45].

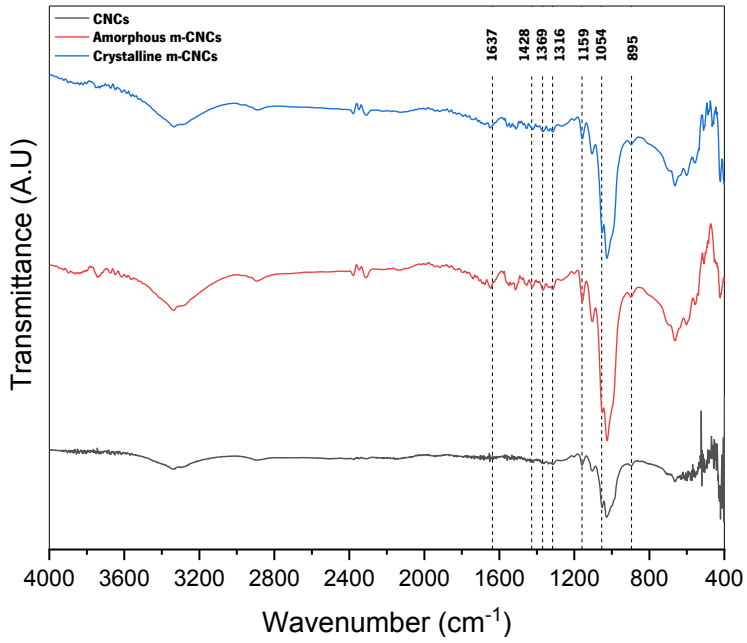

Figure S.3: FTIR spectra of CNCs and m-CNCs. The characteristic peaks of CNCs are highlighted.

Chapter IV.

General Conclusions

CHAPTER IV. General Conclusions

In the last years, bone tissue engineering strategies have drawn significant attention in the biomedical field due to the possibility of developing approaches that could regenerate a crucial element of the human body without restricting patients functionally. Numerous strategies have been proposed through the combination of inorganic (ceramics, metals, or metallic alloys) and/or organic (synthetic or natural origin polymers) biomaterials-based scaffolds, progenitor cells, and biophysical/biochemical stimuli. They have deeply contributed for the increasing level of success of bone regenerative strategies. Nevertheless, these approaches have failed to mimic the true and full complexity of bone, namely the nanoscale biomineralization as well as the role of non-collagenous proteins in its regulation.

Therefore, in this work, we developed a bioinspired scaffold that emulates the nanoscale biomineralization microenvironment in vitro. For this, we combined a cryogel scaffold based on PL with a-CNCs acting as crosslinkers and m-CNCs as biorreactive nanofillers. We could successfully obtain CNCs with Hap showing more-amorphous and more-crystalline structures by tuning the mineralization conditions. We found that cryogel scaffolds incorporating these m-CNCs enhanced the metabolic activity, cell proliferation, and ALP activity of different cell populations. Moreover, they also up-regulated the expression of bone-related markers, as RUNX2, BMP-2, ALP, OPN, and COL1A1 of hASCs. In addition, immunohistochemical analysis revealed that hASCs seeded on the cryogels containing the amorphous-like Hap presented the typical osteoblast phenotype. Overall, the results from this thesis suggest that the incorporation of m-CNCs improved the biological performance of the developed cryogels by ameliorating their osteoinductive properties, triggering desirable primary processes related with osteogenic differentiation and bone regeneration. In summary, the proposed mineralized cryogel scaffolds could be potentially useful for bone tissue engineering and regenerative medicine strategies due to their ability to mimic the nanoscale mineralization process and microenvironment and to promote osteogenic differentiation.

In future works, it would be interesting to study the angiogenic and neurogenic potential of the developed system in order to recapitulate the vascularization and innervation of native bone tissue. Moreover, the culture of the scaffolds within bioreactors to mimic the human body biophysical, biochemical, and/or hydrodynamic conditions could be also applied. Generally, these systems allow a mechanical stimulation and a more efficient supply of nutrients and waste removal, which yield more homogeneous colonization with cells, enhancing the crosstalk between each other

and the scaffold, and matrix deposition within large engineered scaffolds. Ultimately, a in vivo study should be considered to evaluate the full potential of our strategy in regenerating bone, and to continue the research towards the clinical translation of the proposed system.